Detached Eddy Simulation of Turbulent Flow and Heat Transfer in Turbine Blade Internal Cooling Ducts

Aroon K Viswanathan

Dissertation submitted to the faculty of Virginia Polytechnic Institute and State University in partial fulfillment of the requirements for the degree of

Doctor of Philosophy
in
Mechanical Engineering

Dr. Danesh K. Tafti, Chair
Dr. William J. Devenport
Dr. Thomas E. Diller
Dr. Muhammad R. Hajj
Dr. Wing F. Ng

July 31, 2006
Blacksburg, Virginia

Keywords: *Detached Eddy Simulations (DES), Coriolis forces, centrifugal buoyancy, ribbed ducts, turbine blade internal cooling*

Detached Eddy Simulation of Turbulent Flow and Heat Transfer in Turbine Blade Internal Cooling Ducts

Aroon K Viswanathan

Abstract

Detached Eddy Simulations (DES) is a hybrid URANS-LES technique that was proposed to obtain computationally feasible solutions of high Reynolds number flows undergoing massive separation with reliable accuracy. Since its inception, DES has been applied to a wide variety of flow fields, but mostly limited to unbounded external aerodynamic flows. This is the first study to apply and validate DES to predict the internal flow and heat transfer in non-canonical flows of industrial relevance. The prediction capabilities of DES in capturing the effects of Coriolis forces, which are induced by rotation, and centrifugal buoyancy forces, which are induced by thermal gradients, are also authenticated.

The accurate prediction of turbulent flows is sensitive to the level of turbulence predicted by the turbulence scheme. By treating the regions of interest in LES mode, DES allows the unsteadiness in these regions to develop and hence predicts the turbulence levels accurately. Additionally, this permits DES to capture the effects of system rotation and buoyancy. Computations on a rotating system (a sudden expansion duct) and a system subjected to thermal gradients (cavity with a heated wall) validate the prediction capability of DES.

The application of DES is further extended to a non-canonical, internal flow which is of relevance in internal cooling of gas turbine blades. Computations of the fully developed flow and heat transfer shows that DES surpasses several shortcomings of the RANS model on which it is based. DES accurately predicts the primary and secondary flow features, the turbulence characteristics and the heat transfer in stationary ducts and in rotating ducts, where the effects of Coriolis forces and centrifugal buoyancy forces are dominant. DES computations are carried out at a computational cost that is almost an order of magnitude less than the LES with little compromise on the accuracy.

However, the capabilities of DES in predicting the transition to turbulence are inadequate, as highlighted by the flow features and the heat transfer in the developing region of the duct. But once the flow becomes fully turbulent, DES predicts the flow physics and shows good quantitative agreement with the experiments and LES.

Granting Institution

This research was supported by the US DOE, Office of Fossil Energy, and National Energy Technology Laboratory. Any opinions, findings, conclusions, or recommendations expressed herein are those of the authors and do not necessarily reflect the views of the DOE.

To my parents, mentors and friends

Acknowledgements

Working on this dissertation over the last three years has been pretty rewarding in terms of the knowledge and insight I have gained in the field of turbulence modeling. In the course of this I have got advice, help and encouragement from many people whom I would like to thank. I am extremely grateful for the guidance of my advisor, Dr. Danesh Tafti. His mentoring, encouragement and optimism have consistently helped me get over the several obstacles that I have run into during this period. He has always been present in his office and the lab, even during off-hours like semester breaks, weekends and late evenings, to answer my queries. His code GenIDLEST has been used for running all the calculations presented in this dissertation.

I would also like to thank my committee members Dr. Devenport, Dr. Diller, Dr. Hajj and Dr. Ng for reviewing my work and providing valuable suggestions during my preliminary defense.

I have been privileged to work with my colleagues at the HPCFD lab. I would like to thank Evan Sewall, Samer Abdel-Wahab, Wilfred Patrick and Sundar Narayan from whom I learnt a lot during the first year of my PhD. Special thanks to Emily Sewall for the snacks and cookies which she used to send with Evan. I would also like to thank the other members of the HPCFD lab: Ali Rozati, Shi Ming Li, Ju Kim, Anant Shah, Mohammad Elyyan, Pradeep Gopalakrishnan and Keegan Delaney with whom learnt and shared a good deal of knowledge. Ali, Mohammad, I'll keep checking the ESPN web-page for updates on the NBA 2007 draft. Hope to see you guys in the first round of the draft.

I have enjoyed the company of my dearest friends Giridhar, Kavita, Ashvin, Vikram, Wilfred and Leepika. Thank you for being with me during thick and thin. Thank you Giridhar for your company during our regular weekend hikes. I wouldn't have explored Blacksburg as much without you. Thank you Kavita for your constant (and loud) lectures on how CLA and PPAR-α affect the fat content in my body. I know for sure that these have had a severe effect on my hearing. I have also had the privileged company of several others – Nitin, Owais, Umesh, Pratik, Ritesh and Akhilesh who have hung out with me during the past three years.

I would also like to thank Dr. Don Waldron and Dr. (Mrs.) Claire Waldron, who were my hosts in Blacksburg. They were my family away from home and took care of me during the three years.

Finally, I owe the most to my parents who have encouraged me all through me graduate studies. To them, to my mentors and to my friends, I dedicate this work.

Project Description

This study is a subset of the project "Enhanced Prediction Techniques Based on Time-Accurate Simulations for Turbine Blade Internal Cooling" which aims at applying, developing and demonstrating the use of high-fidelity Large Eddy Simulations (LES) and a hybrid RANS-LES technique – Detached Eddy Simulations (DES) as accurate prediction tools for the analysis of the three-dimensional, unsteady flow and heat transfer in rotating internal cooling ducts. These computational approaches are integrated with experiments from the literature and three-component mean and turbulent flow field measurements made in a large scale ribbed channel using Laser Doppler Velocimetry (LDV).

The project studies the application of the computational techniques in internal cooling geometries with ribs. Of prime interest are: (a) the developing flow regime (b) the fully developed region, and (c) the 180º bend region that connects two passes of the cooling duct. LES has been applied in the fully developed region for stationary internal cooling ducts by D. K. Tafti and in rotating ducts by Samer Abdel-Wahab. More recent work on the application of LES to the developing region and the 180º bend of the duct for stationary ducts as well as rotating ducts, where the flow is affected by Coriolis forces and centrifugal buoyancy was carried out by Evan Sewall.

The application of DES in these studies is aimed at cutting down the cost of the computation as compared to LES while not compromising on the accuracy. The performance of DES is initially evaluated in the fully developed region of the ribbed duct. The performance of DES in predicting the flow and heat transfer in stationary and rotating ducts is validated from experiments in literature and earlier LES calculations.

Since DES is computationally less intensive than LES, it is feasible to study a complete two-pass duct which combines all the cases individually studied by LES – the developing region of the flow, the fully developed region and the 180º bend. These studies are validated with experiments from literature, experiments as a part of this project (assisted by K. A. Thole) and the LES computations.

As of date, 15 conference papers and 8 journal papers have been published from this project. From the DES computations, which were carried out with the assistance of D. K. Tafti, 2 conference papers and 4 journal papers have been published. A list of all the publications is shown in Table 1. The relevant publications have been highlighted in the Table and the abstracts of these publications are reproduced in Appendix C.

Table 1: List of publications from the project "Enhanced Prediction Techniques Based on Time-Accurate Simulations for Turbine Blade Internal Cooling"

Paper	Publication Year
Tafti D. K., Large Eddy Simulations of Heat Transfer in A Ribbed Channel for Internal Cooling of Turbine Blades, Paper No. GT2003-38122, Proceedings of ASME/IGTI Turbo Expo., Atlanta, Georgia, June 16-19, 2003.	2003
Tafti, D. K., Evaluating the Role of Subgrid Stress Modeling in a Ribbed Duct for the Internal Cooling of Turbine Blades*, Int. J. Heat Fluid Flow*, 26, pp 92-104, 2005	2005
Abdel-Wahab, S. and Tafti, D. K., Large Eddy Simulation of Flow and Heat Transfer in a Staggered 45^{o} Ribbed Duct, GT2004-53800, ASME Turbo Expo: 2004, Vienna, Austria.	2004
Abdel-Wahab, S. and Tafti, D. K., Large Eddy Simulations of Flow and Heat Transfer in a 90^{o} Ribbed Duct with Rotation - Effect of Coriolis Forces, GT2004-53796, ASME Turbo Expo: 2004, Vienna, Austria.	2004
Abdel-Wahab, S. and Tafti, D. K., Large Eddy Simulations of Flow and Heat Transfer in a 90^{o} Ribbed Duct with Rotation - Effect of Buoyancy Forces, GT2004-53799, ASME Turbo Expo: 2004, Vienna, Austria.	2004
Abdel-Wahab, S. and Tafti, D. K., Large Eddy Simulations of Flow and Heat Transfer in a 90º Ribbed Duct with Rotation - Effect of Coriolis and Centrifugal Buoyancy Forces, *J. Turbomachinery,* 126, pp 627-636, 2005.	2005

Sewall, E, and Tafti, D. K., Large Eddy Simulation of the Developing Region of a Stationary Ribbed Internal Turbine Blade Cooling Channel, GT2004-53832, ASME Turbo Expo: 2004, Vienna, Austria	2004
Sewall, E, and Tafti, D. K., Large Eddy Simulation of the Developing Region of a Rotating Ribbed Internal Turbine Blade Cooling Channel, GT2004-53833, ASME Turbo Expo: 2004, Vienna, Austria.	2004
Graham, A., Sewall, E., Thole, K.A., Flowfield Measurements in a Ribbed Channel Relevant to Internal Turbine Blade Cooling, GT2004-53361, ASME Turbo Expo: 2004, Vienna, Austria.	2004
Sewall, E, and Tafti, D. K., Large Eddy Simulation of Flow and Heat Transfer in the Developing Flow Region of a Rotating Gas Turbine Blade Internal Cooling Duct with Coriolis and Buoyancy Forces, GT2005-68519, ASME Turbo Expo, Reno-Tahoe, USA	2005
Sewall, E, and Tafti, D. K., Large Eddy Simulation of Flow and Heat Transfer in the 180 Degree Bend Region of a Stationary Ribbed Gas Turbine Blade Internal Cooling Duct, GT2005-68518, ASME Turbo Expo, Reno-Tahoe, USA	2005
Sewall, E, and Tafti, D. K., Large Eddy Simulation of Flow and Heat Transfer in the 180 Degree Bend Region of a Stationary Ribbed Gas Turbine Blade Internal Cooling Duct, *In press ASME J. Turbomachinery.*	2005
Sewall, E.A., Tafti, D.K., Graham, A.B., Thole, K.A., Experimental Validation of Large Eddy Simulations of Flow and Heat Transfer in a Stationary Ribbed Duct, *, Int. J. Heat Fluid Flow*, 27, pp 243-258, 2006	2006
Viswanathan, A.K., Tafti, D.K., "Detached Eddy Simulation of Turbulent Flow and Heat Transfer in a Ribbed Duct", HT-FED04-56152, Proceedings of Heat Transfer/ Fluids Engineering Summer Conference ASME, July 11-15, Charlotte, USA.	2004
Viswanathan, A.K., Tafti, D.K., Abdel-Wahab., S., "Large Eddy Simulation of Flow and Heat Transfer in an Internal Cooling Duct with High Blockage Ratio 45° Staggered Ribs", GT2005-68086, ASME Turbo Expo 2005, June 6-9, Reno-Tahoe, USA.	2005
Viswanathan, A.K., Tafti, D.K., "Large Eddy Simulation in a Duct with Rounded Skewed Ribs", GT2005-68117, ASME Turbo Expo 2005, June 6-9, Reno-Tahoe, USA.	2005

Viswanathan, A.K., Tafti, D.K., "Detached Eddy Simulation of Flow and Heat Transfer in a Stationary Internal Cooling Duct with Skewed Ribs", GT2005-68118, ASME Turbo Expo 2005, June 6-9, Reno-Tahoe, USA.	2005
Viswanathan, A.K., Tafti, D.K., "Detached Eddy Simulation of Turbulent Flow and Heat Transfer in a Ribbed Duct", ASME Journal of Fluids Engineering, 127(5), pp 888-896, September 2005	2005[+]
Viswanathan, A.K., Tafti, D.K., "A Comparative Study of DES and URANS in a Two-pass Internal Cooling Duct with Normal Ribs", IMECE2005-79288, ASME International Mechanical Engineering Congress and Exposition 2005, November 5-11, Orlando, Florida, USA.	2005[+]
Viswanathan, A.K., Tafti, D.K., "Detached Eddy Simulation of Turbulent Flow and Heat Transfer in a Two-pass Internal Cooling Duct", *Int J of Heat and Fluid Flow*, 27, pp 1 – 20, 2006.	2006*
Viswanathan, A.K., Tafti, D.K., "Large Eddy Simulation of the fully developed Flow and Heat Transfer in a Rotating Duct with 45° Ribs", GT2006-90229, ASME Turbo Expo 2006, May 8-11, Barcelona, Spain.	2006
Viswanathan A.K., Tafti, D. K., 2005, Detached Eddy Simulation of Flow and Heat Transfer in Fully Developed Rotating Internal Cooling Channel with Normal Ribs , *Int. J Heat and Fluid Flow.* 27, pp 351-370, 2006	2006*
Viswanathan, A.K., Tafti, D.K., "A Comparative Study of DES and URANS for Flow Prediction in a Two-pass Internal Cooling Duct", *In press ASME Journal of Fluids Engineering*	2006

[+] Figures and tables are reprinted with permission from ASME

[*] Figures are reprinted with permission from Elsevier

Table of contents

Abstract ii

Project Description vi

List of Tables xii

List of Figures xiii

Nomenclature xx

1 Introduction 1
1.1 Problem Description 5

2 Literature Review 9
2.1 Stationary Internal Flows 10
2.2 Modeling the Effect of Coriolis Forces 12
2.3 Modeling the Effect of Buoyancy Forces 15

3 Computational Model and Governing Equations 22
3.1 Mean Flow and Energy Equations 22
3.2 Turbulence Models 23
3.2.1 *k-ω* Equations (1988 Wilcox Model) 23
3.2.2 Menter's Baseline Model 24
3.2.3 Shear-Stress Transport (SST) Model 26
3.3 Detached Eddy Simulations 26
3.4 Numerical Method 28
3.5 Post-processing 29

4 Validation Cases – Effects of Rotation and Buoyancy 31
4.1 Capturing the Effects of Rotation in Sudden Expansion Channels using Detached Eddy Simulations 31
4.1.1 Computational Details 33
4.1.2 Grid Sensitivity 34
4.1.3 Comparison of Turbulence Strategies 35
4.1.4 DES Regions 38
4.1.5 Flow Characteristics 40
4.1.6 Conclusions 44
4.2 Prediction of the Turbulent Cavity Flow driven by Shear and Buoyancy using Detached Eddy Simulations 45
4.2.1 Computational Details 46
4.2.2 Effect of Grid Density 48
4.2.3 Effect of additional buoyancy terms 49
4.2.4 Effects of buoyancy 50
4.2.5 Conclusions 52

5 Flow and Heat Transfer in the Fully Developed Ribbed Duct 53
5.1 Grid Sensitivity Comparisons 55
5.2 DES Regions 57
5.3 Stationary Duct 59
5.3.1 Flow Field Predictions 59
5.3.2 Heat Transfer Enhancement 64
5.3.3 Summary and Conclusions 68
5.4 Rotating Duct - Effects of Coriolis Forces 69
5.4.1 Mean Flow field 70
5.4.2 Turbulent Flow Characteristics 75
5.4.3 Mean Heat Transfer 77
5.4.4 Conclusions 83
5.5 Rotating Ducts - Effects of Coriolis Forces and Centrifugal Buoyancy 85
5.5.1 Effects of Centrifugal Buoyancy 86
5.5.2 Mean Flow Features 87
5.5.3 Turbulent Flow Features 91
5.5.4 Heat Transfer Augmentation 93
5.5.5 Summary and Conclusions 100

6 Flow and Heat Transfer in a complete Two Pass Duct connected by a 180º Bend 103
6.1 Stationary Two-Pass Duct 105
6.1.1 Mean Flow Field 106
6.1.2 Summary and Conclusions 126
6.2 Rotating Two Pass Duct – Effect of Coriolis Forces 128
6.2.1 Developing Flow 129
6.2.2 Heat Transfer Augmentation in the First Pass 132
6.2.3 Flow in the 180º Bend 135
6.2.4 Heat Transfer in the 180º Bend 137
6.2.5 Pitch Averaged Friction Factor 139
6.2.6 Rib Averaged Heat Transfer Augmentation 142
6.2.7 Summary and Conclusions 143

7 Summary and Conclusions 145
7.1 Recommendations 145

References 148

Appendix A: Additional Buoyancy Production Term in the *k*-equation 156

Appendix B: Dimensionless Parameters 158

Appendix C: Abstracts of relevant publications 160

List of Tables

Table 1: List of publications from the project "Enhanced Prediction Techniques Based on Time-Accurate Simulations for Turbine Blade Internal Cooling"..... vii

Table 2: Variation in the coefficient of the buoyancy production term in the ω or ε equation used by different groups.....19

Table 3: Extra terms in the momentum (S_u) and energy equations (S_θ) for the different cases studied.....23

Table 4: *a-posteriori* comparison of the grid dimensions in the three directions for the DES grids.....55

Table 5 : Percentage form and friction drag in the ribbed duct.....59

Table 6 : Comparison of the overall friction factor.....63

Table 7 : Comparison of the overall heat transfer augmentation.....67

Table 8: Variation of the heat transfer augmentation at the ribbed and side walls for different rotation and buoyancy cases.....100

Table 9: Comparison of the surface pressure drop as predicted by the current computation in comparison with the experimental measurements by Prabhu and Vedula (2003) for the rotating duct.....141

List of Figures

Figure 1: (a) The cross-section of the first stage rotating blade used in the Siemens - Westinghouse 501-F Engine (Courtesy: Howard, G., O'Brein, W.F.,) (b) Schematic diagram of the turbine balde cross-section (Han, J.C., 1988) showing the region of interest 6

Figure 2: Geometry used for computation of flow downstream of a back-facing step. The effect of clockwise (negative) rotation and anti-clockwise (positive) rotation are also shown. Red arrows show the effect of Coriolis forces on the reattachment. 32

Figure 3: Grid distribution in the *x, y, z* directions downstream of the back-facing step, for the aspect ratio 2 channel. 34

Figure 4: Comparison of the reattachment lengths for the three grids used for DES Computation 35

Figure 5: Comparison of the reattachment lengths downstream of the back-facing step for a stationary case (Ro = 0.00, Aspect ratio = 2). LES = 5.25, DES = 7.20, URANS = 10.00 36

Figure 6: Comparison of the reattachment lengths as predicted by DES *k-ω* (Duct AR = 2), URANS *k-ω* (AR = 2) and earlier studies by Nilsen and Andersson (1990) (Re = 5500, AR = 2) and Iaccarino *et al.,* (1999) with experimental measurements by Rothe and Johnston (1979). 37

Figure 7: Instantaneous coherent vorticity contours downstream of the back-facing step (AR = 2), at the center of the duct for DES (Top) and URANS (Bottom). 38

Figure 8: DES regions downstream of the back-facing step showing the dominance of LES characteristics in the region of separation (Case shown is Ro = 0.04).....39

Figure 9: Iso-surfaces of coherent vorticity to show the stabilizing (Ro = -0.08) and the destabilizing effects (Ro = 0.08) of rotation on the flow downstream of the backfacing step. (Aspect Ratio = 5) 40

Figure 10: Variation of the reattachment lengths at the center of the channel with rotation number for the duct of aspect ratio 5 (Top) and 2 (Bottom).....41

Figure 11: Comparison of the reattachment lengths for a duct of (a) AR = 5 (b) AR = 2.....43

Figure 12: Top view of the instantaneous coherent vortices downstream of a backward facing step for ducts of aspect ratio 2 (Top) and aspect ratio 5 (bottom) 44

Figure 13: Schematic diagram of the 2D cavity studied. Periodic boundary conditions are used in the *z* direction.....46

Figure 14: Schematic diagram showing the measurement planes where the temperature profiles have been reported.....47

Figure 15: Grid independency study comparing the spatial variation of temperature predicted by DES and LES with experimental data. Data has been extracted at the vertical center (y/L = 0.5) and horizontal center (x/L = 0.5) of the cavity.....48

Figure 16: Effect of the buoyancy term in the URANS (Top) and DES (Bottom) calculation. Data has been extracted at the vertical center (y/L = 0.5) and horizontal center (x/L = 0.5) of the cavity 50

Figure 17: Effect of buoyancy in influencing the temperature in the cavity at y/L = 0.5 and at x/L = 0.5 51

Figure 18: Comparison of the spatial variation of temperature (LES on 64 x 64 x 64 grid, DES and URANS on 32 x 32 x 32 grid) with experiments by Grand (1975), for a high buoyancy case.....51

Figure 19 : The computational model - A pair of ribs placed at the center of the duct. Flow in the duct is periodic in the streamwise direction.....54

Figure 20 : Comparison of the streamwise velocities in a plane through the ribs (y/e = 0.25) for the (a) 48^3 grid (b) 64^3 grid (c) 96^3 grid (d) LES 128^3 case. 64^3 and the 96^3 case show the best agreement. 48^3 grid overpredits the extent of the recirculation region.....56

Figure 21 : Plot of the LES and RANS region in the DES computation for the 64^3 grid in a *Z* plane. A value of 1 represents a complete LES region and a value of 0 a complete RANS region. Flow is periodic in the streamwise direction.....58

Figure 22 : Streamwise velocity distributions at the center of the duct at y/e = 0.1 in comparison with the experimental measurements by Rau *et al.*, (1998).....60

Figure 23 : Comparison of streamwise velocity distributions at y/e = 0.25 for the (a) k-ω DES case (b) SST DES case (c) k-ω RANS case (d) LES case.....61

Figure 24 : Comparison of the secondary flow distribution at y/e = 1.5 and z/D_h = 0.45.....62

Figure 25 : Comparison of the secondary flow (a) predicted by DES *k-ω* model (b) DES SST model (c) *k-ω* RANS model (d) Experimental (Liou *et al.*). 63

Figure 26 : Streamlines showing the recirculation region in front of the rib and primary and secondary circulations behind the rib and their effect on heat transfer on the walls. Red regions represent high heat transfer, while blue regions represent low heat transfer. 64

Figure 27 : Comparison of augmentation ratios on the ribbed floor for the (a) *k-ω* DES case (b) Menter's SST DES case (c) *k-ω* RANS case (d) LES case 65

Figure 28 : Comparison of the augmentation ratios (a) at the center of the ribbed floor (b) side walls upstream of the rib 66

Figure 29 : Comparison of the heat transfer augmentation ratios on the side walls (a) *k-ω* DES (b) Menter's SST DES (c) *k-ω* RANS (d) LES 67

Figure 30: Effect of Coriolis forces in a square duct subjected to rotation.....69

Figure 31: Streamlines showing the flow in a fully developed duct as predicted by DES SST at Z = 0.5 (a) Ro = 0.18 (b) Ro = 0.35 (c) Ro = 0.67. Y = 0 represents the trailing wall, while Y = 1 represents the leading wall. Flow direction is from left to right. 71

Figure 32: Streamlines showing the flow in a fully developed duct rotating at Ro = 0.35 at Z = 0.5 as predicted by (a) LES (b) DES SST (c) URANS SST. Y = 0 represents the trailing wall, while Y = 1 represents the leading wall. Flow direction is from left to right. 73

Figure 33: Secondary flow contours on the rib for (a) Ro = 0.0 (b) Ro = 0.18 (c) Ro = 0.35 (d) Ro = 0.67 as predicted by DES SST. The contours show the effect of rotation on the secondary flow in the cross-section. 74

Figure 34: TKE values as predicted by the DES, LES and the URANS cases for the three rotation cases in between the ribs at z = 0.5.....75

Figure 35: Coherent vorticity contours for the (a) LES 128^3 (b) DES 64^3 (c) URANS 64^3 for Ro = 0.35 show the scales resolved of the three schemes. 76

Figure 36: Heat transfer augmentation (Nu/Nu_0) predicted at the leading and the trailing walls by DES SST for (a) Ro = 0.18 (b) Ro = 0.35 (c) Ro = 0.67. Flow direction is from left to right. 77

Figure 37: Heat transfer augmentation (Nu/Nu_0) predicted at the leading (upper half of the plot) and the trailing walls (lower half of the plot) for the Ro = 0.35 case by (a) LES (b) DES SST(c) URANS SST. Flow direction is from left to right.....78

Figure 38: Heat transfer augmentation (Nu/Nu_0) predicted at the side wall by DES SST for the (a) Ro = 0.18 (b) Ro = 0.35 (c) Ro = 0.67. Flow direction is from left to right. 80

Figure 39: Heat transfer augmentation (Nu/Nu_0) predicted at the side wall for the Ro = 0.35 case by (a) LES (b) DES SST(c) URANS SST. Flow direction is from left to right. 81

Figure 40: Side wall heat transfer predicted by LES, DES and URANS for the various rotation cases. 81

Figure 41: Comparison of average Nusselt number augmentation ratios at the leading and trailing sides with experiments. 82

Figure 42: Effect of Coriolis forces (F) and Centrifugal Buoyancy (F_b) in rotating ducts 86

Figure 43: Comparison of the recirculation regions at the leading edge for the three rotation cases with Bo = 0.12. 88

Figure 44: Comparison of the recirculation regions at the leading edge for the three different buoyancy cases with Ro = 0.35. 89

Figure 45: Comparison of the secondary velocities for Ro = 0.35 for varying buoyancies (a) Bo = 0.00 (b) Bo = 0.12 (c) Bo = 0.29.....90

Figure 46: Comparison of the secondary flows as predicted by DES and LES at the center of the rib region for Bo = 0.29 and Ro = 0.35, for (a) DES (b) LES. ...91

Figure 47: Comparison of the turbulent kinetic energy in between two consecutive ribs at $z = 0.5$. 92

Figure 48: Heat transfer distribution at the center of the duct (z/D_h =0.5) at the leading and trailing surfaces. Buoyancy in all the cases is Bo = 0.12 93

Figure 49: Heat transfer distribution at the ribbed walls for varying buoyancy numbers for a constant Ro = 0.35. 94

Figure 50: Effect of the variation of rotation and buoyancy on the heat transfer at the side walls, plotted at a distance of 0.5*e* upstream of the ribs. 96

Figure 51: Comparison of the ribbed (Top) and side wall (Bottom) heat transfer predicted by DES and LES for Ro = 0.35 and Bo = 0.29 97

Figure 52: Comparison of the surface averaged ribbed wall heat transfer augmentation 99

Figure 53: Comparison of the side wall heat transfer augmentations..... 99

Figure 54: The two-pass internal cooling duct geometry studied 104

Figure 55: Comparison of streamlines in the developing region through a plane passing through the center z-plane..... 106

Figure 56: Comparison of u-velocities in the developing region through the center z-plane 107

Figure 57: U-velocities at a plane passing through the rib (a) Experiments Rau *et al.,* (1998), P/e = 9 (b) LES – Fully Developed Region (Rib 6) (c) DES – Fully Developed Region (Rib 6) (d) URANS – Fully Developed Region (Rib 6) 108

Figure 58: Comparison of the streamwise velocities at *y/e* = 0.1 with experimental data. 109

Figure 59: Comparison of w-velocities in the developing region through a plane near the side wall 110

Figure 60: Secondary flow in the duct measured at *y/e* = 1.5 and z/D_h = 0.45. 111

Figure 61: Heat transfer augmentation in the first pass of the two-pass duct at the side wall (Top) and Ribbed Wall (Bottom) 113

Figure 62: Side wall heat transfer (a) Experiments Rau *et al.,* (1998) *P/e* = 9 (b) LES – Fully Developed Region (Rib 6) (c) DES –Fully Developed Case (Rib 6) (d) URANS – Fully Developed Region (Rib 6). (b), (c) and (d) show the heat transfer from the lower rib to the center of the duct side wall..... 114

Figure 63: Comparison of side wall heat transfer with the experimental observations. 115

Figure 64: Ribbed wall heat transfer (a) Experiments Rau *et al.,* (1998) P/e = 12 (b) LES – Fully Developed Region (Rib 6) (c) DES –Fully Developed Case (Rib 6) (d) URANS – Fully Developed Region (Rib 6). Only half of the ribbed wall is shown in (b), (c) and (d)..... 116

Figure 65: Comparison of ribbed wall heat transfer with the experimental measurements. 117

Figure 66: Comparison of the flow predicted by DES and URANS in the 180 degree bend. 118

Figure 67: Secondary flow at the center of the 180 degree bend. 118

Figure 68: Velocities in the center of the 180° bend in comparison with experiments by Sewall *et al*., (2006a). 120

Figure 69: Heat Transfer augmentation at the ribbed wall and outer walls in the vicinity of the 180 degree bend. Flow direction indicated by arrows. 121

Figure 70: block averaged friction factors in the complete channel..... 123

Figure 71: Block averaged heat transfer at (a) inner wall (b) outer wall (c) ribbed wall..... 124

Figure 72: Contours of streamwise velocity at the center of the duct (z/D_h = 0.5). 129

Figure 73: Comparison of the streamwise velocities at y/e = 0.15 in the fully developed regions of the flow for (a) Stationary Case (b) Ro = 0.30, Near Leading Wall (c) Ro = 0.30, Near Trailing Wall 130

Figure 74: Comparison of the secondary flow contours on top of rib 9 (a) DES (b) LES 131

Figure 75: Heat transfer augmentation for the first pass of the rotating duct at the leading wall (a) DES (b) LES 132

Figure 76: Heat transfer augmentation for the first pass of the rotating duct at the trailing wall (a) DES (b) LES 133

Figure 77: (a) Heat transfer augmentation for the first pass of the rotating duct at the side wall predicted by (a) LES (b) DES (c) Development of the heat transfer at the outer side wall (0.05D_h upstream of the ribs) of the internal cooling duct (d) Comparison of the fully developed heat transfer augmentations for the stationary and the rotating cases. y = 0 represents the trailing wall and y = 1 represents the leading wall 134

Figure 78: Flow in the U-bend connecting the first and the second passes of the duct at three different vertical locations..... 136

Figure 79: Secondary flow at the center of the 180º bend for the rotating duct 137

Figure 80: Heat transfer augmentation in the vicinity of the U bend..... 138

Figure 81: Comparison of the friction factor as predicted by the present computations with LES and fully developed flow predicted by DES.....140

Figure 82: Locations of pressure taps in the two-pass duct used for comparison with experimental data by Prabhu and Vedula (Comparison in Table 9). 141

Figure 83: Ribbed averaged heat transfer at the leading wall 142

Figure 84: Ribbed averaged heat transfer at the trailing wall.....143

Nomenclature

Ar	Archimedes Number (= $g\beta\Delta TL/U_0^2$)
AR	Aspect ratio (= W/H)
Bo	Buoyancy number (= $\Delta\rho/\rho . r/D_h .Ro^2$)
C_{DES}	DES Constant
C_p	specific heat
D_h	hydraulic diameter
e	rib height
f	Fanning friction factor
g	Acceleration due to gravity
H	Backward facing step height
h	Height of the channel, upstream of the backward facing step
K	Pressure drop defined in Prabhu and Vedula (=$(P_Y-P_{in})/(½\rho U_0^2)$)
k	thermal conductivity (W/mK)
L	Height of the cavity
L_x	Length of domain in x-direction
Nu	time averaged local or surface averaged Nusselt number
p	fluctuating, modified or homogenized pressure
P	total pressure OR rib pitch
P_{in}	Pressure at the inlet of the duct
Pr	Prandtl number ($=\mu C_p / k$)
P_Y	Local pressure at the pressure tap
Q_x	Calculated flow rate in streamwise direction
$q"$	constant heat flux boundary condition on duct walls and rib
r	Outward radial distance from the center of rotation
Re	Reynolds number based on bulk velocity (= U_0h/υ)
Ri	Richardson number (= $\beta q"r/k\ Ro^2$)
Ro	Rotation number based on bulk velocity (= $\Omega h/U_0$)
S	Spanwise width of the cavity
T	Local temperature in the cavity
T_0	Temperature of cold wall
T_H	Temperature of hot wall
TKE, k	Turbulent kinetic energy
t_{LES}	Fraction of time when the region is evaluated in LES mode

u,v,w	Cartesian velocity vector
U_0	Mean bulk velocity
W	width of the channel upstream of the backward facing step, width of the cavity
X, Y, Z,	
x, y, z	physical coordinates
β	mean pressure gradient OR Thermal expansion coefficient
β^*	Modeling constant in the k-ω or SST equation
γ	Mean temperature gradient OR modeling constant in the k-ω equation
Δ	Grid length scale ($^+$ - Wall normal direction, $^{\parallel}$ - Wall parallel direction)
δ	Kronecker delta
ΔK	Non-dimensional pressure difference between two probes
ΔT	Difference in temperature
ε_{ijk}	Permutation tensor
θ	Non-dimensional temperature
κ	Non-dimensional frequency
ρ	Density of the fluid in the duct
Ω	angular velocity of rotation (rad/s) about z-axis
ω	specific dissipation rate of TKE

Subscripts

0	smooth duct
b, ∞	bulk
s	surface
t	turbulent quantities
τ	quantities based on friction velocity

1 Introduction

Despite the continual development of computational schemes to predict turbulent flows over the last few decades, the computation of highly unsteady, separated flows at high Reynolds number flows is still a major challenge. Reynolds Averaged Navier Stokes (RANS) approaches have been traditionally applied to a variety of flows. This approach is cost effective but in spite of several improvements in RANS models, they are not able to predict flows far from their calibration regime. Some of the shortcomings of RANS are listed below:

1. Real-life flows subjected to massive separation are an Achilles heel for most of the popular eddy viscosity turbulence models. The eddies in the separated region are geometry dependent and so the turbulence is anisotropic in nature. The popular eddy-viscosity models are based on the Bousinnesq approximation[1] that assumes isotropy of turbulent flows at larger anisotropic turbulent scales. This results in an inaccurate prediction of the flow.
2. Linear eddy viscosity RANS models assume that the anisotropy tensor is aligned with the mean rate-of-strain tensor, given as $a_{ij} = \langle u_i u_j \rangle - (2/3)k\delta_{ij} = -2\nu_t S_{ij}$ (Pope, 2001). This assumption is observed to be invalid even for simple shear flows and so these models fail to predict the response of the Reynolds stresses to the effects of surface curvature, system rotation, thermal gradients etc.
3. As the grid is refined in a RANS calculation, the calculation converges to a smooth solution of the RANS model. However the solution cannot be improved beyond a limit as it is restricted by the performance of the turbulence model.

[1] See Section 3.2

Large Eddy Simulation (LES) is a viable alternative for accurate computations. However the near wall resolution required for LES makes it prohibitively expensive at high Reynolds numbers. Though RANS models are relatively inaccurate and not always logically robust, the computational time associated with it gives it a competitive advantage for several industries using CFD. This is the rationale behind the recent interest and application of hybrid RANS-LES methods, which combining the advantages of both LES and RANS can give reliable predictions at a reasonable cost.

Out of this family of hybrid techniques, Detached Eddy Simulations (DES) is a technique which has gained popularity since it was proposed in 1997 (Spalart *et al.*). DES involves sensitization of a RANS model to grid length scales, thereby allowing it to function as a sub-grid scale model in the region of interest, where RANS is known to be inadequate (as in separated region). The use of LES in the critical regions, allows the natural instabilities of the flow in this region to develop. A finer grid (in the region of interest) allows the energy cascade to grow and improves the quality of the solution in this region.

This technique, initially proposed based on the Spalart – Allmaras turbulence model, treats the inner wall layer in a RANS mode and by modifying the length scale in the destruction term the model switches to a sub-grid type formulation in regions away from the wall. This eliminates the fine grid resolution needed in wall parallel directions to resolve the small scale turbulent eddies responsible for production of turbulence, which results in considerable cost savings.

Later this technique was generalized by Strelets (2001) who defined an analogous DES formulation for the Menter's Shear Stress Transport model. By this modified

definition, DES is made more sensitive to the local flow features by defaulting to a RANS solution in regions (even away from the wall) where the turbulent length scale is less than the grid length scale.

DES has been used in the prediction of a wide range of flow regimes, especially for high Reynolds number flows undergoing separation. The first application of DES after it was proposed was in 1999 when Shur *et al.,* applied DES to the study of flow around a NACA0012 airfoil at high angles of attack. DES was subsequently used by Travin *et al.,* (2000) to predict the flow past a circular cylinder and Constantinescu *et al.,* (2000, 2002) to predict the flow around a sphere. These geometries belonged to a class of separated flows where the separation is not fixed by the geometry and so the prediction of the three-dimensional separation is a challenge for the prediction scheme. The three dimensional time dependent flow in the wake of these geometries was predicted well by DES in both these cases, which proved to be a motivating factor for the further application of DES.

DES was further extended to flow around other complex geometries. Viswanathan *et al.,* (2003) applied DES to the flow around an aircraft forebody to consider the stability and control of the aircraft at high angles of attack. This study performed for a high Reynolds number was significant as it was representative of realistic flight conditions. The effect of mesh refinement was highlighted in this study and it was observed that as the mesh was refined in the detached regions of the flow, a wider range of scales were resolved. Kotapati-Apparao *et al.,* (2003) used DES to accurately predict the complex physics in the aft of a prolate spheroid undergoing a pitchup maneuver. The primary and the secondary separation observed in experiments, which URANS failed to capture, were captured accurately by DES.

Forsythe *et al.,* (2002) carried out a study of the flow around an F-15 aircraft at a high angle of attack. In this study, DES and URANS were compared and the superiority of DES in predicting the turbulent structures around the aircraft was highlighted. The effects of DES on mesh and time step refinement was also studied. Similar DES studies were carried out on other aircrafts (2002, 2003) to study wing stall and vortex bursts. Kapadia *et al*., (2003) used DES to model the flow behind an Ahmed car model. This study applied DES to a mildly separated case which was prone to reattachment, and thus broadened the application base of DES.

Though diverse in application, one common feature of the above flows is that these flows pertain to external flow regimes undergoing separation, for which DES was originally proposed. The first study which applied DES to internal flows was reported by Nikitin *et al* (2000) with the Spalart-Allmaras model. The wall parallel grid was sufficiently coarse that DES behaved as a sub-grid scale model with a built in wall function. The modeled and the resolved turbulent shear stresses in the channel were studied and the effect of the grid spacing on turbulent shear stress evaluated.

In order to claim that DES is indeed an overall effective tool for the solution of turbulent flows; a few questions still remain to be answered.

1. As in unbounded external flows, can DES be applied to solve internal, non-canonical flows that are of relevance to practical industrial applications? Is this application computationally less intensive than an equivalent LES computation?
2. Can DES capture the effects of additional strains like rotation and buoyancy, which has been a major challenge for the popular RANS models for over three decades?

This dissertation is the first attempt to answer these questions by applying DES to study the flow in stationary and rotating ribbed ducts used for the internal cooling of turbine blades.

1.1 Problem Description

This dissertation is a part of the project "***Enhanced Prediction Techniques based on Time-accurate Simulations for Turbine Blade Internal cooling***" which aims at developing and applying Large Eddy Simulations (LES) and Detached Eddy Simulations (DES) as high-fidelity prediction tools for the analysis of flow and heat transfer in stationary and rotating gas turbine blade internal cooling passages. The main objective of this part of the project is three fold – to extend and verify DES to a non-canonical internal flow configuration; to investigate the performance of DES in predicting the effects of rotation induced Coriolis forces; and to assess the capability of DES in predicting flows influenced by buoyancy.

A picture of the cross-section of a typical gas turbine blade and a schematic diagram with the region of interest is shown in Figure 1. The cross-section shows cooling air passing through a circuit of serpentine passages in which turbulence is promoted by ribs and pin fins before exiting through film cooling holes located at the surface of the blade. The design of these internal cooling passages in turbine blades and nozzles requires a detailed knowledge of the flow and heat transfer phenomena.

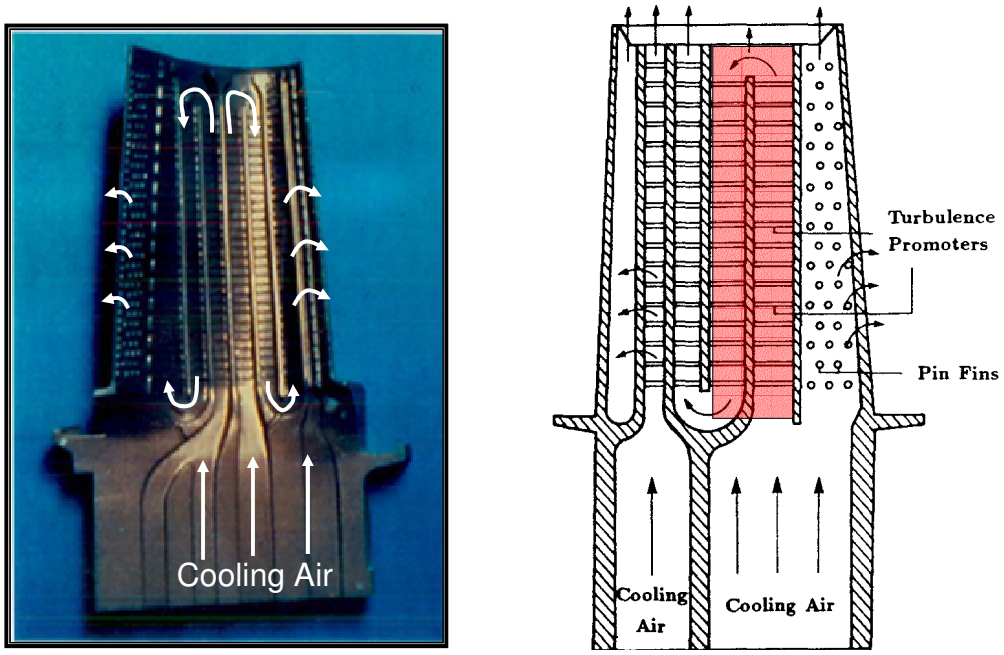

(a) **(b)**

Figure 1: (a) The cross-section of the first stage rotating blade used in the Siemens - Westinghouse 501-F Engine (Courtesy: Howard, G., O'Brein, W.F.,) (b) Schematic diagram of the turbine balde cross-section (Han, J.C., 1988) showing the region of interest[+]

The local flow and heat transfer in these internal cooling passages are a function of several geometric parameters that characterize the shape of the duct and the ribs such as the rib height, the aspect ratio of the duct, the distance from the inlet and the bends in the duct, alignment and arrangement of the ribs. Apart from these geometrical parameters, rotation and differential heating also influence the flow and heat transfer in the duct. Rotation affects the turbulence levels at the leading and trailing surfaces and introduces asymmetry in the flow and heat transfer distributions. The unequal heat transfer distribution at the leading and trailing surfaces results in temperature gradients inside the duct. This gives rise to centrifugal buoyancy that aids or opposes the effects of Coriolis forces.

[+] Figures reproduced with permission from Dr. Walter O'Brein, Mr. G. Howard and ASME

Under normal operating conditions, the typical Reynolds number (ratio of inertial and viscous forces) for the flow in internal cooling ducts, range from around 5,000 to a value of around 100,000. The rotation number (ratio of rotation to momentum) ranges from around 0.1 to values up to 0.5 and the typical local buoyancy number (rotation of buoyancy forces to inertial forces) can reach as high as values 1.0. For aerospace propulsion purposes the Reynolds number and rotation numbers are lower than the values in turbines used for power generation. The conditions used for this study are in the operating range of both propulsion and power generation gas turbines.

Since this is the first study that applies DES to capture the effects of rotation and buoyancy in the flow and heat transfer distribution, initial validation has been carried out on simple canonical geometries of a backward facing step and a buoyant cavity flow. The capability of DES in predicting separation and reattachment under stationary and rotating conditions in a backward facing step and the effects of buoyancy in cavity flows are validated and reported in Chapter 4. Having validated the capability of DES in predicting the effects of Coriolis forces and buoyancy, DES computations were then extended to the fully developed flow in a ribbed internal cooling duct under stationary and rotating conditions. Chapter 5 details these calculations. The ultimate challenge is to assess the capability of DES in predicting the flow and heat transfer in a complete two pass duct under stationary and rotating conditions. This study is reported in Chapter 6 focuses on the developing region of the flow, the 180 degree bend region and the flow and heat transfer in the second pass of the duct. Finally, Chapter 7 concludes and summarizes the work.

Thus, this work extends DES to flow regimes beyond the massively separated external flow regimes for which DES was initially proposed. This extension of DES will continue to motivate the application of DES to other complex flows. Possible candidates include rotating flows (e.g. flows in impellers, blades), flows with buoyancy effects (e.g. indoor air quality analysis, atmospheric and oceanic flows) and complex turbulent flows in internal flow regimes (e.g. flows in engine cooling jackets) where the performance of RANS has been inconsistent and applying LES is expensive considering the current computational capabilities.

2 Literature Review

In spite of the developments in CFD over the past three decades the problem of turbulence is far from being solved. The most popular practice of turbulence modeling in industry is to solve the Reynolds Averaged Navier Stokes (RANS) equations to obtain the mean flowfield in complicated geometries. Though RANS models are not highly reliable and are often not dependable for complex flows, the need for quick turnaround in an industry setting compels the adoption of RANS as the primary tool for turbulence modeling. High fidelity solutions are feasible using Direct Numerical Simulations (DNS) and Large Eddy Simulations (LES). However the implementation of these strategies, especially for high Reynolds number flows is demanding in terms of computational resources.

This chapter presents a review of the literature in the development of turbulence modeling relevant to massively separated flows that are affected by rotation and buoyancy. Of particular interest is the aero-thermal prediction of turbulent flow in the internal cooling passages of gas turbine blades, where the flow and heat transfer are strongly dependent on the prediction of separation and reattachment, primary and secondary effects of rotation induced Coriolis forces and buoyancy driven by the temperature gradients.

The review is primarily divided into three sections. This first section describes the modeling of the turbulent internal flow in stationary geometries. Some of the attempts to capture the effects of rotation induced Coriolis forces using eddy-viscosity models are described in the second section. The final part of the review focuses on the prediction

capabilities of the turbulence modeling strategies when applied to flows in the presence of buoyancy driven by temperature gradients.

2.1 Stationary Internal Flows

The flow behind a rib (turbulator) though geometrically simple, has some complex features: separation of the boundary layer, a curved shear layer, primary and secondary recirculation, reattachment of the boundary layer, recovery etc. These complex features of the flow pose a big challenge in the numerical prediction of the flow. Most of the reported computational predictions in stationary ducts are focused on the solution of the Reynolds-Averaged Navier Stokes (RANS) equations. Different closure models have been used, and it has been observed that while eddy-viscosity models which assume isotropy of turbulence (Prakesh and Zerkle, 1995) fail to capture the flow accurately, more advanced models based on the full Reynolds stress closures have performed reasonably well (Jia *et al,* 2002.).

Several investigators have used the linear k-ε model to study the flow in a backward facing step which is a canonical test case for evaluating models in separating flows. Studies on backward facing step (Driver, 1985; Amano, 1995) show that the turbulent viscosity and the turbulent shear stress are usually over-predicted by the k-ε two equation models. This results in a rapid spreading of the shear layer with early reattachment. Driver and Seegmiller (1985) studied the effect of the turbulent models in predicting the flow in a diverging channel with a backward facing step by conducting experiments and numerically comparing the results using a linear k-ε model, algebraic stress model (ASM) and Reynolds stress models (RSM) models, for a Re_θ = 5000. Similar computational exercise was carried out by Amano and Goel (1985). The prediction of the flow in a

backward facing step was the test case at the 1980-81 AFOSR-HTTM Stanford Conference on Turbulence. The numerical studies presented using the k-ε model predicted a reattachment in the range of 5.2h to 5.5h (h- height of the step) as compared to a value of 7.0h from the experiments. Menter (1993) applied four, two equation eddy viscosity turbulence models – the k-ε model, the 1988 k-ω model and Menter's Baseline model (BSL) and shear stress transport (SST) model to study the flow downstream of the backward facing step. It was observed that the k-ω model, the BSL model and the SST model performed significantly better than the k-ε model.

Liou *et al*. used a k-ε ASM to predict flow in a stationary 2D ribbed duct with ribs on one wall. Their studies showed that the k-ε model fails to predict the flow accurately while the k-ε-A model, which accounts for the anisotropy of turbulence, gives reasonable results. Saidi *et al*. (2001) also used k-ε models in a periodic channel with inline orthogonal ribs, and the computations showed mixed results. Iacovides (1991) carried out computations using k-ε and a low-Re zonal differential stress model (DSM) in a periodic ribbed duct. Though a reasonable flow behavior was predicted by the k-ε model, the thermal behavior was not predicted accurately. The low-Re DSM model gave better predictions than the k-ε model. Iacovides and Raisee (1999) introduced a modified version of the Yap correction to the low-Re DSM models and obtained reasonable heat transfer results in a 180° bend channel. Ooi *et al*. (2002) present predictions using a v^2-f model on orthogonal in-line ribs and found that the model performs better than the k-ε and Spalart – Allmaras (S-A) RANS models.

Apart from the RANS models, high fidelity computations using LES have also been applied to internal cooling duct geometries. Watanabe and Takahashi (2002) carried out

LES computations and experimental studies on a rectangular channel with transverse ribs and got good agreement with the experiments. The studies also revealed the unsteady mechanism that enhanced the heat transfer in the ribbed channel. Tafti (2005) used 96^3 and 128^3 grids to predict the heat transfer in a channel with orthogonal ribs with a pitch to rib height ratio (P/e) of 10 and a rib height to hydraulic diameter (e/D_h) of 0.1. The computations also gave a comprehensive knowledge of the major flow structures in the flow field and compared very well with experiments.

2.2 Modeling the Effect of Coriolis Forces

Rotation (or streamline curvature) generates extra strain rates that significantly affect the turbulent stress production. Bradshaw (1969) formulated an analogy between meteorological parameters and the parameters describing rotation about the axis normal to the plane of rotation. Bradshaw defined an effective Richardson number (Ri) for flows undergoing rotation which is linearly related to the mixing length ($l = l_0(1 - \beta \mathrm{Ri})$). Most of the later studies also propose a similar definition. Bradshaw (1988), Ishigaki (1996) discuss the analogy between the effects induced by curvature and orthogonal rotation in turbulent flows. When the direction of rotation of the fluid element is the same as the angular velocity of the system (or in a flow over a convex surface) the flow is stable while the flow is unstable if the directions are opposing (concave surface). Linear eddy viscosity models fail to account for these effects because of the inability to reproduce normal stresses that appear in the production term. So these effects are modeled by *ad hoc* corrections using a rotation Richardson number.

Wilcox *et al.* (1977), proposed a modified version of the k-ε equation, where they modeled the Coriolis term in the k-equation as a function of the system rotation. The

model was applied for rotating channel flow and cases with streamline curvature. The predictions were within 10% of the measured results. Launder *et al.* (1977) simulated the effects of curvature by making one of the coefficients in the transport equation for ε, a function of the rotational Richardson number ($C_c = C_{\varepsilon 2}$ (1 – 0.2Ri)). The model was applied to a variety of boundary layer flows developing over spinning and curved surfaces. The agreement was only satisfactory but better than that under conditions when rotational effects were not modeled.

Howard *et al.* (1980) used Wilcox's model (1977) and Launder's model (1977) to compute the flow in high and low aspect ratio ducts. For the high aspect ratio duct case the simulation was carried out for rotation numbers ranging from Ro = 0 to 0.42. Launder's model was observed to be unstable at high rotation numbers. All the comparisons moderately agreed with the experimental results but were not accurate. For the low aspect ratio case it was observed that the predicted velocity profiles did not agree quantitatively with the experiments although the shape of the profile was correctly predicted. Rodi *et al.* (1983) used extensions of k-ε models – an ASM and two modified versions of ε equation proposed by Launder *et al.* (1977) and Hanjalic *et al.* (1980), to predict flows in a curved boundary layer, a curved mixing layer and a curved wall jet. It was observed that with curvature corrections the flow in the separated region was accurately captured. However the flow predictions in the recovery region were incorrectly predicted by all the models.

Chima (1996) proposed a modified two equation k-ω turbulence model by writing the production terms in both the k and the ω equations in terms of vorticity. The model was applied to transonic flows over a flat plate, over a compressor and over a turbine vane.

The results compared well with the experiments but were not substantially better than the computations using Baldwin-Lomax model (1978) for the cases considered.

Hellsten (1998) suggested improvements in the k-ω SST model (Menter., 1992, 1993), by modifying the coefficient of the production term in the k-equation. The production term was divided by a factor ($C_{\omega 2} = 1/(1 + C_{rc}Ri)$) to incorporate the effects of rotation. The model was tested for a spanwise rotating channel. It was observed that for high rotation numbers (Ro = 0.21, 0.42), the location of maximum velocity point is predicted too near the suction side wall. Also the correction seemed to have a minor impact on the results in many of the other cases (personal communication).

A numerical study of fully developed flow in a rotating rectangular duct was performed by Iacovides and Launder (1991). Ducts with a square cross section and with an aspect ratio of 2:1 were studied. The Reynolds number varied from 33,500 to 97,000 and the rotation number ranged from 0.005 to 0.2. The standard high Reynolds number $k-\varepsilon$ model was used for the bulk of the flow. Near the wall, a low Reynolds number one-equation model was used. The calculations correctly predicted the secondary flow caused by Coriolis forces. However, there was only a qualitative match between the computed and experimental heat transfer results.

Bo *et al.* (1995) studied developing flow in an orthogonally rotating square duct. The rotation numbers were 0.12 and 0.24. Three turbulence models were used in the analysis: a $k-\varepsilon$ eddy viscosity model with a low Reynolds number one-equation EVM near the wall, a low Reynolds number algebraic stress model (ASM), and a low Reynolds number $k-\varepsilon$ EVM. Results from the low-Re $k-\varepsilon$ EVM for both constant and variable density were very unrealistic and were not pursued any further. The $k-\varepsilon$/one-equation EVM

generally performed well for low rotation, but results deviated substantially from experimental results on both leading and trailing sides for the high rotation number case.

Prakash and Zerkle (1995) used the standard $k-\varepsilon$ model to simulate outward flow and heat transfer in a smooth square duct with radial rotation. Coriolis and buoyancy forces were included only in the mean equations. The Reynolds number was kept at 25,000 and the rotation numbers were 0.24 and 0.48. The simulations did not match trends from experimental data. The authors attributed the quantitative disagreement to the need for including rotation effects in the $k-\varepsilon$ model.

Rigby (1998) used Chima's k-ω model to predict the flow in a rotating internal cooling passage with a 180 degree turn and ribbed walls. Reynolds numbers in the range 5200 to 7900 were tested for two rotation cases (Ro = 0 and 0.24). The predictions for the rotation cases were not accurate. The mass transfer was over predicted in the first leg and was under-predicted in the second leg.

In general it has been observed that the linear eddy viscosity models fail to predict the response of the turbulent stresses to flows undergoing rotation. Though several modifications have been proposed to sensitize the model to rotation, the linear eddy viscosity models are still not free from defects. The studies presented in chapters 4.1, 5.4 and 6.2 show how a small switch in the turbulence length scales in the 1988 k-ω and Menter's SST two equation models, to obtain a DES formulation drastically improves the prediction capabilities of these linear eddy-viscosity models.

2.3 Modeling the Effect of Buoyancy Forces

Bradshaw (1969) studied the effects of buoyancy in turbulent flow and came up with an analogy that related it to flows with curvature. He formulated a flux buoyancy term

which he defined as the ratio of the turbulent energy production by buoyancy forces to the production by shear forces. The flux Richardson number, as defined by Bradshaw (1969) is given by $Ri_f = g\left(\overline{\theta' v'} \Big/ \overline{\theta} \Big/ \overline{u' v'} \partial U \Big/ \partial y\right)$. The total turbulent kinetic energy production in the TKE equation is then modified as $\tau_{xy}\left(\partial U \Big/ \partial y\right)(1 - Ri_f)$. Several forms of this term have been used widely in the studies on flows with buoyancy and the equivalent two-equation *k-ω* model reduces to a form

$$\frac{\partial k}{\partial t} + U_j \frac{\partial k}{\partial x_j} = (1 - Ri_f)\tau_{ij} \frac{\partial U_i}{\partial x_j} - \beta^* k + \frac{\partial}{\partial x_j}\left[\left(\nu + \sigma^* \nu_T\right)\frac{\partial k}{\partial x_j}\right]$$

$$\frac{\partial \omega}{\partial t} + U_j \frac{\partial \omega}{\partial x_j} = (1 - c_{\omega 3} Ri_f)\alpha \frac{\omega}{k} \tau_{ij} \frac{\partial U_i}{\partial x_j} - \beta \omega^2 + \frac{\partial}{\partial x_j}\left[\left(\nu + \sigma \nu_T\right)\frac{\partial \omega}{\partial x_j}\right]$$

Similar formulations have been proposed for the *k-ε* models. Different values of $c_{\omega 3}$ ($c_{\varepsilon 3}$ in a *k-ε* model) have been used in the literature which are described below and are tabulated in Table 2.

Several studies in atmospheric and oceanic sciences have been reported which apply eddy viscosity turbulence models to compute flows with buoyancy. Koutsourakis *et al.,* (2003) presented the various methodologies applied in the field of atmospheric dispersion. The RANS models described in the paper are based on the flux Richardson number which is used to model the effects of buoyancy. Hassid (2002) studied the behavior of four turbulence models in stratified flows. The behavior of the model was observed to be dependent on the gravitational production term in the turbulent dissipation equation ($C_{\varepsilon 3}$). Stips *et al.,* (2002) studied the temperature field and spatial dynamics of

flow in a lake using a two equation k-ε model. The value of $C_{\varepsilon 3}$ was based on the Brunt-Väisälä frequency which is the frequency of the buoyancy waves in the flow. Deficiencies in predicting the spatial dynamics were observed in spite of a flux Richardson number being introduced to model the effect of buoyancy.

Another area where the effects of buoyancy forces are extensively studied is the flow in two-dimensional cavities. Sharif and Liu (2003) applied low Reynolds number k-ε and k-ω models to study the turbulent natural convection in moderately high Rayleigh number flows in a two dimensional cavity inclined at various angles. No additional terms were used to model the buoyancy effects. It was observed that the k-ω model performed better than the k-ε model. Peng and Davidson (1999) used low Reynolds number k-ε and k-ω models to compute the turbulent buoyant convection flows in rectangular and square cavities. Based on arguments by earlier researchers that the results are insensitive to the value of $C_{\omega 3}$, the term was set to zero. None of the models used showed a grid independent solution. To and Humphrey (1986) used a modified version of the k–ε equation with a flux Richardson number and an algebraic stress model to model free and mixed convection flows in cavities.

Shankar *et al.,* (1995) used the standard k-ε equation to study turbulent plumes and found that the standard equation without any terms for buoyancy underpredicts the spreading rate of the plume. Murakami *et al.,* (1999) used four models based on eddy-viscosity with appropriate terms incorporating the effects of buoyancy. The models fell short in predicting the flow and temperature fields accurately. Hanjalic *et al.,* (1996) studied the flow and heat transfer in two dimensional partitioned enclosures using eddy

viscosity based three and four equation models. The models showed good agreement with the experiments, but extra equations with more empirical constants were used.

Several other studies are also available which use a similar approach as mentioned above to model atmospheric and oceanic flows, indoor air flows (Plett *et al.,* 1993, Yeoh *et al.,* 2002) and cavity flows (Hanjalic *et al.,* 2001). Zhao *et al*., (2001) used the *k*-ε equation in conjunction with the temperature variance model and studied the effects of the closure terms in predicting turbulent buoyant shear flows. Kantha (2004) studied the various length scale equations which are used in conjunction with the *k*-equation and showed that all the equations are equivalent.

Several studies on the effects of centrifugal buoyancy in internal cooling ducts have also been reported. Lin *et al*. (2001) studied the three dimensional flow and heat transfer in a U-shaped duct under stationary and rotating conditions for a Reynolds number of 25,000 and a density ratio ($\Delta\rho/\rho$) of 0.13. Menter's shear stress model was used for closure. The evolution of flow and the effect of Coriolis forces, centrifugal buoyancy, staggered ribs and the 180 degree bend were studied. However the average heat transfer augmentation showed only moderate agreement with experimental results.

It is observed that an additional buoyancy term is required in the turbulence equations to model the effects of buoyancy. Despite the widespread application of these RANS models it is observed that the coefficient of the additional production term in the *k* and the ω (or ε) equations are tailored for each individual application. Some of the coefficients used in the equation are shown in Table 2.

Table 2: Variation in the coefficient of the buoyancy production term in the ω or ε equation used by different groups[2]

Author (year)	$c_{\varepsilon 3}$ or $c_{\omega 3}$
Peng & Davidson (1999), Sharif & Liu (2003)	0
Stips et al., (2003)	-0.629 if N2 > 0 1.000 if N2 < 0
To & Humphrey (1986), Hanjalic et al., (1996), Murakami et al., (1999), Zhao et al., (2001), Umlauf et al., (2003)	1.44
Murakami et al., (1999)	1.50
Shankar et al., (1995)	4.44
Rodi (1980), Peng & Davidson (1999), Hassid (2002), Sharif & Liu (2003)	tanh |v/u|

While RANS suffers this deficiency LES has been applied by several researchers to predict the effects of buoyancy. Abdel-Wahab and Tafti (2004b) validated the LES Dynamic Smagorinsky model for a ribbed duct with Coriolis and buoyancy forces. Ribs with a $P/e = 10$ and $e/D_h = 0.1$ were studied and some of the hydrodynamic and turbulent characteristics of the flow, which are difficult to obtain through experiments were

[2] Some authors used more than one value of $c_{\varepsilon 3}$/ $c_{\omega 3}$ to study the effect of these terms. All the values used have been tabulated.

highlighted. The heat transfer at the leading wall was observed to decrease as the rotational speed increases but increased along the trailing wall of the rotating duct. The computed data compared well with experimental results. Murata and Mochizuki (2001a) studied the effect of buoyancy in ribbed ducts with ribs aligned at an angle of 90º and 60º with the flow direction. While it was observed that the friction factor increases with buoyancy in the 90º case, it decreases for the duct with 60º ribs. The heat transfer at the trailing surface was observed to increase as buoyancy is increased. While the computations listed above were carried out in periodic domains, a handful of LES computations have been reported that have been carried out on complete two pass ducts. Murata and Mochizuki (2001b) carried out computations for a rotating two pass ducts at Re < 5,000 and studied the effects of buoyancy. Buoyancy increases the heat transfer at the trailing surface in the region upstream of the bend and at the leading surface. LES computations for developing flow and heat transfer in rotating ducts have also been carried out by Sewall and Tafti (2005b) at Re = 20,000, with and without the inclusion of centrifugal buoyancy forces. It was observed that as the buoyancy parameter was increased from a value of 0 to 0.25 the heat transfer at the leading surface decreases. However as the buoyancy increases further it was observed that the heat transfer increases.

From the studies presented that use linear eddy viscosity models to predict the effects of buoyancy, it is observed that a buoyancy production term is added to the turbulence equations to account for the extra strain rates generated by buoyancy. However there is a lack of consensus in the turbulence constant used by the different studies. LES studies present a consistent trend in the predictions without any additional modeling for

buoyancy. However the cost of performing LES is a major concern. Chapters 4.2 and 5.5 present studies where DES is applied to study the effects of buoyancy. These study show that by switching from a RANS computation to a LES in regions of interest, buoyancy can be modeled without explicitly defining extra buoyancy modeling terms. These computations also show that the DES grid requirements are less rigorous than LES and so is feasible using the current computational capabilities.

3 Computational Model and Governing Equations

This chapter describes the computational details. The sections below outline the governing conservative equations, the turbulence closure equations and the boundary conditions applied. Details of post-processing the information obtained from the calculations are also explained in detail in the last part of this chapter.

3.1 Mean Flow and Energy Equations

The governing flow equations are non-dimensionalized by a characteristic length scale and a characteristic velocity scale. The energy equations are non-dimensionalized by a characteristic temperature scale. The characteristic length scale, velocity scale and the temperature scale are listed for the cases studied are listed in Table 3. On substitution into the Navier-Stokes and energy equations, the non-dimensional time-dependent equations take the following conservative form[3]:

Continuity:

$$\frac{\partial}{\partial x_j}\left(U_j\right) = 0$$

Momentum:

$$\frac{\partial}{\partial t}\left(u_i\right) + \frac{\partial}{\partial x_j}\left(U_j u_i\right) = -\frac{\partial}{\partial x_j}\left(p\right) + \frac{\partial}{\partial x_j}\left(\left(\frac{1}{\mathrm{Re}} + \frac{1}{\mathrm{Re}_t}\right)\frac{\partial u_i}{\partial x_k}\right) + S_u$$

Energy:

$$\frac{\partial}{\partial t}\left(\theta\right) + \frac{\partial}{\partial x_j}\left(U_j \theta\right) = \frac{\partial}{\partial x_j}\left(\left(\frac{1}{\mathrm{Pr}\,\mathrm{Re}} + \frac{1}{\mathrm{Pr}_t\,\mathrm{Re}_t}\right)\frac{\partial \theta}{\partial x_k}\right) + S_\theta$$

[3] Henceforth, all usage is in terms of non-dimensionalized values.

The additional effects of rotation and buoyancy are incorporated in the mean flow and energy equations. The additional terms in the equations are listed in Table 3. Re_t is the turbulent Reynolds number based on the turbulent viscosity that is modeled using the k-ω model and/or Menter's SST model (Menter, 1993) in both the DES and URANS formulations.

Table 3: Extra terms in the momentum (S_u) and energy equations (S_θ) for the different cases studied

Case	Ref. Length	Ref. Velocity	Ref. Temp. (θ)	S_u	S_θ	Origin of Terms
Backward facing step	H	U_0		$-2Rou_m\varepsilon_{i3m}$		Rotation
Flow in a cavity	L	U_0	$(T-T_0)$ / (T_H-T_0)	$-Ar\,\theta\delta_{i2}$		Buoyancy
Fully developed flow – Stationary Duct	D_h	u_τ	$q''D_h/k$	$\beta\,\delta_{i1}$	γu_1	Streamwise periodicity
Fully developed flow – Rotating Duct	D_h	u_τ	$q''D_h/k$	$\beta\,\delta_{i1}$	γu_1	Streamwise periodicity
				$-2Ro_\tau u_m\varepsilon_{i3m}$		Rotation
Fully developed flow – Rotating Duct (With Buoyancy)	D_h	u_τ	$q''D_h/k$	$\beta\,\delta_{i1}$	γu_1	Streamwise periodicity
				$-2Ro_\tau u_m\varepsilon_{i3m}$		Rotation
				$-Ri_\tau(\theta-\theta_{ref})\,\delta_{i1}$		Buoyancy
Stationary Two Pass Duct	D_h	U_0	$q''D_h/k$			
Rotating Two Pass Duct	D_h	U_0	$q''D_h/k$	$-2Rou_m\varepsilon_{i3m}$		Rotation

3.2 Turbulence Models

3.2.1 *k-ω* Equations (1988 Wilcox Model)

The equations for the turbulent kinetic energy (k) and the rate of dissipation of energy per unit volume and time (ω) (Wilcox, 1988) are:

$$\frac{\partial(k)}{\partial t}+\frac{\partial(U_j k)}{\partial x_j}=\tau_{ij}\frac{\partial U_i}{\partial x_j}-\beta^* k\omega+\frac{\partial}{\partial x_j}\left[\left(\frac{1}{\mathrm{Re}}+\frac{\sigma^*}{\mathrm{Re}_t}\right)\frac{\partial k}{\partial x_j}\right]$$

$$\frac{\partial(\omega)}{\partial t}+\frac{\partial(U_j \omega)}{\partial x_j}=\gamma\frac{\omega}{k}\tau_{ij}\frac{\partial U_i}{\partial x_j}-\beta\omega^2+\frac{\partial}{\partial x_j}\left[\left(\frac{1}{\mathrm{Re}}+\frac{\sigma}{\mathrm{Re}_t}\right)\frac{\partial \omega}{\partial x_j}\right]$$

The turbulent kinetic energy and the dissipation rate are needed to define the eddy viscosity as

$$\frac{1}{\mathrm{Re}_{t_\tau}}=\gamma^*\frac{k}{\omega}$$

The Boussinesq approximation is used to define the Reynolds stress tensor in terms of the mean strain rate tensor *(S_{ij})* as

$$\tau_{ij}=\frac{2}{\mathrm{Re}_{t_\tau}}\left[S_{ij}-\frac{1}{3}\frac{\partial U_k}{\partial x_k}\delta_{ij}\right]-\frac{2}{3}k\delta_{ij}\,.$$

The closure coefficients and the auxiliary relations are defined as

$$\gamma=5/9\,,\qquad \beta_0=3/40\,,\qquad \beta^*=0.09\,,$$

$$\gamma^*=1\qquad \varepsilon=\beta^*\omega k\qquad \sigma=\sigma^*=1/2$$

3.2.2 Menter's Baseline Model

A major shortcoming of the k-ω model is the sensitivity to the freestream values specified outside the shear layer. To overcome this freestream dependency and to retain a reliable form, a zonal technique that acts as k-ω in the inner part of the boundary layer and gradually changes to a k-ε model in the farfield was proposed by Menter (1992,

1993). This model, known as Menter's Baseline Model (BSL), uses a blending function that gradually changes from 1 in the *k-ω* region to 0 in the *k-ε* region. The *k-ω* equations in a transformed *k-ε* form, introducing a cross-diffusion term are:

$$\frac{\partial(k)}{\partial t}+\frac{\partial(U_j k)}{\partial x_j}=\tau_{ij}\frac{\partial U_i}{\partial x_j}-\beta^* k\omega+\frac{\partial}{\partial x_j}\left[\left(\frac{1}{\mathrm{Re}}+\frac{\sigma_k}{\mathrm{Re}_t}\right)\frac{\partial k}{\partial x_j}\right]$$

$$\frac{\partial(\omega)}{\partial t}+\frac{\partial(U_j \omega)}{\partial x_j}=\gamma\frac{\omega}{k}\tau_{ij}\frac{\partial U_i}{\partial x_j}-\beta\omega^2+\frac{\partial}{\partial x_j}\left[\left(\frac{1}{\mathrm{Re}}+\frac{\sigma}{\mathrm{Re}_t}\right)\frac{\partial \omega}{\partial x_j}\right]+2(1-F_1)\sigma_{\omega 2}\frac{1}{\omega}\frac{\partial k}{\partial x_j}\frac{\partial \omega}{\partial x_j}$$

The constants for the model are calculated using the *k-ω* and *k-ε* constants and using the blending function in the region of transformation as:

$$\phi=F_1\phi^{k-\omega}+(1-F_1)\phi^{k-\varepsilon}$$

The constants for the *k-ω* Wilcox model are:

$$\sigma_{k1}=0.5,\qquad \sigma_{\varpi 1}=0.5,\qquad \beta_1=0.075,$$

$$\kappa=0.41\qquad \beta^*=0.09\qquad \gamma_1=\beta_1/\beta^*-\sigma_{\omega 1}\kappa^2/\sqrt{\beta^*}$$

The constants for the standard *k-ε* model are:

$$\sigma_{k1}=1.0,\qquad \sigma_{\varpi 1}=0.856,\quad \beta_2=0.0828,$$

$$\kappa=0.41\qquad \beta^*=0.09\qquad \gamma_2=\beta_2/\beta^*-\sigma_{\omega 2}\kappa^2/\sqrt{\beta^*}$$

The blending function F_1 is defined as

$$F_1=\tanh(\arg_1^4)$$

with

$$\arg_1=\min\left(\max\left(\frac{\sqrt{k}}{0.09\omega y},\frac{500}{\mathrm{Re}_\tau y^2\omega}\right);\frac{4\sigma_{\omega 2}k}{CD_{k\omega}y^2}\right)$$

where y is the distance to the nearest surface and CD_{kw} is the cross-diffusion term. The eddy viscosity and the stress tensor are defined in the same manner as in Wilcox's k-ω equation.

3.2.3 Shear-Stress Transport (SST) Model

The SST model was devised from the BSL model to account for the transport of the shear stresses. Inspired by the Johnson-King turbulence model, the SST model assumes that the principal shear stress is proportional to the total kinetic energy. The SST model has a better sensitivity to adverse pressure gradients as compared to the BSL model. The formulation of this model is similar to the BSL model, with some changes in the modeling constants.

$\sigma_{k1} = 0.85,$ $\sigma_{\varpi 1} = 0.5,$ $\beta_1 = 0.075,$

$\kappa = 0.41$ $\beta^* = 0.09$ $\gamma_1 = \beta_1 / \beta^* - \sigma_{\omega 1} \kappa^2 / \sqrt{\beta^*}$

The eddy-viscosity is defined as

$$\frac{1}{\mathrm{Re}_{t_\tau}} = \frac{a_1 k}{\max(a_1 \omega; \Omega F_2)}$$

where a_1 is a constant, Ω is the absolute value of vorticity and F_2 is given by

$$F_2 = \tanh(\arg_2^2)$$

$$\arg_2 = \max\left(2\frac{\sqrt{k}}{0.09\omega y}, \frac{500}{\mathrm{Re}_\tau y^2 \omega}\right)$$

3.3 Detached Eddy Simulations

A majority of the DES computations reported in the open literature use the one equation Spalart – Allmaras model as the base model. The Spalart – Allmaras based DES

model is hardwired to use RANS in the near wall region and LES away from the wall solely based on the grid distribution and so is insensitive to the local flow features. In order to facilitate the computation to be cognizant of the eddy length scales and hence behave as RANS or LES depending on the instantaneous local conditions, a two equation (k–ω, SST) model has been used to model the effects of turbulence. The formulation of the two-equation model based DES is discussed by Strelets (2001) for the SST model.

To obtain the DES form, the RANS length scale, $l_{\text{k-}\omega}$ ($=\sqrt{k}/\beta^{*}\omega$), in the two equation model is replaced by a DES length scale δ, where

$$\delta = \min(l_{k-\omega}, C_{DES}\Delta)$$

$$\Delta = \max(\Delta_x, \Delta_y, \Delta_z)$$

$$C_{\text{DES}} = 0.78$$

The resulting sub-grid model reduces into a Smagorinsky-like model (Strelets, 2001). Based on this modification, the only term that is modified is the destruction term in the turbulent kinetic energy equation and the new k-transport equation for DES is

$$\frac{\partial k}{\partial t} + \frac{\partial (u_j k)}{\partial x_j} = \tau_{ij}\frac{\partial u_i}{\partial x_j} - \frac{k^{3/2}}{\delta} + \frac{\partial}{\partial x_j}\left[\left(\frac{1}{\text{Re}} + \frac{\sigma^{*}}{\text{Re}_t}\right)\frac{\partial k}{\partial x_j}\right]$$

Hence if the grid length scale is larger than the eddy length scale, DES uses a RANS derived eddy viscosity model to treat the eddy. Thus the relaxation of the grid in the wall parallel direction ensures that the boundary layer is treated in a RANS mode, where RANS is calibrated. In addition, the model evaluates the grid density with reference to the instantaneous local turbulent length scale and accordingly switches between LES and URANS. When the grid is finer than the local instantaneous turbulent length scale, the

model behaves as a sub-grid model and eddies are directly resolved on the grid. This allows the energy cascade to extend to length scales close to the grid spacing. In contrast if the local instantaneous length scale is larger, the RANS turbulence model gains full control of the solution. One prominent feature of the DES version of the k–ω or the SST model is that although an instantaneous discontinuity may exist between the RANS region and the LES region, in the mean however a smooth transition takes place from RANS to LES and vice versa. The smooth and continuous velocity and the eddy viscosity fields make DES a non-zonal technique.

3.4 Numerical Method

The governing equations for momentum and energy are discretized with a conservative finite-volume formulation using a non-staggered grid topology. The Cartesian velocities, pressure, and temperature are calculated and stored at the cell center, whereas contravariant fluxes are stored and calculated at the cell faces. For the time integration of the discretized continuity and momentum equations, a projection method is used. The temporal advancement is performed in two steps, a predictor step, which calculates an intermediate velocity field, and a corrector step, which calculates the updated velocity at the new time step by satisfying discrete continuity. A second order central difference scheme is used to discretize the momentum and energy equations.

The DES versions of the k-ω model and/or Menter's SST are used for closure and the standard boundary conditions, as prescribed by Wilcox (1988), are used. The equations for the turbulent kinetic energy and the dissipation rate are solved using a second order central difference scheme subject to a TVD limiter. Typically the k-ω

equations are stiff and so the equations are rearranged to obtain a diagonally dominant system. The sink terms ($\beta^* k\omega$ and $\beta\omega^2$), in the turbulence equations are solved implicitly along with the diffusion terms. These terms fortify the diagonal of the system matrix to add stability to the system.

The computer program GenIDLEST (**Gen**eralized **I**ncompressible **D**irect and **L**arge **E**ddy **S**imulations of **T**urbulence) used for these simulations has been applied extensively to study air-side heat transfer augmentation in compact heat exchangers and internal cooling in gas turbines (Abdel Wahab and Tafti., 2004a, 2004b; Sewall and Tafti., 2006). Details about the algorithm, functionality, and capabilities can be found in Tafti (2001).

3.5 Post-processing

Time evolution of bulk quantities such as surface-averaged Nusselt numbers and friction factors are monitored as the solution is allowed to reach a statistically steady state. The mean characteristics of the flow are obtained by averaging the solution for an additional time. To facilitate comparison with previous experimental work all the results are normalized by the mean bulk flow velocity. The Fanning friction factor is calculated in terms of the non-dimensional pressure difference as $f = -\frac{1}{2}\frac{\Delta p}{\Delta l}$. The form drag is computed by integrating the pressure forces on the ribs. The friction losses on each of the walls and the ribs are computed by integrating the shear stresses on the surface.

For the computations on ribbed ducts, the local Nusselt number is calculated as $Nu = \frac{1}{\theta_s - \theta_{ref}}$ where θ_s is the surface temperature and θ_{ref} is the reference

temperature defined as[4] $\theta_{ref} = \frac{\iint |u_1| \theta dA_x}{\iint |u_1| dA_x}$. The surface-averaged Nusselt number is obtained by averaging the local Nusselt number as $< Nu >= \frac{1}{\iint_\Omega dS} \left[\iint_\Omega \frac{1}{\theta_s - \theta_{ref}} dS \right]$ where S denotes the surface under consideration.

The augmentation ratios in the ribbed ducts are calculated with reference to a smooth channel. The reference values for Nusselt number and friction factor for a smooth duct are obtained from the correlations (Incorpera and Dewitt, 2002) $Nu_0 = 0.023 \cdot \mathrm{Re}_b^{\,0.8} \cdot \mathrm{Pr}^{0.4}$ and $f_0 = 0.046 \cdot \mathrm{Re}_b^{\,-0.2}$

Though calculations have been carried out over the entire domain, to take advantage of the symmetry in the flow and heat transfer in the ribbed duct calculations, the data is averaged about the symmetry plane(s). The fully developed computations on a stationary duct are averaged over the *y*- and the *z*-axes and the data for a quadrant is presented. For the fully-developed rotating cases (with and without buoyancy) since the flow is asymmetric at the leading and trailing surfaces, averaging is carried out about the *z*-axis.

For the stationary two-pass duct averaging is carried out about the *y*- and the *z*-axes only for the first 9 ribs. Beyond the 9th rib the flow and heat transfer are affected by the presence of the 180 degree bend. The flow and heat transfer downstream of the bend is also asymmetric due to the asymmetry introduced by the bend. So the flow and heat transfer downstream of the 9th rib, in the bend and downstream of the bend in the second pass are all averaged about the *z*-axis. For the rotating two-pass duct, the flow and heat transfer in the first pass (upstream of the 9th rib) are averaged about the *z*-axis.

[4] For time-averaged Nusselt number θ_s and θ_{ref} are calculated from the time averaged temperature field.

4 Validation Cases – Effects of Rotation and Buoyancy

4.1 Capturing the Effects of Rotation in Sudden Expansion Channels using Detached Eddy Simulations

This section discusses the effects of rotation induced Coriolis forces on the flow physics in a backward facing step. It is observed from previous studies conducted that when the direction of rotation is in tandem with the fluid rotation vector i.e., the vorticity (or in a flow over a convex surface) the flow is stable while the flow is unstable if the directions are opposing (convcave surface). This stabilizing and destabilizing effect of rotation on the boundary layer has been studied experimentally in rotating channel flows by Johnston *et al.,* (1972) and in rotating diffusers by Moore (1973) and Rothe and Johnston (1976).

As with boundary layers, shear layers are also stabilized or destabilized by rotation. Rothe and Johnston (1979) carried out experiments on the separated flow downstream of the backward facing step, to show the effect of system rotation on a free shear layer. A three dimensional turbulent flow was observed in destabilized rotation while a more calm flow was observed in flows with strong stabilizing rotation.

Nilsen and Andersson (1990) used an algebraic second moment closure model to predict the rotational effects on backward facing step flows. It was observed that the rotation induced variation of the mean flow pattern is a result of the significant change in the turbulent fluctuations in the free shear layer. However the quantitative prediction of the reattachment lengths showed only reasonable agreement with the experimental data (Rothe and Johnston, 1979). A similar study was carried out on rotating flows using a v^2-f model by Iaccarino *et al*., (1999). Both the original and a modified version of the model

were used to predict the reattachment length downstream of a backfacing step. The modified model predicted the reattachment length better than the original model. However it was observed that the predictions of the modified model, like the ASM model of Nilsen and Andersson (1990) showed only reasonable agreement with the experiments.

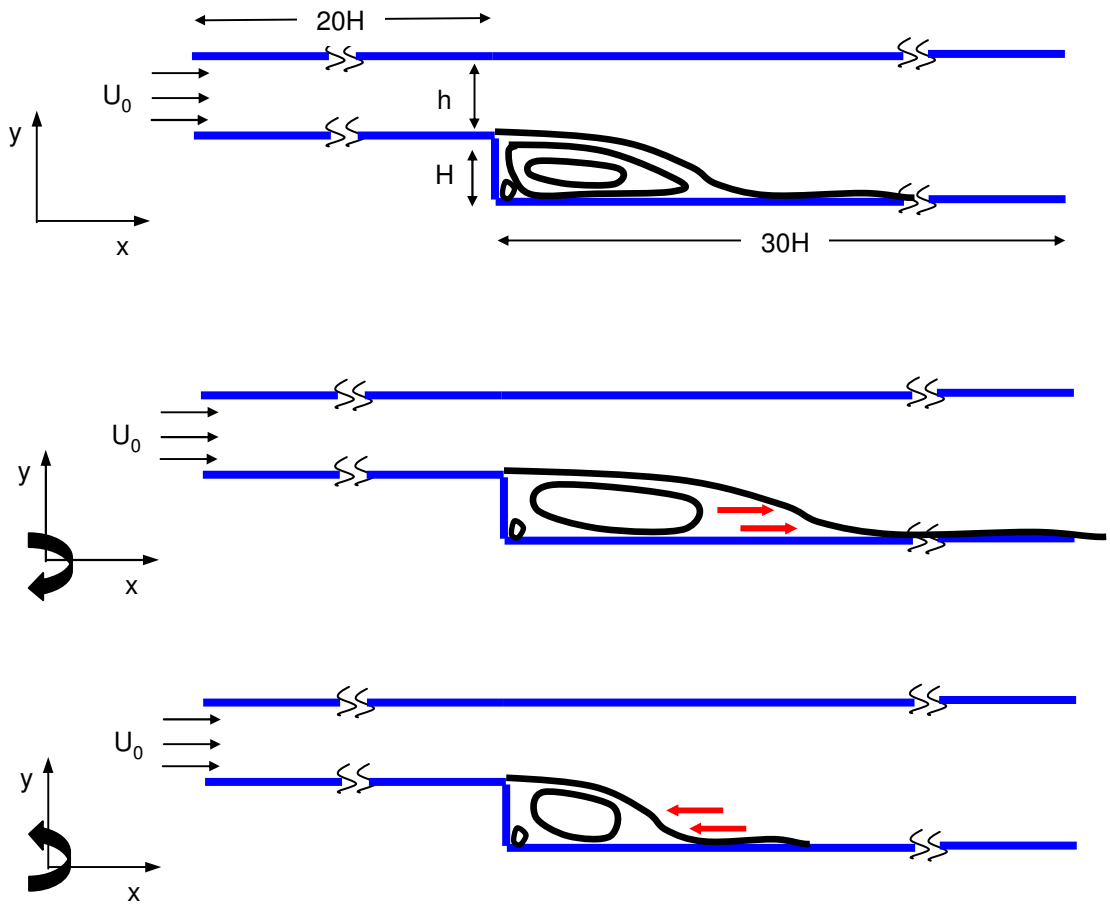

Figure 2: Geometry used for computation of flow downstream of a back-facing step. The effect of clockwise (negative) rotation and anti-clockwise (positive) rotation are also shown. Red arrows show the effect of Coriolis forces on the reattachment.

In spite of the continual development of RANS models, studies show that RANS models fall short in predicting the effects of rotation in turbulent flows. This study applies Detached Eddy Simulations (DES) to the unsteady flow downstream of a back-facing step and aims at capturing the three-dimensional, unsteady characteristics of the flow

downstream of the backward facing step and the effects of rotation on the reattachment length. The results obtained from these computations are compared with experimental measurements by Rothe and Johnston (1979). This study is used as a validation for applying DES to capture the effects of rotation.

4.1.1 Computational Details

The turbulent flow over a backward step of expansion ratio 2 is studied with the step height, H, equal to the height of the channel, h, upstream of the back-facing step. A uniform inlet velocity of U_0 (= 1), is prescribed at the inlet of the channel. The inlet is placed $20H$ upstream of the step so as to allow the flow to be fully developed before it enters the sudden expansion region. The expanded portion of the duct extends up to $30H$ downstream of the step to eliminate any disturbances from the exit conditions prescribed. The global Reynolds number ($Re = U_0H/\nu$) based on the inlet velocity and the step height is 10000 and the global rotation number ($Ro = \Omega H/U_0$) is varied from -0.08 (clockwise rotation) to +0.08 (anti-clockwise rotation). The width, W, of the duct upstream of the step is varied and two different widths – $W = 5H$ and $2H$ are considered in the current computation. The geometry used and the anticipated effect of rotation are shown in Figure 2.

Figure 3 shows the grid distribution in the x, y, z directions for the baseline grid with 72 points in the streamwise direction, 24 points along the height of the channel and 32 points in the spanwise direction. The *a-posteriori* evaluation of the wall normal grid spacing (for the stationary duct of aspect ratio of 2) shows that the $\Delta^+ < 1$ in the region downstream of the backward facing step. The streamwise grid distribution gives $\Delta^+ \sim 1$ near the backward facing step wall, which gradually increases to a value of $\Delta^+_{max} \sim 1000$

near the outlet. The spanwise distribution yields $\Delta^+ \sim 1$ near the walls and $\Delta^+_{max} \sim 75 - 80$ towards the center of the duct.

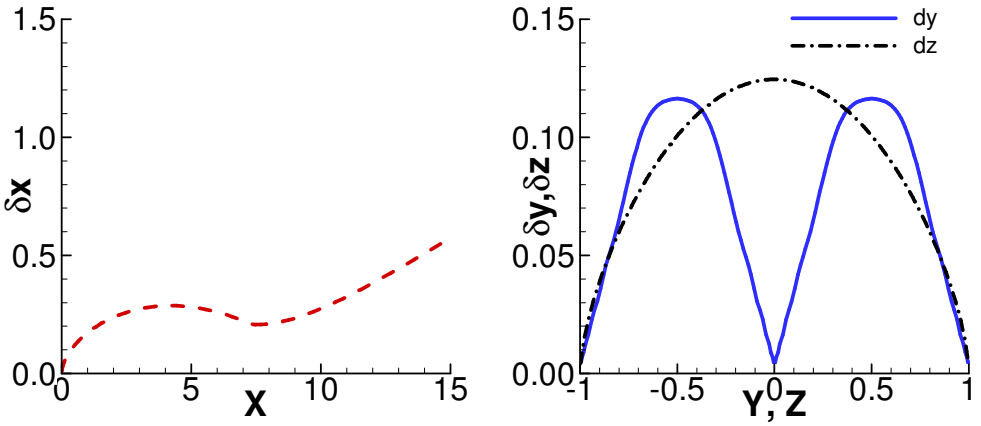

Figure 3: Grid distribution in the *x, y, z* directions downstream of the back-facing step, for the aspect ratio 2 channel.

The duct is subjected to orthogonal rotation with axis along the positive z-direction at an angular velocity Ω. The governing flow and energy equations are non-dimensionalized by a characteristic length scale which is chosen to be the step height (H) and a characteristic velocity scale given by the inlet velocity (U_0).

4.1.2 Grid Sensitivity

DES, like LES, is sensitive to the grid resolution. Refining the grid in the regions of interest, allows the model to resolve more turbulence. In the fine grid limit a DES computation becomes a LES computation. Three grids - 50 x 24 x 32 (coarse grid), 72 x 24 x 32 (baseline grid) and 100 x 24 x 32 (dense grid), are used to discretize the computational domain downstream of the step. A comparison of the reattachment lengths predicted downstream of the step shows that the baseline and the fine grid predict reattachment at a distance of 7.2H downstream of the step. On the other hand the coarse

grid predicts a value close to 5.5*H*. Rothe and Johnston (1979) experimentally showed that the reattachment point for this case to lie at a distance of 6.5*H*. The baseline and the fine grid predict reattachment lengths which are within 10% of the experimental measurements. However the baseline grid was considered for further computations, keeping in mind the cost of computation.

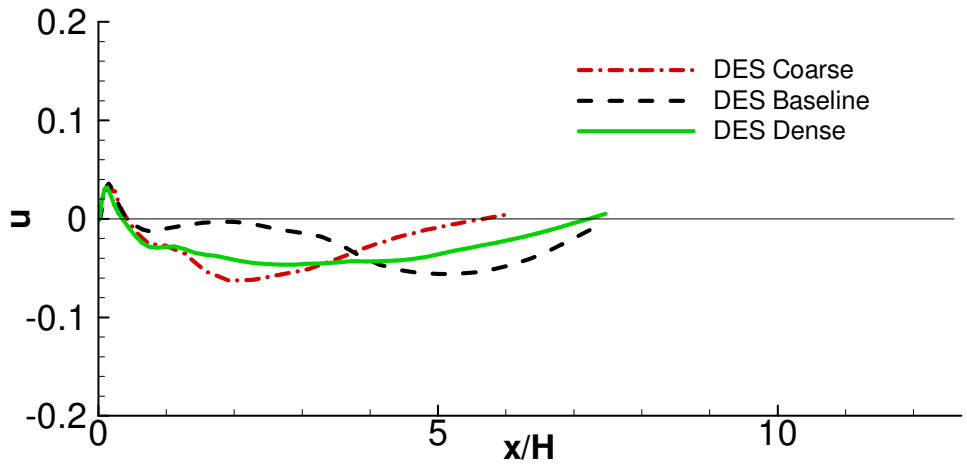

Figure 4: Comparison of the reattachment lengths for the three grids used for DES Computation

4.1.3 Comparison of Turbulence Strategies

Computations carried out for ducts with aspect ratio (AR = *W/H*) of 5 and 2 are compared with the experimental measurements by Rothe and Johnston (1979). Rotation introduces Coriolis forces and stabilizes or destabilizes the flow downstream of the backward facing step. While the Coriolis forces are accounted for in the main momentum equations, the attenuation/augmentation of turbulence has to be computed accurately for predicting the reattachment length.

The basic objective of DES is to predict results comparable in accuracy to LES but at a relatively lower cost. So it is important to verify that the grid used for DES is not sufficient for a LES computation. Comparisons of the reattachment lengths predicted by the Dynamic Smagaronsky LES, *k-ω* DES and *k-ω* URANS are compared with the experimental results reported by Rothe and Johnston (1979). From Figure 5 it is observed that LES predicts a reattachment length of 5.25, DES a value of 7.20 and URANS a value of 10.00. The experiments showed that the flow reattached at a distance of 6.50 step heights downstream of the step, which is in closest agreement with the value predicted by DES. This shows that LES would require a much finer grid to accurately resolve the turbulence and thereby accurately predict the reattachment. As an example earlier LES computations by Ghosal *et al.,* (1995) in expansion channels used a Δx^+_{max} = 273 and a uniform Δz^+ = 36, which is finer than the grid resolution used for the current computation. On the other hand URANS under-predicts the turbulence as a result of which the reattachment length is over-predicted.

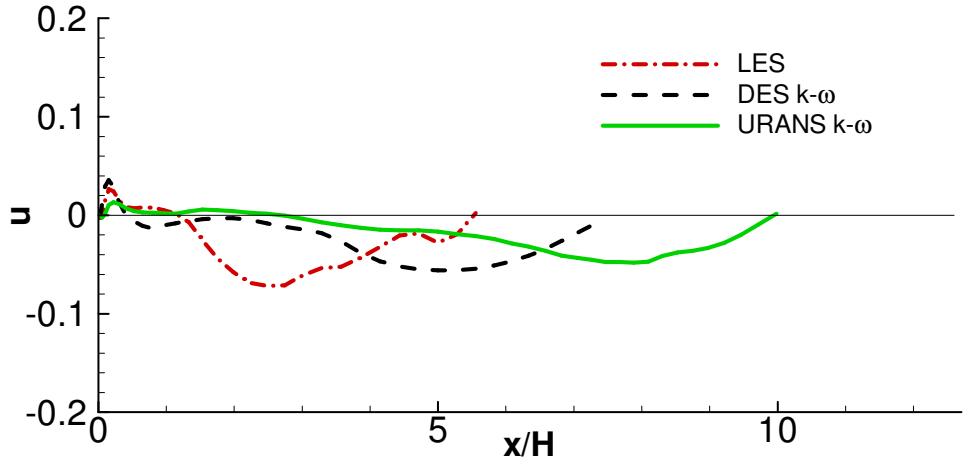

Figure 5: Comparison of the reattachment lengths downstream of the back-facing step for a stationary case (Ro = 0.00, Aspect ratio = 2). LES = 5.25, DES = 7.20, URANS = 10.00

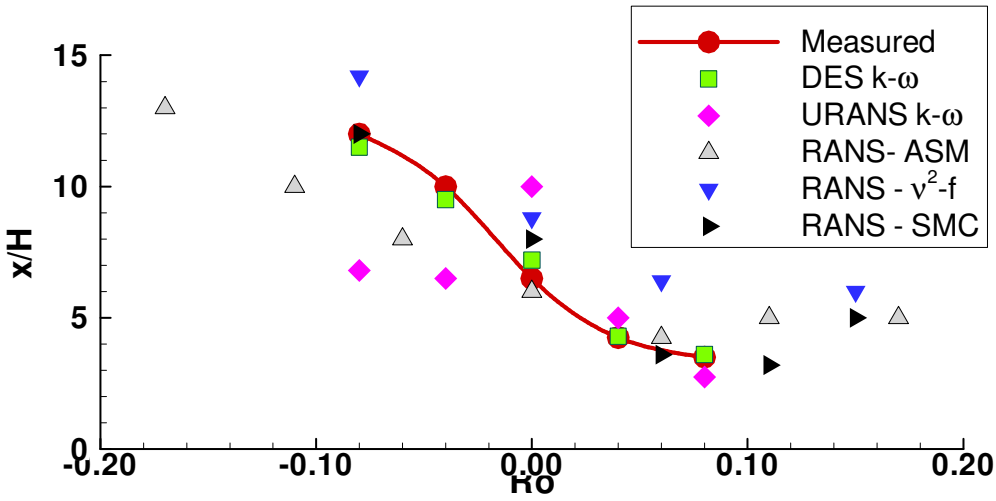

Figure 6: Comparison of the reattachment lengths as predicted by DES *k-ω* (Duct AR = 2), URANS *k-ω* (AR = 2) and earlier studies by Nilsen and Andersson (1990) (Re = 5500, AR = 2) and Iaccarino *et al.,* (1999) with experimental measurements by Rothe and Johnston (1979).

In order to establish the superiority of the DES results in comparison to RANS, computations were carried out on the same grid for all the rotation cases and compared with the experimental measurements. Figure 6 shows the comparison of the reattachment values predicted by *k-ω* URANS and DES as compared with the experiments. Results from earlier numerical studies using algebraic second moment (ASM) RANS model (Nilsen and Andersson) for the duct of aspect ratio 2 and RANS second moment closure (SMC) and v^2-*f* RANS models (Iaccarino *et al.,* 1999) are also presented along with the current results. It is observed that the ASM RANS model over-predicts the reattachment lengths for destabilizing rotation and under-predicts the length for stabilizing rotation. While the v^2-*f* RANS model over-predicts the reattachment lengths for all the rotation cases considered, the SMC RANS model shows mixed trends like the ASM RANS model. A comparison of the *k-ω* URANS studied in this computation shows that *k-ω* URANS underpredicts the reattachment length for almost all the rotation cases studied,

while overpredicting the reattachment length for the stationary flow. It is observed that DES overcomes the shortcomings of all the RANS models, predicting reattachment lengths with an accuracy of 13% of the experimental measurements.

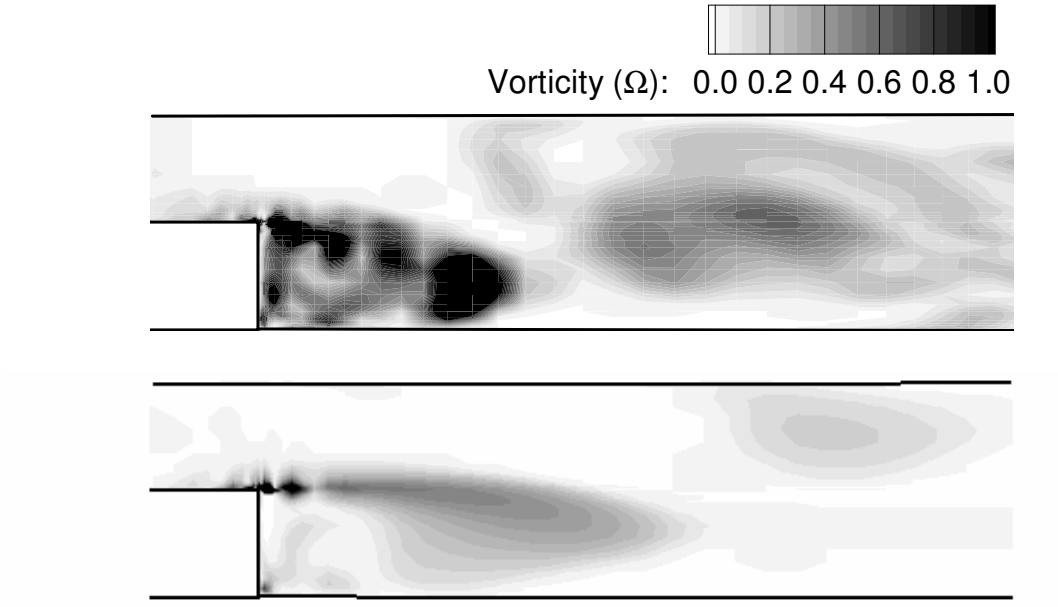

Figure 7: Instantaneous coherent vorticity contours downstream of the back-facing step (AR = 2), at the center of the duct for DES (Top) and URANS (Bottom).

To accentuate the capability of DES in capturing unsteady structures better than the URANS model on which it is based on, the instantaneous coherent vorticity contours (Chong *et al.,* 1990) are compared in Figure 7**.** DES predicts unsteady vortex shedding downstream of the backward facing step. The length scales associated with these structures are also observed to be much finer and the vorticity magnitudes much higher than the corresponding URANS predictions.

4.1.4 DES Regions

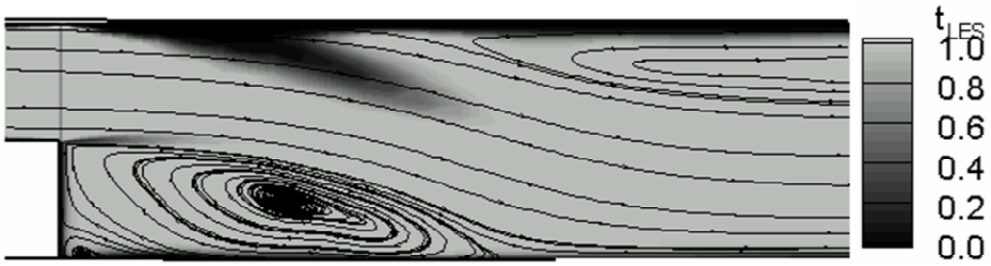

Figure 8: DES regions downstream of the back-facing step showing the dominance of LES characteristics in the region of separation (Case shown is Ro = 0.04).

Figure 8 shows the fraction of time (during the whole computation) when the calculation is solved in the LES mode. DES with k-ω model uses a turbulent length scale which is computed from the turbulence equations solved (k and ω). So the turbulent (RANS) length scale is a function of time as well as space. This feature facilitates the computation to be cognizant of the eddy length scales and hence behave as RANS or LES depending on the instantaneous local conditions, unlike in the case of a Spalart-Allmaras based DES, where DES acts just like a wall model. Another prominent feature of the DES version of the k-ω model is that although an instantaneous discontinuity may exist between the RANS region and the LES region, in the mean however a smooth transition takes place from RANS to LES and vice versa. In a DES Spalart–Allmaras model, the distance from the wall determines the switch from RANS to LES, is not receptive to instantaneous flow features.

The grid facilitates the computation of the region in RANS and/or LES depending on the instantaneous conditions existing in the region. The near wall region is always resolved in the RANS mode which transitions to the LES mode as the distance from the wall increases. The flow in the separation bubble downstream of the step and the recirculation zone on the top wall is mostly resolved in LES mode all the way to the

reattachment point. This feature ensures that the unsteady physics in the separated region is captured accurately both in the stationary as well as the rotating cases, without explicitly defining extra strain terms to account for rotation, in the turbulence equations.

4.1.5 Flow Characteristics

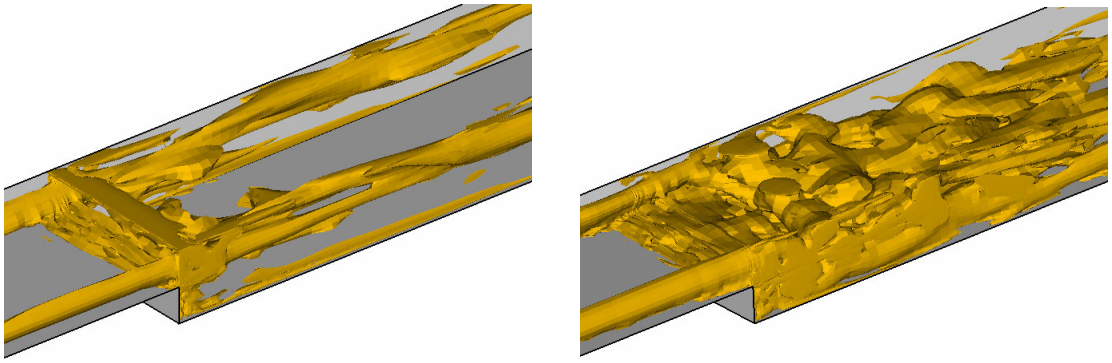

Ro = -0.08 **Ro = 0.08**

Figure 9: Iso-surfaces of coherent vorticity (Vorticity magnitude = 0.25) to show the stabilizing (Ro = -0.08) and the destabilizing effects (Ro = 0.08) of rotation on the flow downstream of the backfacing step. (Aspect Ratio = 5)

The tendency of rotation to stabilize and destabilize the flow downstream of the backward facing step can be estimated from instantaneous shots of the vortex structures. Visualizations of the instantaneous iso-surfaces of coherent vorticity (Chong *et al.,* 1990) for Ro = -0.08 and Ro = 0.08 as predicted by DES are presented in Figure 9. The iso-surfaces of the coherent vorticity show that while the flows with destabilizing rotation of Ro = 0.08 are highly three-dimensional, the flow in the Ro = -0.08 case is more stabilized. These features concur with the observations of Rothe and Johnston (1979).

Figure 10 shows the streamwise velocities at the first grid point from the bottom wall of the duct to study the reattachment lengths downstream of the backward facing step. It is observed that for the stationary case, the flow separates and reattaches at around 7.20

times the step height. This value predicted by DES compares well with the experimental value of 6.50. As the duct is rotated in the clockwise direction (negative rotation) the Coriolis forces acting on the flow, forces the flow to stay separated longer than in the stationary case, thereby resulting in larger separated zones. The turbulence in the separated zones is attenuated as rotation increases which further delays the reattachment. It is observed (for the duct aspect ratio of 2) that the reattachment length increases to a value of around 9.50 for Ro = -0.04 and further to 11.50 for Ro = -0.08.

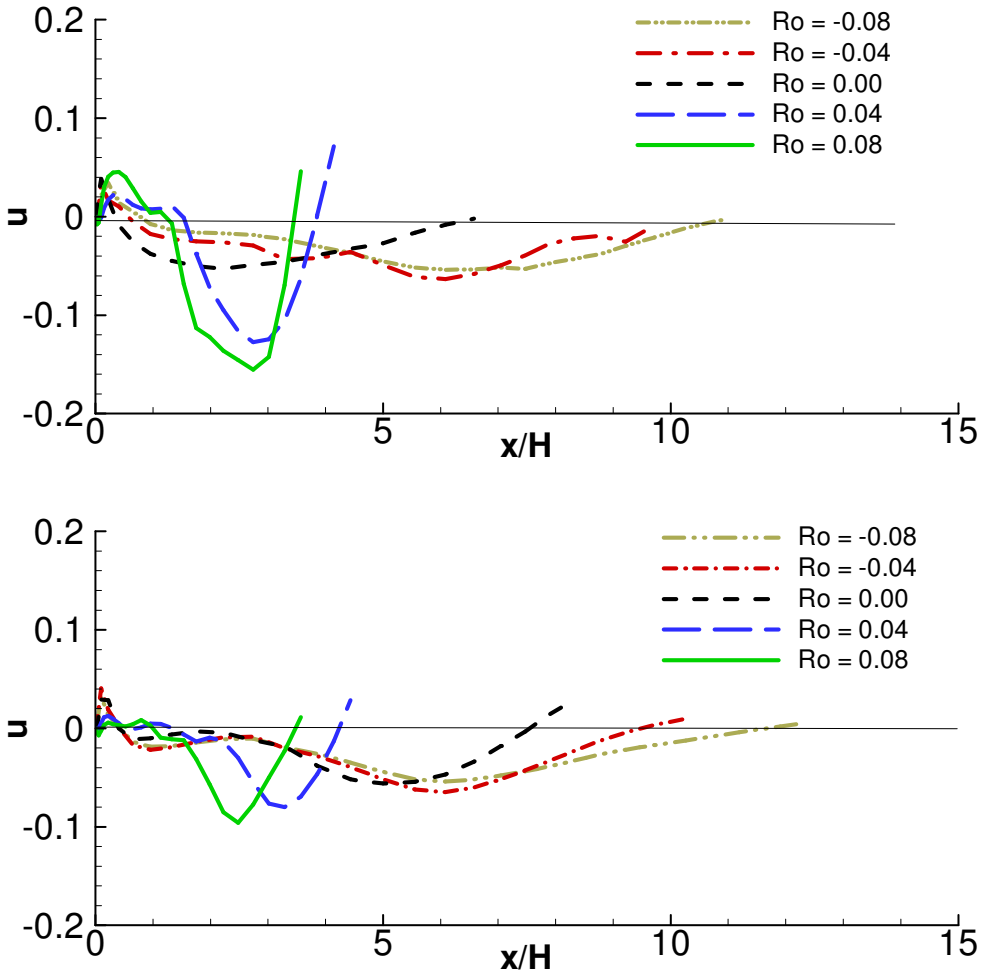

Figure 10: Variation of the reattachment lengths at the center of the channel with rotation number for the duct of aspect ratio 5 (Top) and 2 (Bottom)

On the other hand, the reattachment length for anti-clockwise (positive) rotation decreases as the Coriolis forces act to force earlier reattachment. The turbulence in the separated region is augmented thereby aiding reattachment. It is observed that the reattachment length decreases to a value of 4.30 for Ro = 0.04 and further to 3.60 for Ro = 0.08. As the system is rotated in the anti-clockwise direction, flow separates at the top wall (around 2.0 step heights) downstream of the step and reattaches around 14.0 step heights downstream. Similar features are observed for the duct with an aspect ratio of 5 as shown in Figure 10.

Figure 11 shows the comparison of the reattachment lengths predicted by DES for channels of aspect ratio 5 and 2. The reattachment length downstream of the rotating back-facing step is a function of the Reynolds number, the aspect ratio of the channel, the inlet conditions and the system rotation. In the cases considered, since the inlet conditions and the Reynolds number are maintained constant the channel aspect ratio and the rotation affect the reattachment length.

For a duct aspect ratio of 5, it is observed that the reattachment length increases from a value of around 3.70 for the highest rotation in the anti-clockwise direction to a value of around 10.90 for the highest rotation in the clockwise direction. For the duct with aspect ratio of 2, the reattachment length increases from a value of around 3.60 to a value of 11.50 for the highest rotation in the clockwise direction. The values predicted by DES compare well with the experimental observations prediction values within 13% of the measurements.

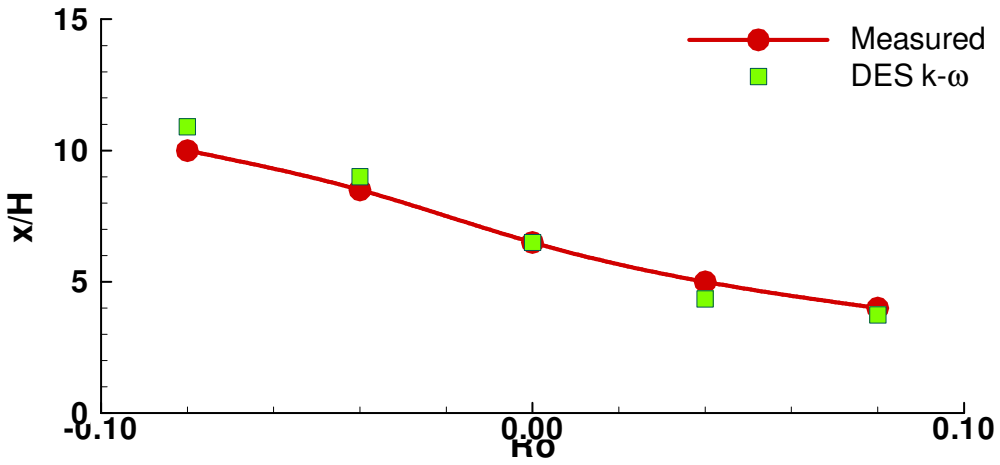

(a)

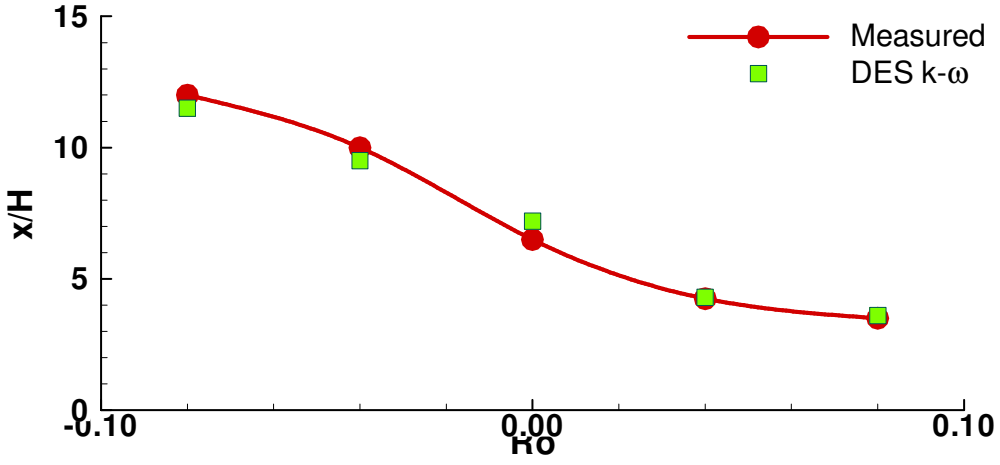

(b)

Figure 11: Comparison of the reattachment lengths for a duct of (a) AR = 5 (b) AR = 2

A comparison of the reattachment lengths for the two ducts shows that the separation bubbles are larger for the smaller aspect ratio duct. In the duct with an aspect ratio of 2, the side walls suppress the vortices in the spanwise direction, resulting in lower levels of turbulence in the separation bubble, which delays the reattachment of flow.

Figure 12 shows the instantaneous coherent vorticity iso-surfaces (Chong *et al.,* 1990) downstream of the backward facing step. It is observed that the flow in the duct of larger aspect ratio is characterized by unsteady, three dimensional flow. However the vortices in

the duct of smaller aspect ratio clearly show the influence of the side walls which result in the damping of these three dimensional structures.

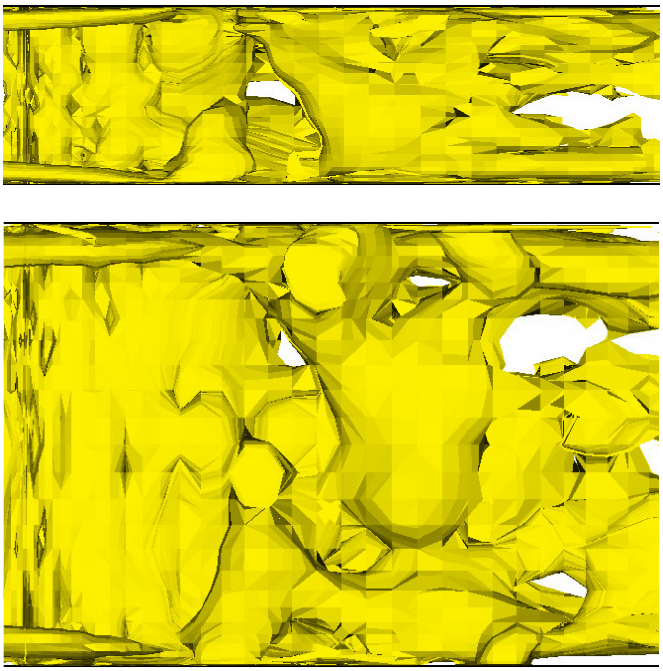

Figure 12: Top view of the instantaneous coherent vortices (vorticity magnitude = 0.25) downstream of a backward facing step for ducts of aspect ratio 2 (Top) and aspect ratio 5 (bottom)

4.1.6 Conclusions

Computations are carried out for the rotating flow in a back-facing step. DES is used to compute the turbulent flow in the duct. Since the flow Reynolds number was maintained constant, it was observed that the rotation rate and the aspect ratio of the duct influence the turbulence downstream of the duct. The Coriolis forces and the turbulence in the separation zone affect the reattachment point.

Computations were carried out for two different aspect ratio channels for 5 different rotations ranging from Ro = -0.08 to Ro = 0.08. The reattachment point predicted by DES

showed favorable agreement with the experimental observations, for all the cases studied, predicting the lengths within accuracy of 13%.

The prediction of the three-dimensionality and time dependence of the rotation dominated, separated flow downstream of the backward facing step undergoing rotation is observed to be superior to what can be achieved using RANS models. It is also concluded that using eddy-viscosity models in the DES mode overcomes some of the inherent shortcomings of the base RANS model. The unsteady physics and the trends in the flow field as observed in experiments are captured accurately by DES without the need for defining extra strain terms for rotation in the turbulence equations.

4.2 Prediction of the Turbulent Cavity Flow driven by Shear and Buoyancy using Detached Eddy Simulations

Numerical predictions are reported for the turbulent flow in a cavity driven by the shear provided by a channel flow and buoyancy due to the heated top wall. Buoyancy affects the flow and temperature fields in the cavity. As the buoyancy effects increase the tendency of warmer fluid to remain near the top heated wall increases. It is observed that DES captures the effects of shear and buoyancy and the temperature and flow fields predicted match accurately with the experiments. This study is used as a validation for applying DES to flows driven by shear and buoyancy.

The main objective of the current study is to capture the mixed convection effects that buoyancy introduces in flows driven by shear. In spite of the continual development of RANS models, studies show that eddy-viscosity based RANS models are not adequate for predicting the effects of buoyancy. Our main objective is to show that eddy viscosity

RANS model when used in the DES mode are able to capture the effects of buoyancy without the use of additional adjustments to the base RANS model. In addition it is shown that DES predicts accurate results at a computational cost much lower than LES.

4.2.1 Computational Details

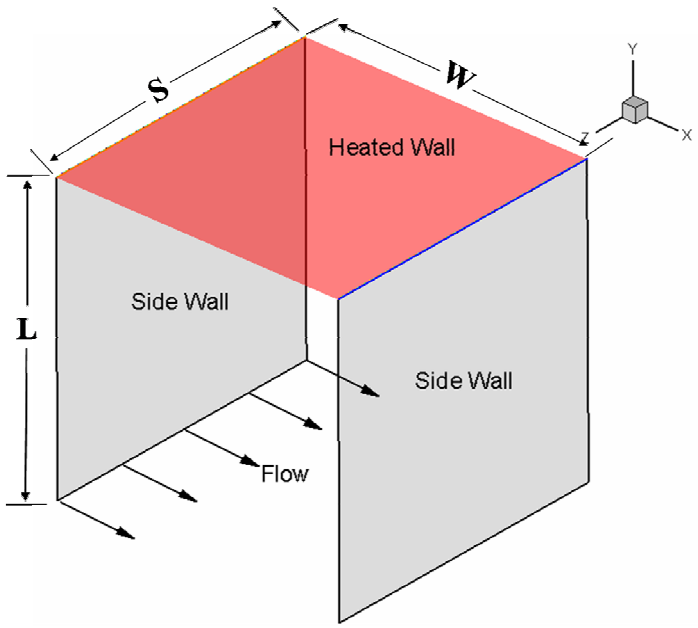

Figure 13: Schematic diagram of the 2D cavity studied. Periodic boundary conditions are used in the z direction

The turbulent flow in an open cavity is studied. The cavity height, L, is equal to the width, W. Flow at a velocity of U_0 (= 1) and a temperature of T_0, is prescribed at the bottom wall of the cavity to mimic the flow driven by a thin outer channel. The top wall is heated at a constant temperature ($T_H = T_0 + \Delta T$) while the side walls are insulated. The global Reynolds number (Re = $U_0 L/\nu$) based on the velocity at the bottom wall and the cavity height is 10000 and two different Archimedes numbers ($Ar = Gr/Re^2 = g\beta\Delta TL/U_0^2$, β is the thermal expansion co-efficient) are studied – 0.00 and 0.37 to evaluate the effect of buoyancy on the flow and temperature distribution in the cavity. A spanwise width, S,

was used and since the conditions are studied at a location where the flow was observed to be two-dimensional from the experiments by Grand (1975), periodic boundary conditions were imposed along the spanwise direction. The geometry used is shown in Figure 13.

The governing flow and energy equations are non-dimensionalized by a characteristic length scale which is chosen to be the cavity height (L), a characteristic velocity scale given by the velocity (U_0). An additional body force term ($Ar\theta\delta_{i2}$) is added to the momentum equation to model the effects of buoyancy. In the buoyancy term θ is the non-dimensional temperature defined as $(T-T_0)/\Delta T$ and Ar is the Archimedes number, which is defined as the ratio of the gravitational forces to the viscous forces. Turbulence is modeled using Wilcox's k-ω model (1988) in the DES formulation (Appendix A). The results obtained from these computations are compared with experimental measurements by Grand (1975). Figure 14 shows the locations at which the temperatures have been reported.

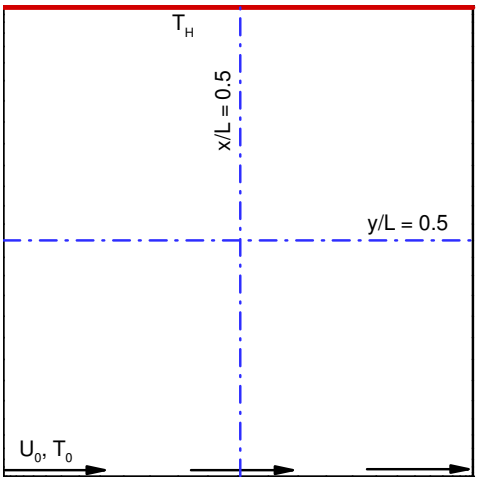

Figure 14: Schematic diagram showing the measurement planes where the temperature profiles have been reported

4.2.2 Effect of Grid Density

Ideriah (1980) used the *k-ε* model (with a modification to account for the buoyancy terms) to study the flow in a cavity that is driven by shear as well as buoyancy forces. The domain used to compute the flow was divided into 37 x 37 cells. In spite of the modification used to account for the effects of buoyancy the model failed to capture the flow physics accurately for the high buoyancy case studied. Chow and Gao (2004) carried out detailed LES computations on a 100 x 100 and a 37 x 37 grid to study the effect of the Smagorinsky constant and the grid sizes on the flow in the cavity. While the predictions obtained from the fine grid were observed to be in good agreement with the experiments, the coarser grid failed to predict the trends of the temperature and the flow fields. Keeping the grid sizes of these two computations in mind it was decided to test similar grid densities for the DES computations.

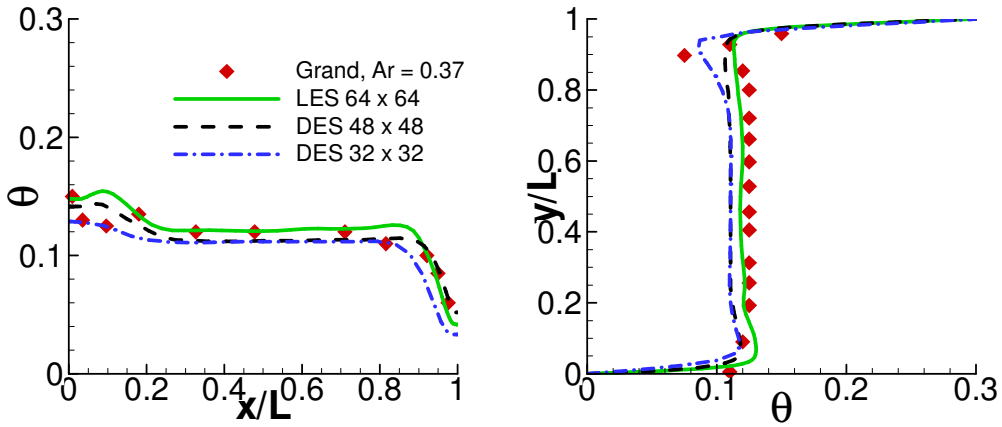

Figure 15: Grid independency study comparing the spatial variation of temperature predicted by DES and LES with experimental data. Data has been extracted at the vertical center (*y/L* = 0.5) and horizontal center (*x/L* = 0.5) of the cavity

Figure 15 compares the temperature field obtained from a LES computation carried out on a 64 x 64 x 64 grid and DES on two grids – 48 x 48 x 48 and 32 x 32 x 32. The

basic objective of this comparison is to show the efficiency of DES in predicting results with an accuracy as good as LES but at grids of much coarser resolution. While it is observed that the values predicted by the LES computations compare well with the experimental values, DES predicts the same trends on a grid that is almost 8 times coarser than the LES grid used. Since no major differences are observed in the prediction capabilities of the two DES grids, the coarser (32 x 32 x 32) grid is used for further analysis.

4.2.3 Effect of additional buoyancy terms

Earlier computations using (U)RANS (Hanjalic *et al*., 1996, Rodi *et al.,* 1983, Peng and Davidson, 1999, Stips *et al.,* 2003) have shown the necessity to incorporate extra strain terms to model the effects of buoyancy. These extra strain terms are tailored for each specific case and hence different forms of the buoyancy production terms are used in the turbulence equations for different applications. On the other hand LES does not explicitly require any terms to model these non-linear effects.

In order to check the effect of the additional terms in DES, two models – one with the additional buoyancy production term in the *k*-equation (Appendix A) and another without the term (Chapter 3.3) were tested. A comparison of the temperature profiles predicted by the models is shown in Figure 16. URANS shows a definite improvement in the results as the extra buoyancy term is added. DES on the other hand does not show any difference due to the addition of the extra production term. Both the forms of DES are equally effective in capturing the variation in the temperature. Hence the rest of the study was

carried out using DES derived from the 1988 k-ω model, without the additional buoyancy term.

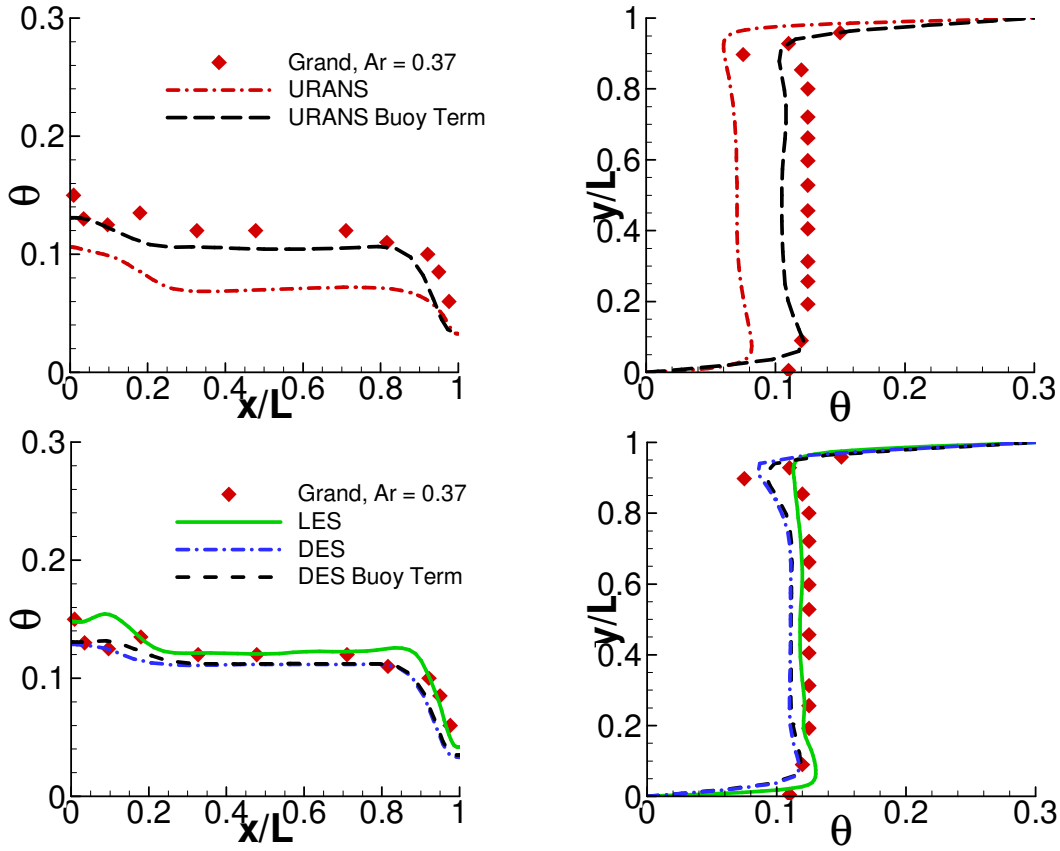

Figure 16: Effect of the buoyancy term in the URANS (Top) and DES (Bottom) calculation. Data has been extracted at the vertical center (y/L = 0.5) and horizontal center (x/L = 0.5) of the cavity

4.2.4 Effects of buoyancy

Figure 17 shows the effect of buoyancy on the temperature distribution in the cavity. Computations carried out for a Reynolds number of 10,000 and for two buoyancy cases – Ar = 0.00 and 0.37 are compared with the experimental measurements of Grand (1975). Increasing the buoyancy, results in the warmer fluid to remain near the top wall. This results in a larger region of stable stratification as can be observed in the θ vs. y/L plots in the regions $y/L > 0.90$.

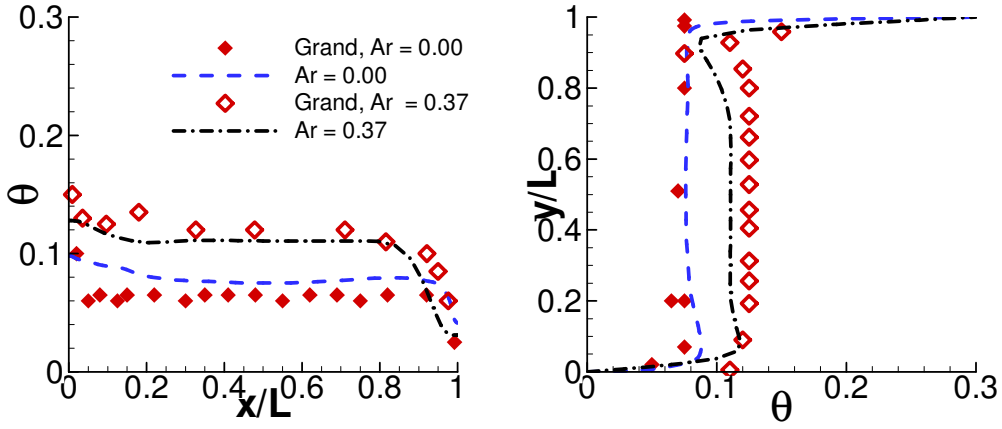

Figure 17: Effect of buoyancy in influencing the temperature in the cavity at *y/L* = 0.5 and at *x/L* = 0.5

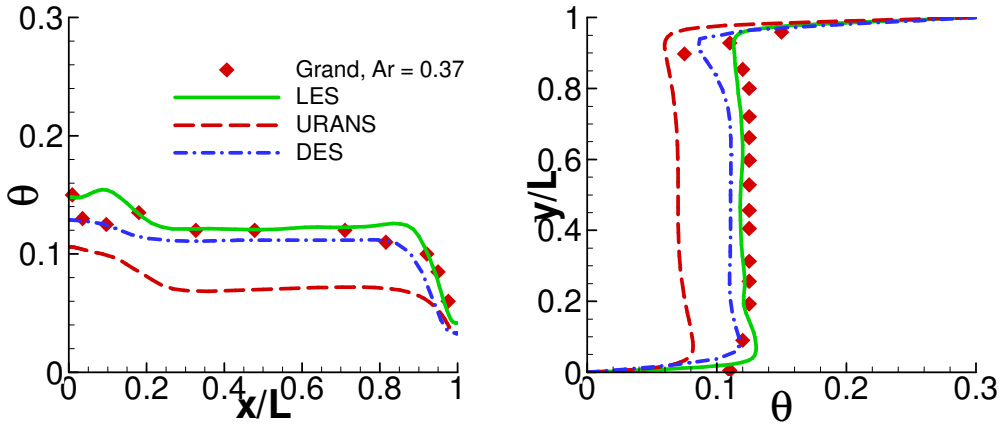

Figure 18: Comparison of the spatial variation of temperature (LES on 64 x 64 x 64 grid, DES and URANS on 32 x 32 x 32 grid) with experiments by Grand (1975), for a high buoyancy case.

Figure 17 shows the comparison of the temperature profiles measured at the vertical and horizontal centers of the cavity. The temperature profiles show good agreement with the experiments. This shows the capability of DES to accurately capture the effects of shear and buoyancy that drives the cavity flow. Figure 18 shows the comparison of the LES, DES and URANS predictions with the experimental values. It is observed that while LES (64 x 64 x 64 grid) and DES (32 x 32 x 32 grid) predicted the temperature variation reasonably well, the URANS (32 x 32 x 32 grid), like in earlier studies (Ideriah,

1980) fails to predict the trends accurately. Since DES treats a major portion of the flow in LES mode, the effects induced due to buoyancy are captured by the grid length scales. This allows DES to accurately predict the effects of buoyancy in the cavity flow case.

4.2.5 Conclusions

From the computations carried out above it has been shown that DES can be successfully applied to study the effects of shear and buoyancy. The important conclusions obtained from this study are:

1. The effect of shear and buoyancy can be predicted accurately using DES at a cost much lower than that required for an LES computation.
2. DES does not require any *ad hoc* terms to account for the effects of buoyancy.
3. While URANS fails to predict the temperature distribution accurately as the buoyancy is increased, the equivalent DES formulation captures these effects.

5 Flow and Heat Transfer in the Fully Developed Ribbed Duct

Fully developed flow in a duct is achieved after a certain distance from the inlet, when the flow and thermal solution of the flow is repetitive in the streamwise direction. Earlier studies (Rau *et al.,* 1998, Sewall and Tafti, 2004, Sewall *et al.,* 2006a) show that after a few ribs (3^{rd} - 4^{th} in the stationary duct and 8^{th} – 9^{th} in the rotating ducts) the flow and thermal solution is repetitive and so it is a good assumption to consider the flow to be fully developed downstream. In order to study the flow features in the fully developed region of the duct, periodic boundary conditions can be used in the streamwise direction. Applying periodic boundary condition is a means by which the computation domain is replicated through space to form a straight ribbed duct of infinite length. In the simulation, as a fluid particle leaves the computational domain, it is replaced with its periodic image that enters at the opposite side. By modeling the fully developed regime in this manner, the size of the computation domain used for solving the problem is reduced drastically in size. This facilitates easy numerical experimentation with grids and the model validation process is faster. This study presents computations in the hydrodynamically and thermally fully developed region of the ribbed duct. The validation of DES in canonical geometries discussed in the previous chapter is followed up in this study wherein the flow and heat transfer in a non-canonical, internal flow regime is studied. Through the comparison of the flow and thermal features with experiments and LES computations, the capabilities of DES in predicting flows in stationary and rotating ribbed ducts are validated.

The computational domain consists of a ribbed channel, with two ribs placed at the center of the channel, at the top and the bottom. The rib pitch to rib height of 10 and rib height to hydraulic diameter of 0.1 at a bulk Reynolds number of 20,000. The domain used for the study is shown in Figure 19.

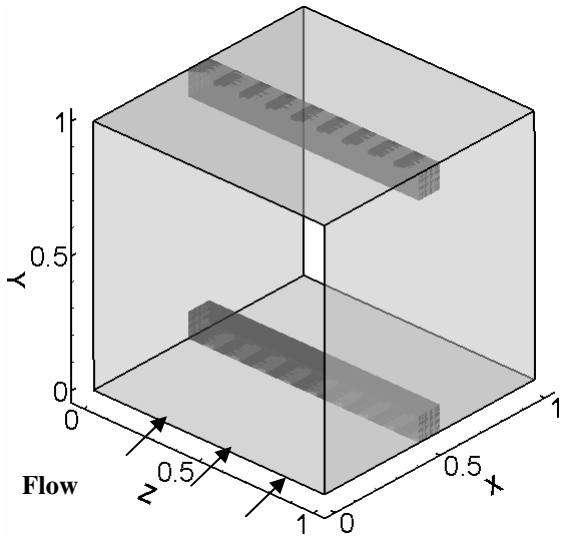

Figure 19 : The computational model - A pair of ribs placed at the center of the duct. Flow in the duct is periodic in the streamwise direction.

A no-slip boundary condition is imposed on the walls and the ribs. The conditions set at the wall are $\vec{u} = 0$, k = 0, and $\omega \to 6/\mathrm{Re}_\tau\, \beta_1 y^2$ as $y \to 0$, which is derived from a molecular diffusion and dissipation balance on smooth surfaces (Wilcox, 1988). The turbulent Prandtl number is assumed to have a constant value of 0.9. A periodic boundary condition is imposed in the streamwise *(x)* direction which gives the relation $\phi(x + L_x) = \phi(x)$, where Φ = $\bar{u}$, p, θ, k and ω. The mean pressure gradient β is assumed to be unity, whereas the temperature gradient γ is calculated from a global energy balance as $\gamma = q''\Omega \big/ \mathrm{Re}_\tau \,\mathrm{Pr}\, Q_x L_x$.

In the study, the flow and heat transfer in both stationary and rotating ducts is investigated. The first section of the study deals with the detailed flow and heat transfer validation in a stationary duct. This study is further extended in the subsequent sections to study the effects of rotation. Initial computations are carried out by considering the effects of Coriolis forces and neglecting the effects of centrifugal buoyancy to evaluate the performance of DES in predicting the effects of Coriolis forces. Once these effects have been successfully captured, the capability of DES in predicting the effects of centrifugal buoyancy is validated.

5.1 Grid Sensitivity Comparisons

DES is sensitive to grid resolution as shown by earlier DES calculations (Forsythe *et al.,* 2002). The grid dependency is not similar to LES, where an increase in resolution of the grid improves the solution. In DES, a grid which is fine might trigger an LES solution in the boundary layer, which might be detrimental if the resolution is not fine enough for LES. On the other hand, a coarse grid may eliminate the LES regions in the grid altogether, and in the limit the calculation would default to a URANS calculation. So a grid sensitivity study is carried out for the fully developed region of the stationary ribbed duct.

Table 4: *a-posteriori* comparison of the grid dimensions in the three directions for the DES grids

Grid	Δy^+	Δx^+	Δz^+
48^3 grid	0.2 - 3.25	1 – 200	1 – 250
64^3 grid	0.2 - 2.89	1 – 90	1 – 120
96^3 grid	0.2 - 2.95	1 – 36	1 – 80

A 96^3 grid used for earlier LES studies (Tafti, 2005) was considered as the fine grid used in the study. A baseline grid (64^3) was formed by maintaining the same grid resolution near the walls and coarsening the grid in the inter-rib spacing and in regions away from the channel walls. The coarsest grid (48^3 cells), was obtained by coarsening the 64^3 grid in regions away from the walls. Henceforth, the 96^3, 64^3 and the 48^3 grids are referred as fine grid, baseline grid, and the coarse grid, respectively. In the three resolutions tested, the near wall grid resolution was maintained and only the regions away from the wall were modified to generate coarser meshes. A *a-posteriori* grid evaluation of the three grids is shown in Table 4.

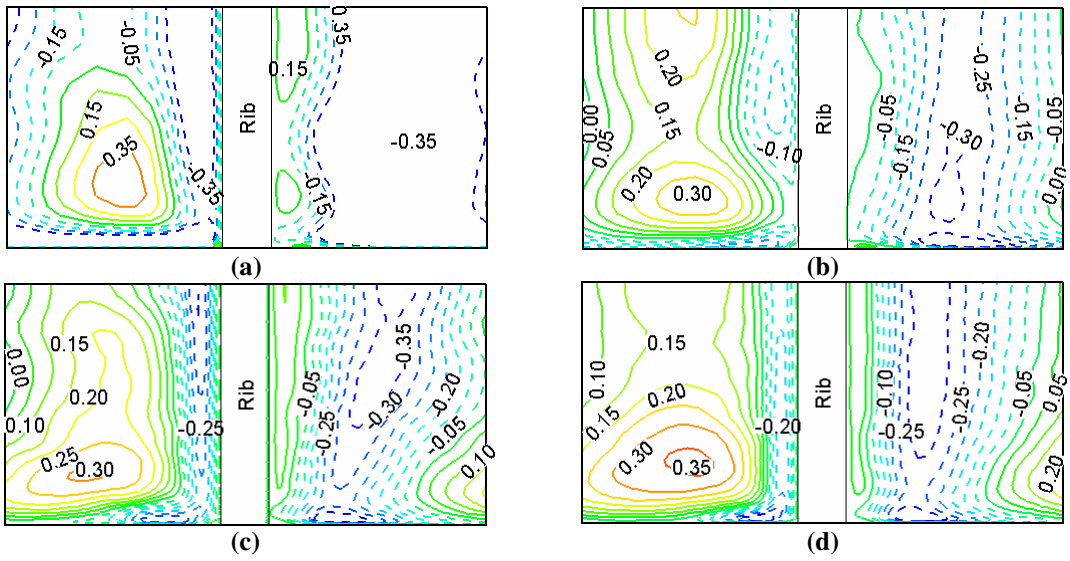

Figure 20 : Comparison of the streamwise velocities in a plane through the ribs (*y/e* = 0.25) for the (a) 48^3 grid (b) 64^3 grid (c) 96^3 grid (d) LES 128^3 case. 64^3 and the 96^3 case show the best agreement. 48^3 grid overpredits the extent of the recirculation region.

A non-dimensional time step of 5 x 10^{-5} was used in all the cases. Calculations are initiated by assuming an initial bulk velocity and integrating in time until a balance

between the internal losses and the specified pressure gradient was obtained. Although the whole domain is considered for the calculation, owing to the symmetry along the y and z directions, the average solution for a quadrant is presented.

DES computations were carried out on the three grids and a comparison of the average streamwise velocities (Figure 20) shows that while the baseline grid and the dense grid compare well with the LES results, the coarse grid fails to accurately predict the velocity levels. A comparison of the baseline grid and the denser grid shows that both grids predict the streamwise velocity contours to good accuracy (Figure 20) and capture the secondary recirculation behind the rib. The denser grid did not show any added value, and so the baseline grid was considered to be sufficiently accurate for further study. Hence, all computations have been carried out with the 64^3 (baseline) grid.

5.2 DES Regions

The underlying idea of DES is to compute regions closer to the wall using a RANS model and solve the regions of separation, or the region of detached eddies, in LES mode. Figure 21 shows the fraction of time (during the whole computation) when the calculation is solved in the LES mode. DES uses a turbulent length scale which is computed from the turbulence equations solved (k, ω). So the turbulent (RANS) length scale is a function of time as well as space. This feature facilitates the computation to be cognizant of the eddy length scales and hence behave as RANS or LES depending on the instantaneous local conditions, unlike in the case of a Spalart – Allmaras based DES, where DES acts just like a wall model. Another prominent feature of the DES version of the two equation model is that although an instantaneous discontinuity may exist between the RANS region and the LES region, in the mean however a smooth transition takes

place from RANS to LES and vice versa. It can be observed from Figure 21 that the RANS regions transition into LES smoothly. In a DES Spalart - Allmaras model, the distance from the wall determines the switch from RANS to LES, which is not as receptive to instantaneous flow features.

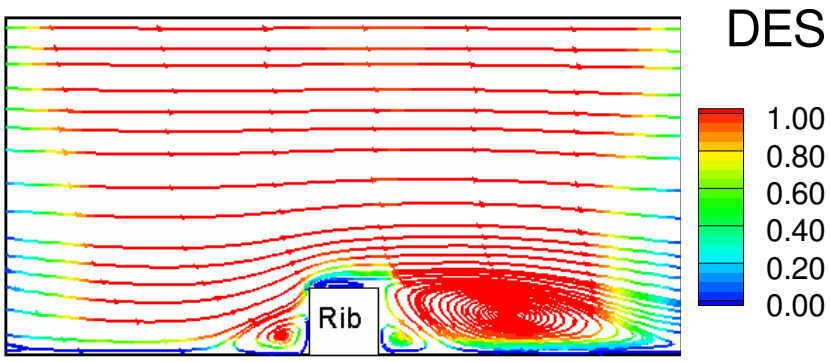

Figure 21 : Plot of the LES and RANS region in the DES computation for the 64^3 grid in a *Z* plane. A value of 1 represents a complete LES region and a value of 0 a complete RANS region. Flow is periodic in the streamwise direction.

The near wall region is always resolved in the RANS mode which transitions to the LES mode as the distance from the wall increases. The flow in the vicinity of the ribs is mostly resolved in LES mode all the way to the channel center. This includes the unsteady large-scale dynamics of the separated shear layer as shown in Figure 21. Though the inter-rib spacing is predominantly LES it transitions to a RANS mode at the center of inter-rib region. The grid facilitates the computation of the region in RANS and/or LES depending on the instantaneous conditions existing in the region. Downstream of the rib, in the region of separation it is observed that the computation is mostly carried out in the LES model. This sensitizes the RANS model to grid length scales, thereby allowing the natural instabilities of the flow in this region to develop. Thus the unsteady physics in the separated region is captured accurately.

5.3 Stationary Duct

5.3.1 Flow Field Predictions

The mean flow pattern observed in the symmetry plane of the span is shown in Figure 21. Flow patterns produced by the LES cases (Tafti, 2005), the RANS models (Ooi *et al*., 2002) and the experiments (Rau *et al*., 1998), show a similar pattern. The flow is characterized by a recirculating eddy in front of the rib, followed by shear layer separation on the rib and the presence of a recirculation region on top of the rib and behind it. Between the main recirculation region and the rib there is an additional counter-rotating eddy. The reattachment length is calculated as 4.6*e* (for *k-ω*) and 4.1*e* (for SST) from the rib, as compared to the LES predictions of 4.1*e* and experimentally observed value of 4.0*e* – 4.25*e*. The prediction of the reattachment length is sensitive to the level of turbulence in the separated shear layer, so the turbulence level may be under-predicted in the *k-ω* case, due to which the reattachment length is over-predicted.

Table 5 : Percentage form and friction drag in the ribbed duct

	LES 128^3	DES *k-ω*	DES SST	RANS *k-ω*
Form Drag	91.0	91.9	95.2	88.0
Ribbed Wall Friction Drag	-1.70	-1.80	-1.30	-1.40
Smooth Wall Friction Drag	7.80	4.50	3.20	11.80
Rib Friction	-0.80	-0.17	-0.49	0.30

A comparison of the total drag in the duct shows that the form drag contributes to a major part of the losses, as is evident from Table 5. The predicted values of form drag agree well with the form loss measured by Rau *et al.,* (1998) of around 85% and the LES

predictions of 91% by Tafti (2005). Owing to the recirculation, a negative friction loss is observed at the ribbed walls of the duct. A small recirculation region was observed above the rib by Rau *et al*. (1998). The DES calculations capture this recirculation while the *k-ω* RANS calculation shows a smooth flow above the rib. This is evident from the negative value of friction in the DES cases and a positive value in the RANS case (Table 5).

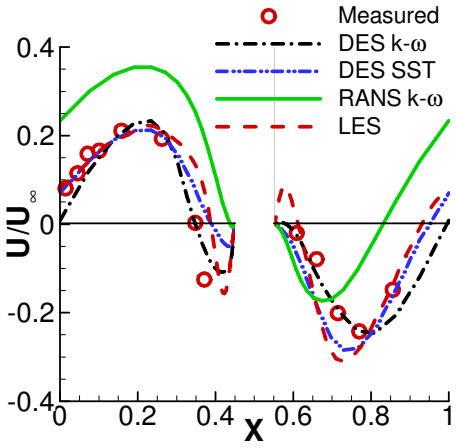

Figure 22 : Streamwise velocity distributions at the center of the duct at *y/e* = 0.1 in comparison with the experimental measurements by Rau *et al*., (1998)

A plot of the normalized streamwise velocities (Figure 22) at a plane close to the ribbed wall (*y/e* = 0.1) indicates the acceleration and deceleration of the flow in the inter-rib region. The separated region behind the rib experiences a reverse flow, which is evident from the negative velocities behind the rib up to the reattachment region. The flow accelerates after reattachment and separates in front of the next rib, owing to the rise in pressure. The separation in front and downstream of the rib are predicted by both DES calculations (*k-ω* and Menter's SST), and the velocity magnitudes are consistent with the LES calculations and the measurements. The *k-ω* RANS fails to predict the flow correctly in these regions.

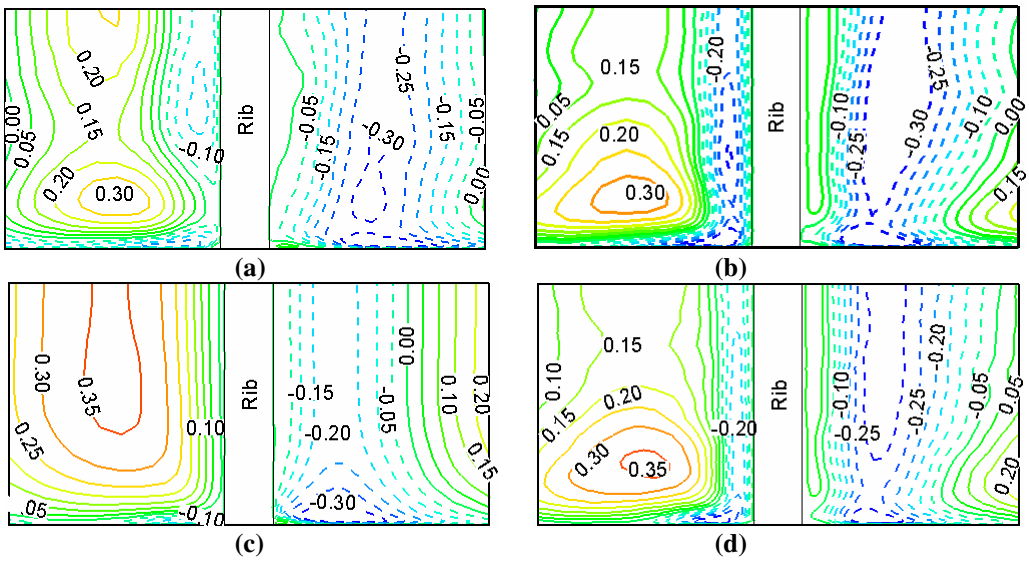

Figure 23 : Comparison of streamwise velocity distributions at *y/e* = 0.25 for the (a) *k-ω* DES case (b) SST DES case (c) *k-ω* RANS case (d) LES case

A contour plot (Figure 23) of the streamwise velocities in a plane passing through the rib (at y/e = 0.25) shows that the maximum velocities do not occur in the center of the channel but closer to the side wall. The flow separation behind the ribs causes this shift. While DES successfully reproduces the trend observed by the experiments, the *k-ω* RANS case fails to capture the variation. Similar results were reported by Ooi *et al*, (2002) for their RANS calculations. The DES distributions match well with the LES cases (Tafti, 2005). The *k-ω* DES case over-predicts the separation region due to which the zero velocity contour line is predicted further downstream as compared to LES and Menter's SST predictions.

Figure 24 shows the lateral w-velocities above the rib along a line close to the smooth side wall (y/e = 1.5, z/D_h = 0.45), as an indication of the strength of the localized secondary flow in the vicinity of the rib. The DES and the *k-ω* RANS calculations are

compared with the measured values and LES. While RANS completely fails at resolving this feature of the flow, DES does a good job at resolving the correct distribution.

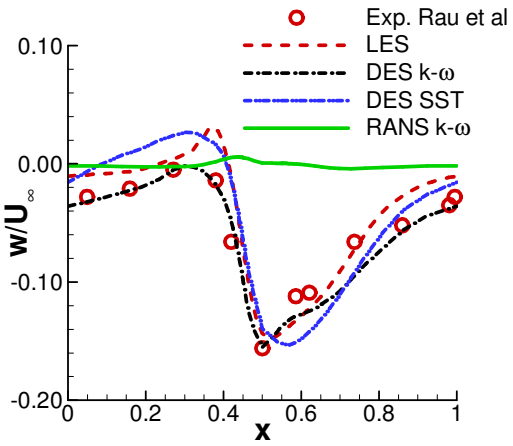

Figure 24 : Comparison of the secondary flow distribution at *y/e* = 1.5 and z/D_h = 0.45

Mean secondary flow patterns in the cross-section were studied experimentally by Liou *et al*. (1993) using LDV techniques. These secondary flow structures are strongest in the vicinity of the ribs and are generated by turbulence. The flow causes core fluid in the center of the duct to be drawn towards the side walls. The impinging secondary flow has a large effect on enhancing heat transfer. Ooi *et al*. (2002) reported a large inconsistency between the *k-ω* RANS calculations and the experimental observations, resulting in large disagreement between the experimentally measured and the calculated side wall heat transfer. A similar discrepancy in the prediction of the secondary flow was observed in the *k-ω* RANS calculation. But the DES versions of the *k-ω* and the SST models predicted the secondary structures (Figure 25). Near the center of the channel there is a flow towards the ribbed walls. The flow turns near the corners and moves along the smooth walls towards the center of the channel.

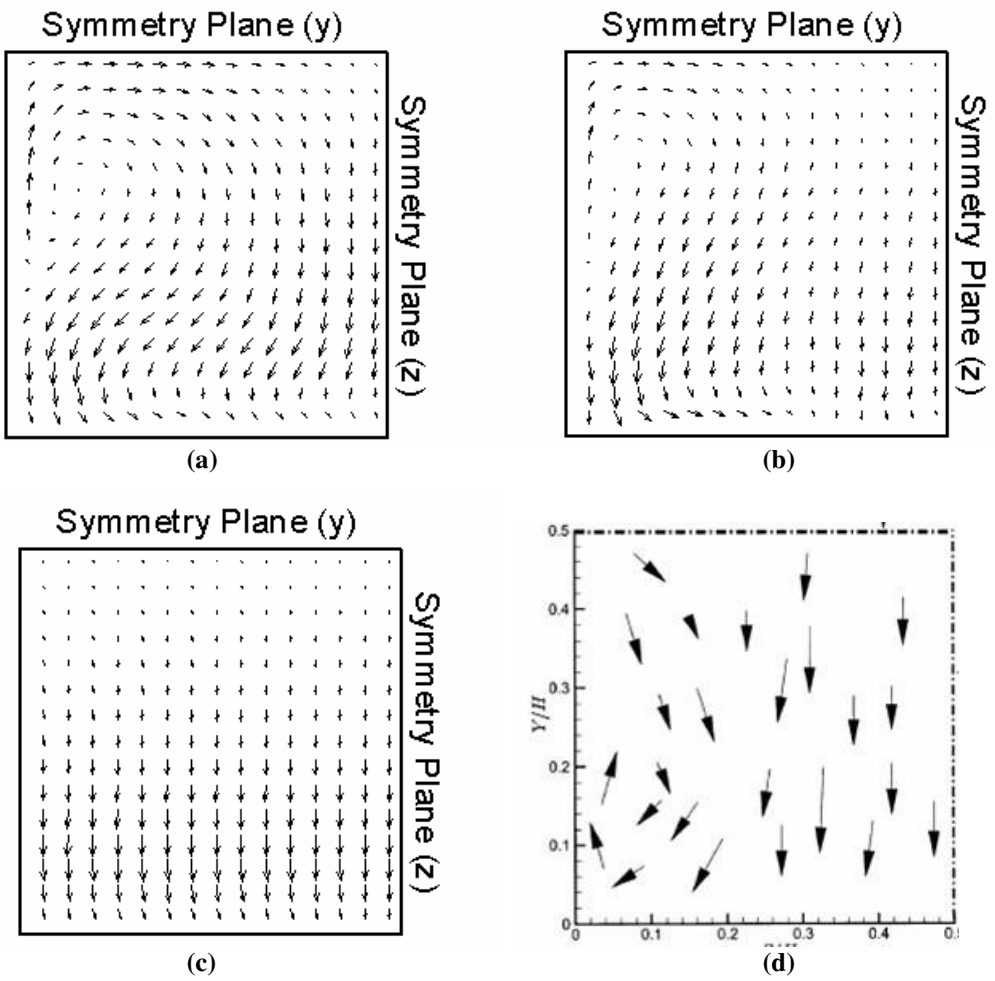

Figure 25 : Comparison of the secondary flow (a) predicted by DES *k-ω* model (b) DES SST model (c) *k-ω* RANS model (d) Experimental (Liou *et al.*).

Table 6 : Comparison of the overall friction factor.

	LES 128^3	DES *k-ω*	DES SST	RANS *k-ω*	Rau et al.
f/f_0	8.60	9.30	9.56	8.76	9.50

The average friction factor augmentation ratios summarized in Table 6 give an estimate of the additional pressure loss incurred due to the introduction of the ribs in the duct. The average friction factor predicted by the DES schemes is very close to the experimentally measured values, and is within an accuracy of 2.5%. The *k-ω* RANS

calculation predicts a value which is within acceptable limits, even though the localized predictions are not accurate. This is due to the over-predictions in some regions compensating for other localized under-predicted values.

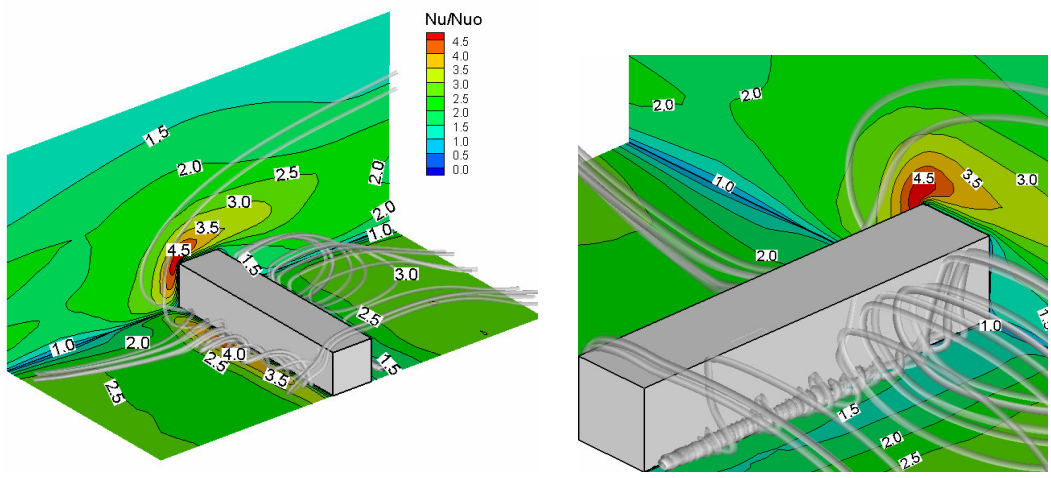

Figure 26 : Streamlines showing the recirculation region in front of the rib and primary and secondary circulations behind the rib and their effect on heat transfer on the walls. Red regions represent high heat transfer, while blue regions represent low heat transfer.

5.3.2 Heat Transfer Enhancement

Figure 26 shows the distribution of heat transfer augmentation at the ribbed wall and the smooth walls of the duct. The augmentation ratio is high in front of the rib as a result of the unsteady junction vortices in this region. These secondary vortices continuously transport cooler fluid from the mainstream to the ribbed wall increasing the heat transfer coefficient. Immediately behind the rib, a secondary recirculation is trapped between the wall and the primary recirculation zone. Although the action of the secondary eddy causes some localized augmentation in this region, the overall augmentation is low and similar to that in a smooth duct. Further downstream, the heat transfer coefficient increases steadily as the vortices from the separated shear layer impinge on the wall. The

heat transfer reaches a maximum value at about 3.5*e* downstream of the rib, which is upstream of the mean reattachment line and coincides with the region of maximum shear. In the spanwise direction, the heat transfer does not show much variation. However, on moving closer to the smooth walls the heat transfer augmentation drops and the minimum heat transfer is observed at the corners formed by the ribbed and the smooth walls. Heat transfer augmentation on the smooth walls is dominated by secondary flow impingement at the top upstream corners of the rib, and decreases towards the center of the channel.

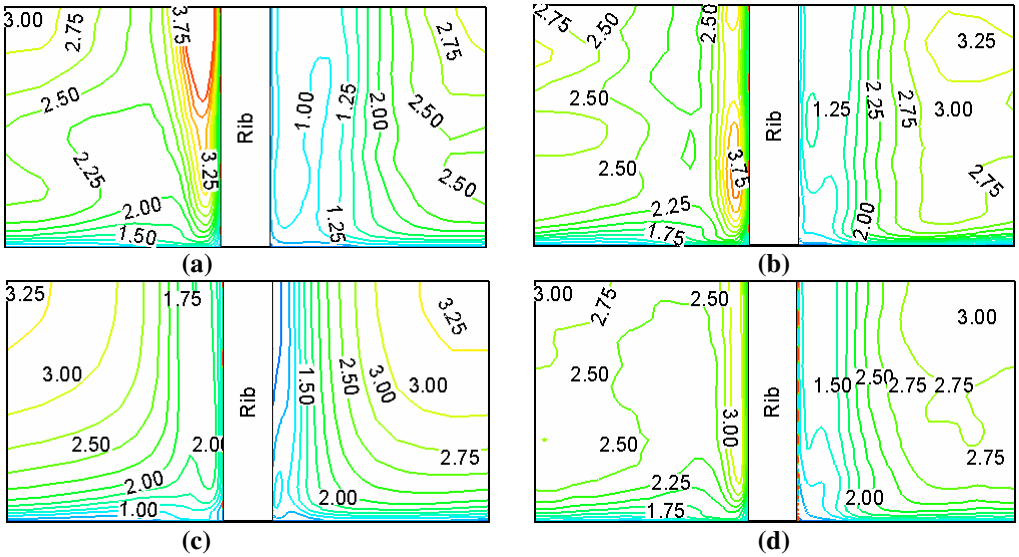

Figure 27 : Comparison of augmentation ratios on the ribbed floor for the (a) *k-ω* DES case (b) Menter's SST DES case (c) *k-ω* RANS case (d) LES case

The distribution of augmentation ratios on the ribbed wall is plotted in Figure 27 and in Figure 28(a) along the centerline. Both DES calculations are consistent with LES and experiments in reproducing the spatial distribution of augmentation ratios, whereas the distribution predicted by RANS is quite different. RANS fails to resolve the secondary eddy behind the rib and its associated effect on augmentation. It also fails to resolve the high augmentation at the front of the rib. These shortcomings can be clearly identified in

Figure 28(a) at the center of the channel, in which the augmentation predicted by RANS immediately before and after the rib is much lower than the other methods. Ooi *et al.* (2002) observed a similar trend. Both DES calculations resolve these features, with the Menter's SST model predicting a solution closer to the experimental measurements. The RANS calculation, in spite of severe shortcomings in predicting the salient features, predicts the augmentation in the inter-rib spacing quite well.

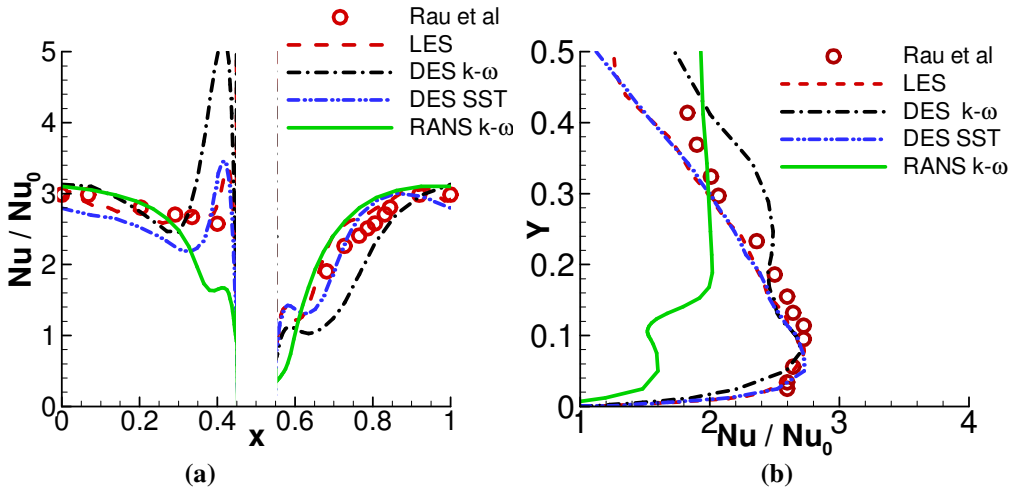

Figure 28 : Comparison of the augmentation ratios (a) at the center of the ribbed floor (b) side walls upstream of the rib

While the heat transfer on the ribbed wall is enhanced due to the streamwise flow, the secondary flow impingement plays a major role in the heat transfer on the side walls. Predictions on the smooth side walls also show the inefficiency of linear eddy-viscosity RANS in Figure 28(b) and Figure 29. The *k-ω* RANS calculation fails to capture the augmentation at the upstream corner of the rib which is caused by the secondary flow impingement. On moving away from the ribbed walls the enhancement ratio is almost constant in *k-ω* RANS, in contrast to the experimental observations, in which the heat transfer decreases on moving towards the center of the channel. The DES predictions

capture the high heat transfer near the rib and also show the decreasing trend in heat transfer.

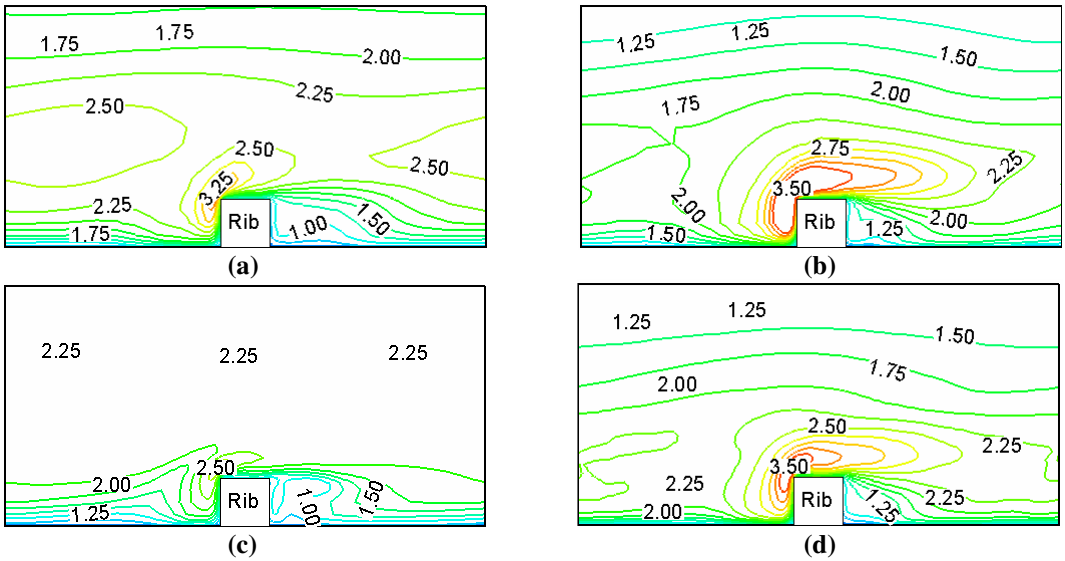

Figure 29 : Comparison of the heat transfer augmentation ratios on the side walls (a) *k-ω* DES (b) Menter's SST DES (c) *k-ω* RANS (d) LES

Table 7 shows the surface averaged augmentation ratios at the ribbed wall, smooth wall and the ribs in comparison to experimental values. All prediction techniques are within 10% of the experiments. However, it is noted that the good agreement of the *k-w* RANS model is fortuitous and is brought about by a cancellation of errors.

Table 7 : Comparison of the overall heat transfer augmentation

	LES 128^3	DES *k-ω*	DES SST	RANS *k-ω*	Rau et al.
Ribbed Wall	2.40	2.17	2.35	2.14	2.40
Error	*0.0%*	*9.4%*	*2.1%*	*10.6%*	
Side Wall	1.89	1.89	1.86	1.83	2.05
Error	*7.7%*	*7.7%*	*9.2%*	*10.8%*	
Ribs	2.89	2.40	2.41	2.38	

5.3.3 Summary and Conclusions

DES and RANS computations are presented in a square duct with normal ribs. The domain is discretized using a 64^3 grid and the computations are compared to the experimental flow and heat transfer results obtained by Rau *et al*. (1998) and LES computations by Tafti (2005).

From the computations performed, the following conclusions can be derived:

1. The average flow characteristics are predicted with good accuracy by the DES computations. DES accurately captures the recirculation regions in front of the rib, behind the rib, and on top of the rib. Owing to the accurate prediction of the main flow characteristics, the heat transfer on the ribbed wall, which is influenced mostly by the main flow, is also predicted with good accuracy.
2. The secondary flow is also accurately captured by the DES computations, while the k-ω RANS fails to capture the secondary flow. Consequently, the heat transfer augmentation on the side walls is predicted with good accuracy by DES, whereas the k-ω RANS calculation fails to accurately capture the side wall heat transfer.
3. The overall flow characteristics and heat transfer predicted by DES agree well with the LES computations and the experimental results, at approximately one-tenth the computational cost of LES.
4. RANS models with known limitations perform better in the DES framework than they would normally in the RANS or URANS framework.
5. By directly resolving more of the turbulent energy, DES, as with LES, is less dependent on the base RANS modeling capability.

5.4 Rotating Duct - Effects of Coriolis Forces

Early studies in turbulent channel flow (Halleen & Johnston, 1967; Lezius & Johnston, 1976) have established two important effects of rotation. When the rotational axis is perpendicular to the plane of mean shear, Coriolis forces have a considerable effect on the mean flow as well as on turbulent fluctuations. These effects are manifested as stabilization/destabilization of turbulence at leading/trailing walls and the generation of spanwise roll cells or secondary flow patterns. The secondary flow patterns are a direct result of the action of Coriolis forces on mean shear and are also observed in laminar flows subjected to system rotation.

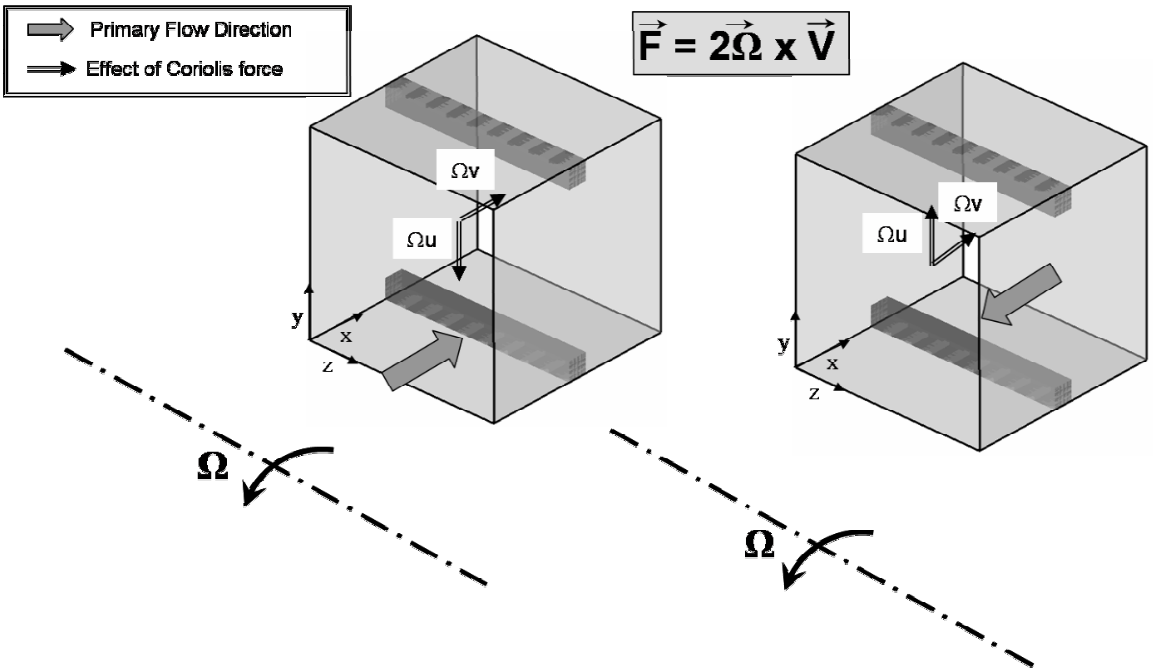

Figure 30: Effect of Coriolis forces in a square duct subjected to rotation

It is well established that the production of turbulence in the near wall region and in shear layers is caused by the exchange of momentum through intense interactions between the fluctuating streamwise and cross-stream velocities. When Coriolis forces act

in tandem with these events, turbulence is augmented, whereas it is attenuated when the two act in opposition. Due to the vector nature of the momentum equations the flow direction determines this bias in the effects of turbulence. The effects of Coriolis forces in a rotating duct are shown in Figure 30. When the direction of the flow is outwards, as considered in the ribbed duct flow in this study, both the turbulent shear layer and near wall turbulence on the trailing surface are augmented by the direct effect of Coriolis forces, while the opposite effect comes into play at the leading wall.

Modern propulsion turbines used in aircrafts rotate at a non-dimensional rotation number of around 0.2. Gas turbines used for power generation have a higher rotation rate (Ro = 0.5 – 1.0), as compared to the aircraft engines. In the study three rotation numbers – Ro = 0.18, 0.35 and 0.67 are examined which cover a wide range of turbine applications. The results obtained using DES are evaluated against the detailed results obtained from LES (Abdel-Wahab and Tafti, 2004).

5.4.1 Mean Flow field

The flow at the center (z=0.5) of the duct is characterized by a large recirculation region behind the rib, a small region of recirculation in front of the rib, a small eddy on top of the rib and an eddy trapped behind the rib, between the large recirculation region and the rib. For a non-rotating case all these features are similar on both the ribbed walls.

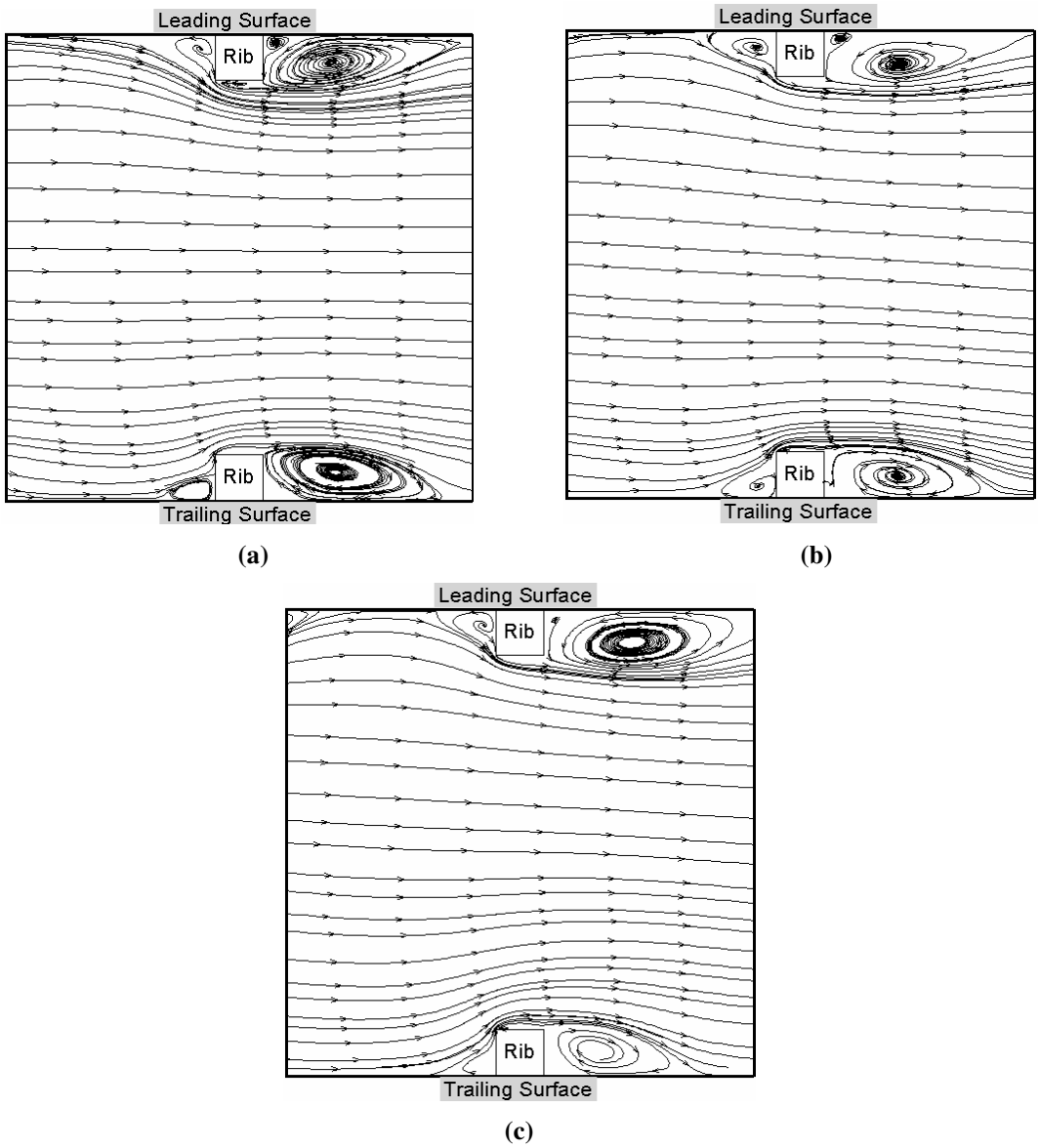

Figure 31: Streamlines showing the flow in a fully developed duct as predicted by DES SST at Z = 0.5 (a) Ro = 0.18 (b) Ro = 0.35 (c) Ro = 0.67. Y = 0 represents the trailing wall, while Y = 1 represents the leading wall. Flow direction is from left to right.

Figure 31 shows the streamlines at the center of the duct (z = 0.5) for the three rotation cases. Rotational Coriolis forces affect the size of the recirculation zones and so the flow is asymmetric about the center *y*-plane of the duct. The reattachment length increases at the leading wall and decreases at the trailing wall with rotation number. The

reattachment is observed at around 4.0*e* for Ro = 0.18 at the trailing side. The size of the separation bubble decreases to a value close to 3.6*e* when the rotation increases to 0.35. On increasing the rotation further to 0.67 the reattachment length remains almost the same as the 0.35 case. On the other hand, the reattachment length at the leading wall increases from a value of 4.25*e* for the stationary case (Ro = 0.0) to a value of 4.5*e* at Ro = 0.18. No significant change is observed as the Ro is increased to 0.35, but on increasing the rotation further to 0.67, the recirculation region is observed to increase to a value of around 6.7*e*, and as a result it almost merges with the recirculation region in front of the next rib.

The reattachment lengths for the rotating cases are consistent with the LES predictions (Abdel-Wahab *et al.,* 2004). Figure 32 shows the comparison of the flowfield as predicted by LES, DES and URANS. The separation and reattachment downstream of the rib is predicted accurately by DES and the reattachment length is in agreement with LES both at the leading and the trailing walls. However URANS overpredicts the reattachment lengths both at the leading as well as the trailing wall. Overprediction of the reattachment lengths is a result of the inability of the SST model to account for the effects of Coriolis forces, whereas in DES, the effect of Coriolis forces is captured in the resolved scales.

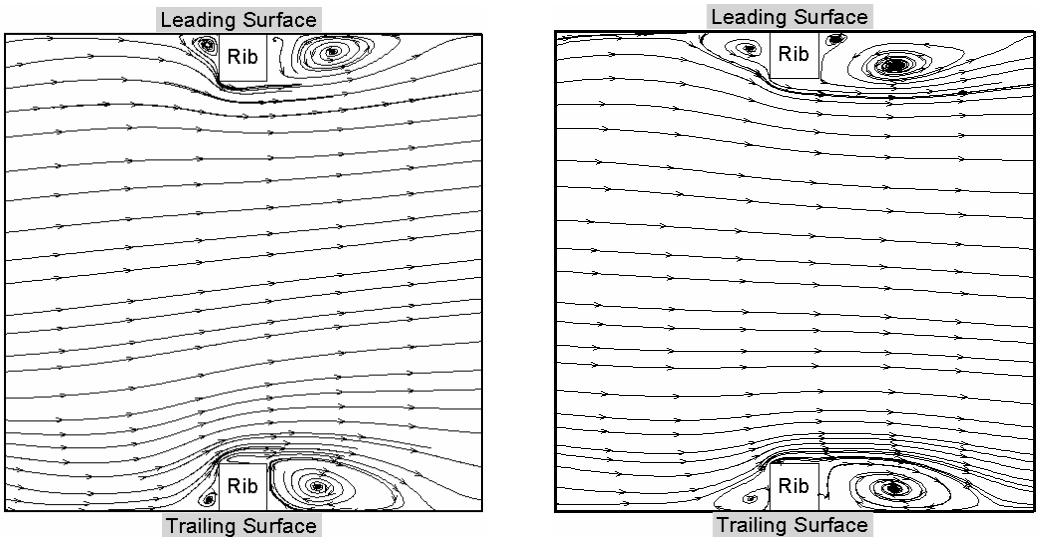

Figure 32: Streamlines showing the flow in a fully developed duct rotating at Ro = 0.35 at Z = 0.5 as predicted by (a) LES (b) DES SST (c) URANS SST. Y = 0 represents the trailing wall, while Y = 1 represents the leading wall. Flow direction is from left to right.

Figure 33 shows the magnitude of the secondary flows (*v, w* velocities) for the stationary and the three rotation cases in the cross-section of the duct on top of the rib. The *v*- and *w*- velocities are plotted individually in each half of the span. Above the rib, the constriction posed by the rib results in flow being pushed towards the channel center,

both at the center of the span and near the side wall. In addition to this effect, a spanwise flow is setup toward the center and toward the side wall which is represented by the high positive impingement *w*-velocities at the side wall. As rotation increases, the strength of the secondary impingement flow at the trailing side increases while it decreases at the leading side, which is evident from the penetration of the high *v*-velocities towards the leading side near the side wall. The asymmetry in the *w*-velocity slightly increases as the rotation increases.

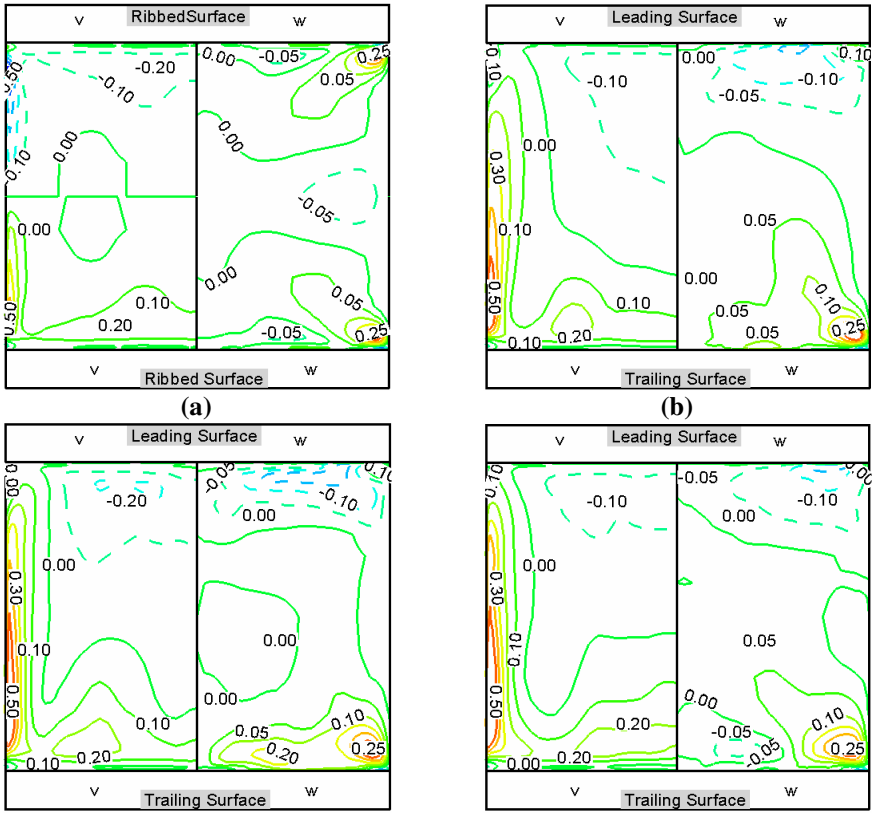

Figure 33: Secondary flow contours on the rib for (a) Ro = 0.0 (b) Ro = 0.18 (c) Ro = 0.35 (d) Ro = 0.67 as predicted by DES SST. The contours show the effect of rotation on the secondary flow in the cross-section.

5.4.2 Turbulent Flow Characteristics

A comparison of the turbulent kinetic energies (TKE) predicted by the DES, LES and the URANS schemes are shown in Figure 34. The resolved component of TKE is considered for comparison for the LES cases, while the sum of the resolved and the modeled components are considered for the DES and URANS cases. It is observed that the resolved component of TKE is significantly larger than the modeled component in the DES computation almost in the entire flow field. On the other hand the resolved and the modeled components make equal contributions in URANS.

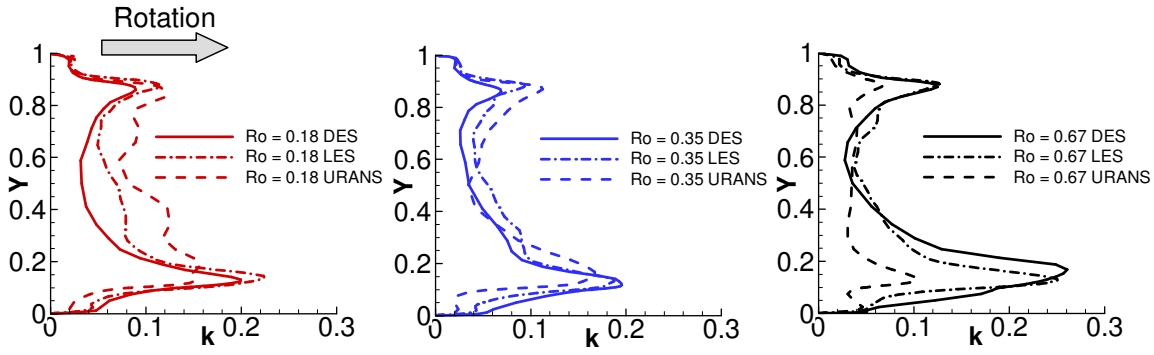

Figure 34: TKE values as predicted by the DES, LES and the URANS cases for the three rotation cases at z = 0.5 and x = 0.65, i.e., 1e downstream of the rib.

A comparison of the TKE in between the rib shows that the values resolved by DES compare well with that resolved by LES for all the three rotation cases. The plotted location is one rib distance downstream of the rib and so represents the separation region for all the three cases both at the trailing and the leading sides. The turbulence statistics in the vicinity of the wall (Y < 0.1) region determine the reattachment point downstream and the heat transfer at the ribbed walls. It is observed that the TKE values predicted in the boundary layer by DES compared well to LES for all the other rotation cases. On the other hand, URANS underpredicts the TKE values in this region for all the cases. The

low turbulence levels in URANS results in larger recirculation regions as compared to DES and LES.

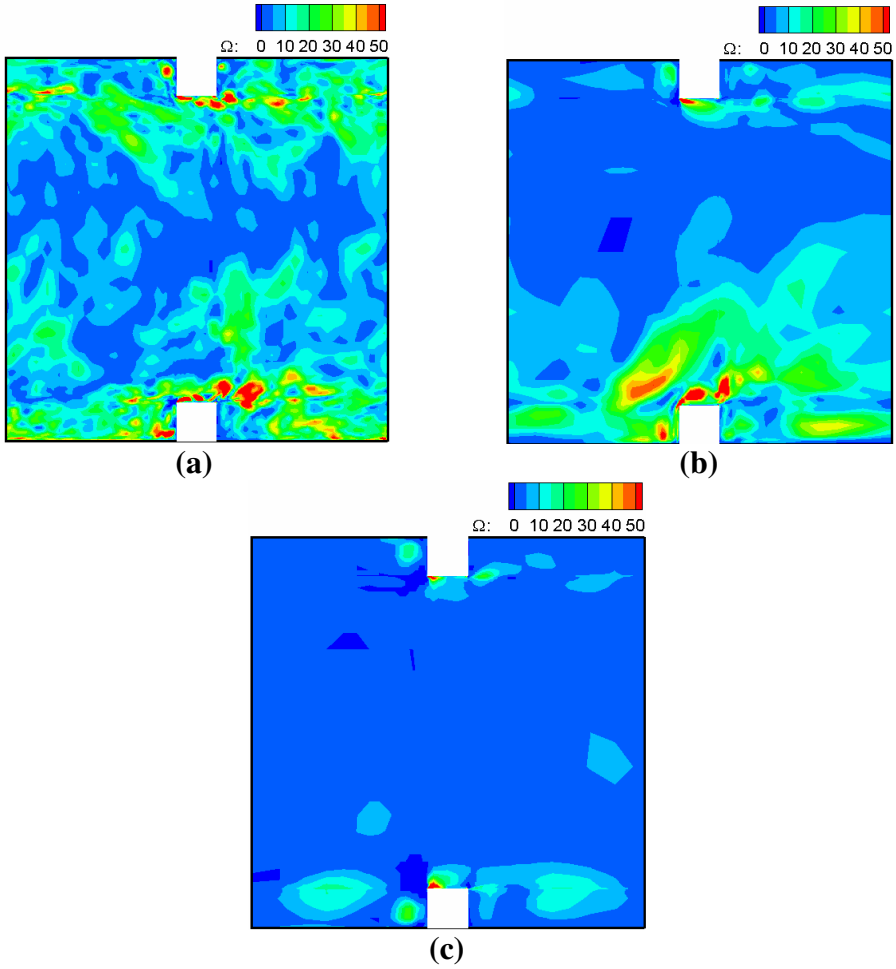

Figure 35: Coherent vorticity contours for the (a) LES 128^3 (b) DES 64^3 (c) URANS 64^3 for Ro = 0.35 show the scales resolved of the three schemes. The flow in all cases is from left to right

A comparison of the instantaneous coherent vorticity (Chong *et al*, 1990) as predicted by 128^3 LES, 64^3 DES and 64^3 URANS is shown in Figure 35. These plots give an idea of the flow structures resolved by the three schemes. It is observed that the magnitude of coherent vorticity and the characteristics predicted by DES is consistent with the magnitudes predicted by LES on a much finer grid. Predictions by URANS show lower vorticity levels as compared to LES and DES, both in the center of the duct as well as the

inter-rib region. Thus the small modification in the URANS model to convert it into an equivalent DES model substantially improves the resolution of the simulation.

5.4.3 Mean Heat Transfer

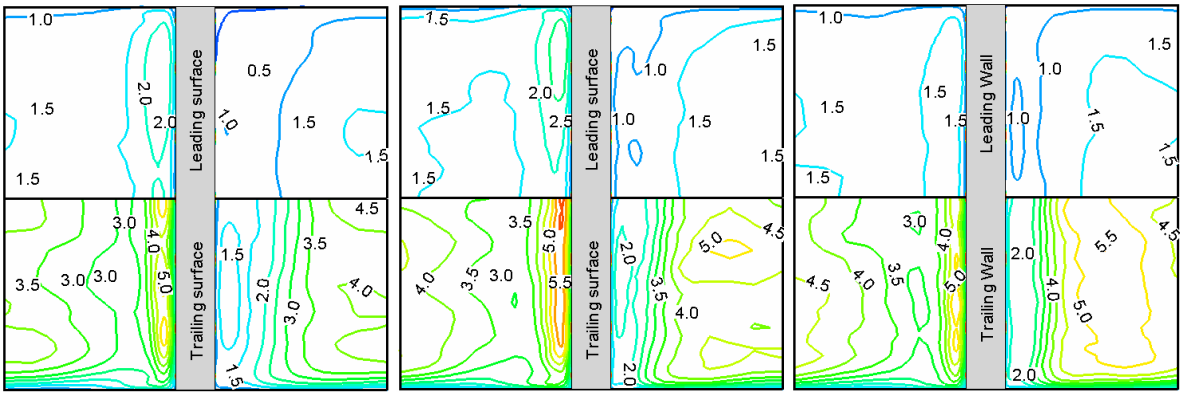

(a) (b) (c)

Figure 36: Heat transfer augmentation (Nu/Nu_0) predicted at the leading and the trailing walls by DES SST for (a) Ro = 0.18 (b) Ro = 0.35 (c) Ro = 0.67. Flow direction is from left to right.

The heat transfer trends at the leading and trailing walls are similar to the trends observed at the ribbed walls for the stationary case. The augmentation ratio is high in front of the rib as a result of the unsteady vortices in this region. These secondary vortices continuously transport cooler fluid from the mainstream to the ribbed wall increasing the heat transfer coefficient. Immediately behind the rib, a secondary recirculation is trapped between the wall and the primary recirculation zone. Although the action of the secondary eddy causes some localized augmentation in this region, the overall augmentation is low and similar to that in a smooth duct. Further downstream, the heat transfer coefficient increases steadily as the vortices from the separated shear layer impinge on the wall.

Figure 36 shows the heat transfer at the leading (upper half) and the trailing walls (lower half) for the three rotation cases. As the rotation number is increased, an increase

in the heat transfer is observed at the trailing wall, especially in regions immediately upstream of the rib and near the reattachment point. This is countered by a decrease at the leading wall in the corresponding regions.

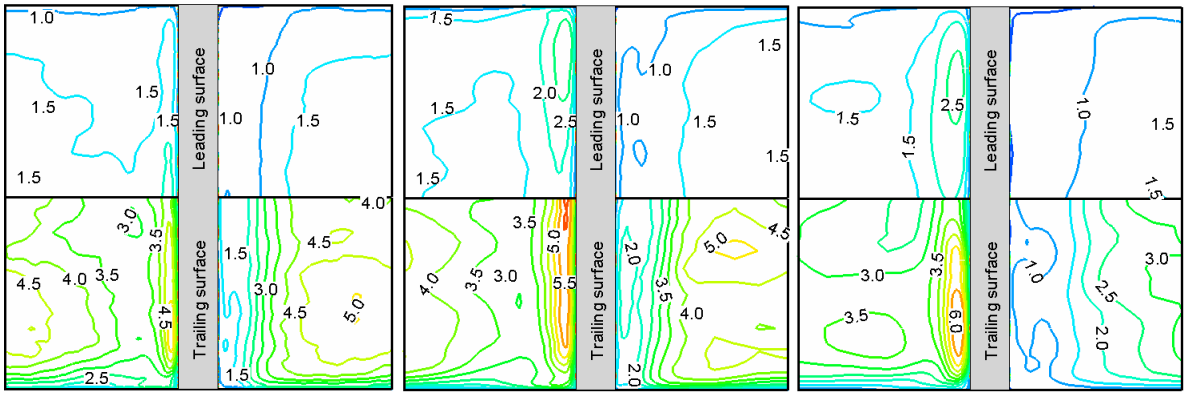

(a) **(b)** **(c)**

Figure 37: Heat transfer augmentation (Nu/Nu_0) predicted at the leading (upper half of the plot) and the trailing walls (lower half of the plot) for the Ro = 0.35 case by (a) LES (b) DES SST(c) URANS SST. Flow direction is from left to right.

Figure 37 shows a comparison of the DES and the URANS with LES results at Ro=0.35. This shows that the URANS under-predicts the heat transfer at the trailing side where the turbulence is enhanced by rotation. The heat transfer augmentation predicted by DES agrees quite well with the LES computations. The peak heat transfer on the trailing wall in the region of shear layer reattachment is shifted away from the center of the duct due to the effect of secondary flows and is captured by all three methods. However, the URANS predicts this region further downstream because of the larger reattachment length. Heat transfer augmentations at the trailing wall reach values close to 5.0 immediately upstream of the rib where the unsteady vortices enhance the heat transfer. Both DES and URANS tend to over-predict the spatial extent of this region.

The flow at the leading wall is more stable than the flow at the trailing wall and so the overall heat transfer at the leading wall is almost half the heat transfer at the trailing wall.

Upstream of the rib, heat transfer levels are almost 2.5 times that observed in a smooth duct case. Once again, both DES and URANS overpredict the extent and augmentation in this region. The heat transfer levels drop to values close to the smooth channel heat transfer values immediately behind the rib, but the augmentation increases to values close to 1.5 downstream of the reattachment point.

The trends predicted by DES are consistent with the LES results (Abdel-Wahab *et al.,* 2004), with the exception of the region immediately upstream of the rib where higher levels of heat transfer are predicted. Similar results were observed in a stationary duct where a larger heat transfer augmentation was observed immediately upstream of the rib. On the other hand URANS results show a lot of discrepancy. The most prominent deviation from LES is the under-prediction of the heat transfer at the trailing wall of the duct. The heat transfer distributions at the ribbed walls are also much smoother than LES and DES predictions.

The secondary flows in the stationary and the rotation cases play an important role in the heat transfer at the side walls. Along the smooth (side) walls the heat transfer increases on moving from the trailing wall and reaches a maximum at the top front corner of the rib as a result of the secondary flow impingement on the wall. The heat transfer decreases on the side walls towards the center of the channel. Though the heat transfer patterns are the same for the stationary and the rotation cases the magnitudes of heat transfer are higher when rotation is introduced.

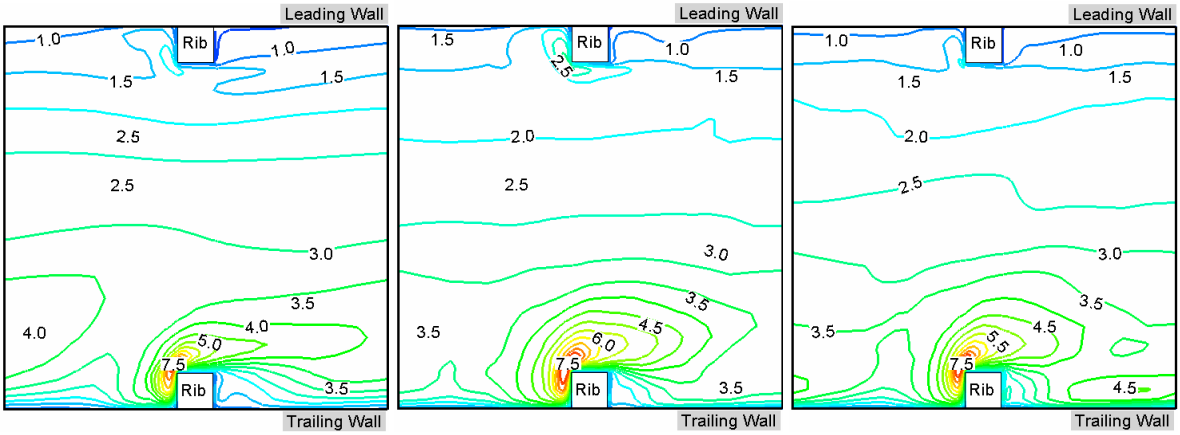

(a) **(b)** **(c)**

Figure 38: Heat transfer augmentation (Nu/Nu_0) predicted at the side wall by DES SST for the (a) Ro = 0.18 (b) Ro = 0.35 (c) Ro = 0.67. Flow direction is from left to right.

For Ro = 0.18 (Figure 38) the secondary flow impingement results in levels of heat transfer as high as seven times that in a smooth channel at the trailing wall, at the corner of the rib and the side wall. The heat transfer decreases to values close to 2.0 towards the center of the duct. On moving towards the leading side the heat transfer decreases further and drops to values close to unity near the leading wall of the side wall. However secondary flow impingement near the corner of the ribs locally results in higher heat transfer. An increase in rotation does not show much effect on the side wall heat transfer. This behavior is consistent with the observations of Wagner *et al.,* (1992) who observed little or no changes in the heat transfer at the side walls as rotation rate increases.

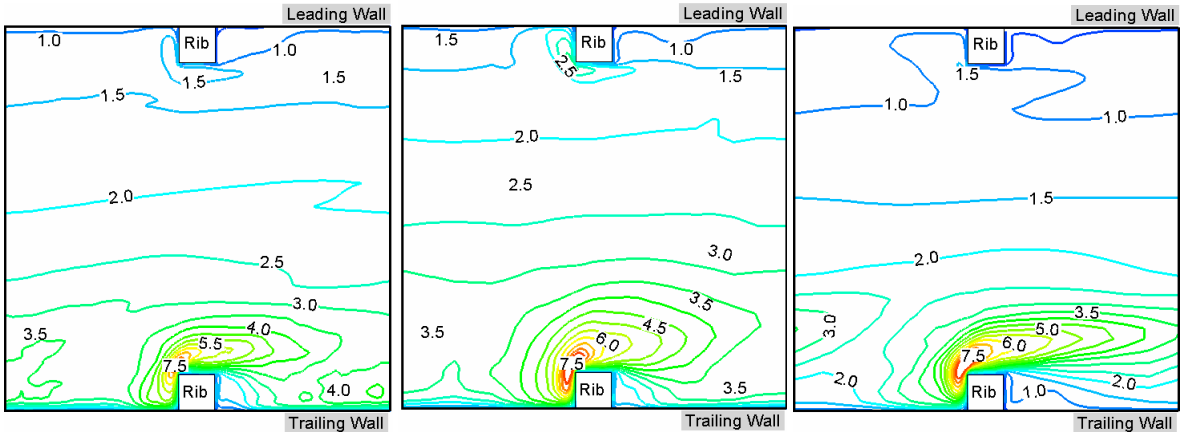

Figure 39: Heat transfer augmentation (Nu/Nu_0) predicted at the side wall for the Ro = 0.35 case by (a) LES (b) DES SST(c) URANS SST. Flow direction is from left to right.

Figure 39 compares the side wall heat transfer predicted by DES and URANS with LES for Ro = 0.35. The DES predictions compare well with LES. URANS predicts comparable trends. However the augmentation ratio is underpredicted at the center of the duct and in the vicinity of the trailing wall.

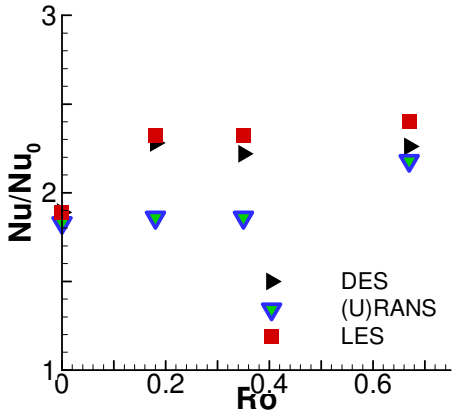

Figure 40: Side wall heat transfer predicted by LES, DES and URANS for the various rotation cases.

Figure 40 shows a gradual, but small increase in the average heat transfer augmentation at the side walls as the rotation number increases from 0.18 to 0.67. DES predicts these trends accurately but slightly underpredicts the augmentation compared to LES at higher rotation rates. URANS severely underpredicts the side wall heat transfer at Ro = 0.18 and 0.35, while the agreement is comparatively better at the highest rotation number.

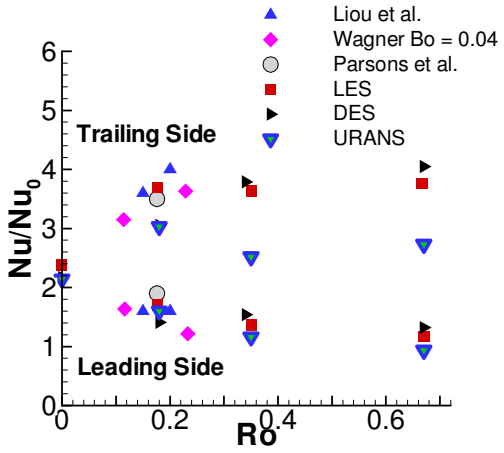

Figure 41: Comparison of average Nusselt number augmentation ratios at the leading and trailing sides with experiments.

The effect of rotation is more prominent at the leading and the trailing walls. Results for averaged Nusselt numbers on the leading and trailing faces for the three rotation numbers are compared with the experiments of Liou et al. (2001), Parsons et al. (1994), and Wagner et al. (1992). The experimental data of Liou *et al.* (2001) is at Re = 10,000 for e/D_h = 0.136 and P/e = 10 and Parsons *et al.* (1994) data is obtained at Re=5,000 for e/D_h = 0.125 and P/e = 10. The data of Wagner *et al.* (1992) includes the effects of buoyancy with a density ratio = 0.13 for a staggered rib arrangement with e/D_h = 0.1 and P/e = 10 at Re=25,000. Wagner's data includes the effects of centrifugal buoyancy which increase trailing wall heat transfer as the rotation number increases. In all cases, fully-

developed data is extracted for comparison. Figure 41 compares the overall heat transfer augmentations at the leading and trailing walls predicted by DES and URANS cases, with the LES computations and experimental results. DES predictions agree well with experiments and LES. On the other hand, URANS substantially underpredicts the trailing wall augmentation, by as much as 30% compared to LES, at the high rotation numbers of 0.35 and 0.67. Prediction accuracy of URANS is similar to that of DES at the leading wall which is within 10% of LES.

5.4.4 Conclusions

Results from DES and URANS of a fully developed flow in a 90° ribbed duct are presented for three rotation cases – Ro = 0.18, 0.35 and 0.67 at a Reynolds number of 20,000. The computations were performed on a 64^3 mesh tested earlier for a stationary case which is almost an order of magnitude less expensive than the analogous LES computation (Abdel-Wahab and Tafti, 2004).

The effect of rotation is observed by an increase in the turbulence intensity at the trailing wall due to which the reattachment length decreases. Secondary flow impingement is observed to become stronger as rotation increases. These flow features result in an increase in the heat transfer at the trailing wall. The peak heat transfer level increases from a value of about 3.0 for the stationary duct to a value of about 6.0 for the largest rotation. The overall heat transfer at the trailing wall increases by almost a factor of 1.5 as the system is rotated from rest to Ro = 0.67.

At the leading wall the opposite effect is observed. Rotation damps turbulence at the leading wall resulting in larger recirculation regions. It is observed that the recirculation region downstream of the rib almost overlaps the recirculation region upstream of the

next rib. This results in low levels of heat transfer at the leading wall. The heat transfer distribution drops to values close to that in a smooth duct for the highest rotation considered.

The heat transfer at the side walls show distributions similar to a stationary duct. The heat transfer is high at the corner of the rib, which is due to the impingement of the secondary flows on the side walls. The heat transfer decreases on moving from the trailing wall to the leading wall. Rotation increases the magnitude of the secondary flows and increases the heat transfer augmentation on the side walls.

The flow and heat transfer distribution predicted by the DES SST case is consistent with the LES predictions. Though higher heat transfer is predicted immediately upstream of the rib, the distribution in the other regions is accurate. The overall predicted heat transfer also match well with the LES predictions and the experimental observations. URANS fails to capture the effects of the Coriolis forces at the trailing wall and underpredicts the heat transfer.

In summary, it is concluded that DES accurately predicts the physics of the rotation dominated flow, in addition to accurately predicting separation and reattachment and unsteady vortex induced secondary motions. The main contribution of this work is in establishing that DES, like LES, can produce quality results at a cost which is an order of magnitude less than an equivalent LES. It is also observed that the URANS model when used in a DES mode overcomes the deficiency of the base model and predicts the effects of shear and rotation in the flow and heat transfer in the fully developed region of the internal cooling duct.

5.5 Rotating Ducts - Effects of Coriolis Forces and Centrifugal Buoyancy

The study of the flow and heat transfer in rotating ducts, considering the effects of the Coriolis forces and neglecting centrifugal buoyancy shows that URANS fails to capture the effects of rotation. However, RANS when applied in the DES mode captures the effects of rotation. Since the application of DES in capturing the effects of Coriolis forces has been validated, the next step is to test and validate the capabilities of DES in predicting the flow and heat transfer in internal cooling passages when the centrifugal buoyancy effects introduced by the temperature difference at the trailing and leading walls of the passage become significant. The advantage of applying DES is two-fold – to cut down the computational cost associated with LES and to eliminate the deficiencies observed in using standard eddy viscosity RANS models. The main objective of this part of the study is to validate the performance of DES in capturing the mixed convection effects introduced in the flow in a ribbed duct due to the action of shear, rotation and buoyancy.

In the cases studied three different rotation cases are considered – Ro = 0.18, 0.35 and 0.67. Three different density ratios are studied to evaluate the capability of DES in predicting the effects of buoyancy. The effective buoyancy numbers (Bo) for the three cases are evaluated to be 0.00, 0.12 and 0.29 respectively. In the present context the density difference and the buoyancy number are related as $Bo = \frac{\Delta\rho}{\rho_0}\frac{r}{D_h}Ro^2$. In all the cases the centrifugal buoyancy complements the effects of Coriolis forces. In typical gas turbine applications the buoyancy parameters can reach values of upto 1.0. However

since detailed LES results (Abdel-Wahab and Tafti, 2004) are available for the buoyancy parameters in the range of 0.00 – 0.30, the current studies are carried out for the relevant density ratios.

The detailed flow and heat transfer physics is compared with LES prediction by Abdel-Wahab and Tafti (2004) on a 128^3 grid. Considering the grid sizes and the time scales used for the LES and DES calculations, the cost of the DES computation is almost an order of magnitude less than the LES computation (Abdel-Wahab and Tafti, 2004). The surface averaged heat transfer augmentation has been validated with heat transfer data from Wagner *et al.,* (1992) and the LES computation (Abdel-Wahab and Tafti, 2004).

5.5.1 Effects of Centrifugal Buoyancy

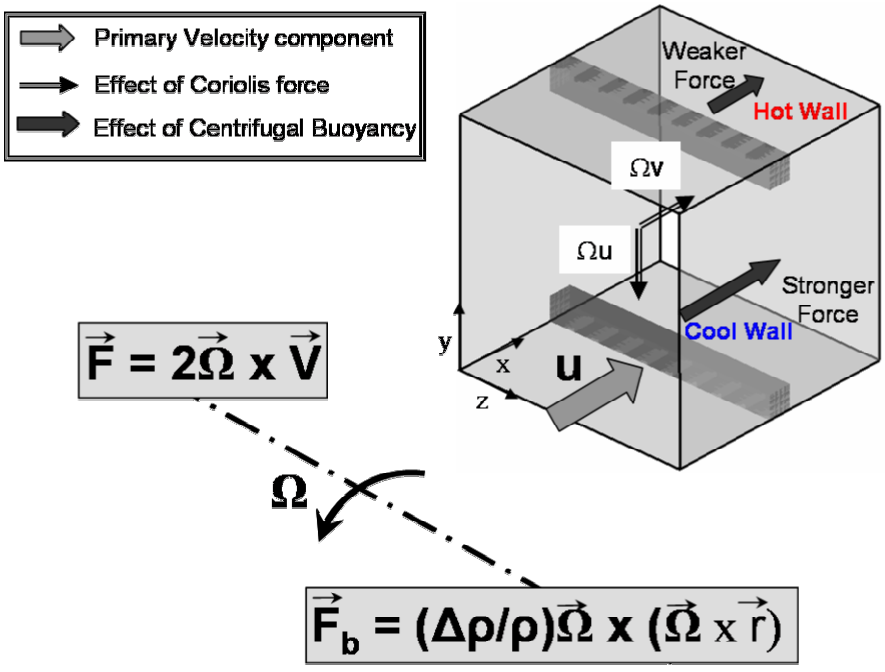

Figure 42: Effect of Coriolis forces (F) and Centrifugal Buoyancy (F_b) in rotating ducts

Rotation induces Coriolis forces that accentuate the turbulence and destabilizes the flow on one side and attenuates turbulence and stabilizes the flow at the other side. This has a direct effect on the heat transfer at the ribbed walls. Due to the vector nature of the equations of motion, the flow direction has a significant influence on the effects of Coriolis forces and Centrifugal buoyancy. When the flow is radially outwards, the heat transfer at the trailing wall is observed to be higher than the heat transfer at the leading wall (Figure 42). The opposite trend is observed when the flow is radially outwards. Section 5.4 which studies the effect of Coriolis forces on radially outward flows show that as the rotation in the duct is increased to a value of Ro = 0.67, the rib averaged heat transfer increases by a factor of around 65% as compared to the stationary duct at the trailing wall. On the other hand the heat transfer at the leading wall decreases by a factor of around 75%. This difference in the heat transfer results in the fluid near the leading wall to be warmer than the fluid at the trailing wall. Difference in the densities of the fluids in the vicinity of the ribbed walls induces centrifugal buoyancy. In the radially outward flow considered the centrifugal buoyancy aids the effects of Coriolis forces.

5.5.2 Mean Flow Features

Studies in the hydrodynamically and thermally fully developed flow in a ribbed duct show that as rotation is increased the separation region at the leading side increases in size, while it decreases at the trailing side. While the size of the recirculation region downstream of the rib at the trailing side reaches a constant value as the rotation increases, considerable changes in the reattachment lengths are observed at the leading wall. Figure 43 shows the comparison of the reattachment lengths at the center (z = $0.5D_h$) of the leading wall for the three rotation cases. The effects of rotation for a

constant buoyancy number (Bo = 0.12) is shown. It is observed that as the rotation is increased from 0.18 to 0.67, the reattachment length increases from a value of around 5e to a value of 8.5e at the leading surface.

Comparison of the recirculation regions for the three rotation cases with predictions by LES show that the recirculation regions for Ro = 0.18 and 0.35 are consistent with the predictions by LES. The recirculation region predicted for the highest rotation case is slightly different. The effective rotation number for the largest rotation case is around 0.74 as compared to the value of 0.67 used for the DES case, which could potentially lead to the difference in the reattachment lengths.

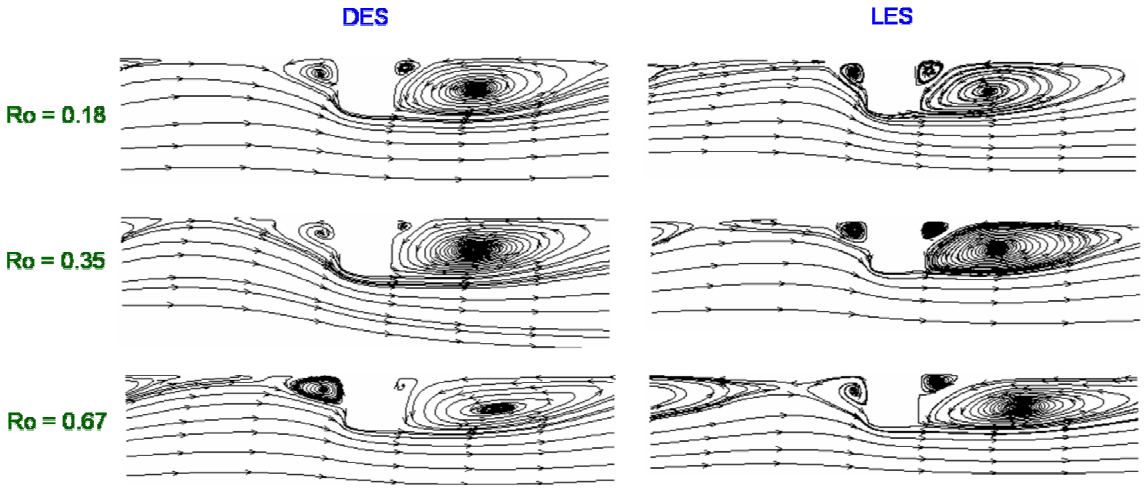

Figure 43: Comparison of the recirculation regions at the leading edge for the three rotation cases with Bo = 0.12.

Centrifugal buoyancy, like Coriolis forces affects the recirculation region at the leading wall. Figure 44 shows the recirculation regions at the leading wall for a constant rotation rate of Ro = 0.35 and different buoyancy numbers. It is observed that as the buoyancy number is increased from a value of Bo = 0.00 to Bo = 0.29, the recirculation

region grows until one large recirculation zone is observed at the leading wall for Bo = 0.29.

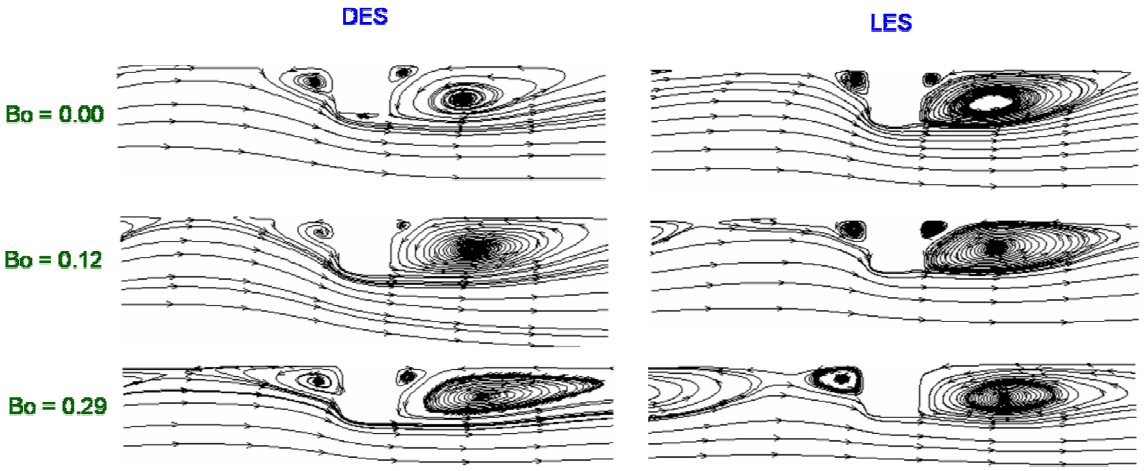

Figure 44: Comparison of the recirculation regions at the leading edge for the three different buoyancy cases with Ro = 0.35.

A comparison with LES shows concurrence. The structure of the recirculation regions for Bo = 0.00 and 0.12 are reproduced by DES. For Bo = 0.29, while one large recirculation region is observed in between the ribs, the structure of the recirculation regions is different as predicted by LES and DES.

The effects of Coriolis forces on the secondary flow in the duct cross-section showed an increase in the vertical velocity as the rotation is increased. Figure 45 shows the effect of buoyancy on the secondary flows for the rotation number of Ro = 0.35. The magnitude of the secondary flows (*v, w* velocities) for the stationary and the three rotation cases in the cross-section of the duct on top of the rib are shown and the *v*- and *w*- velocities are plotted individually in each half of the span. A strong component of vertical velocity is observed in the vicinity of the side walls. At the core of the channel, a milder upwash is observed which propagates upwards as the buoyancy is increased. This can be observed from the movement of the zero vertical velocity contour line from the lower half of the

duct towards the upper half as buoyancy number is increased. So as buoyancy increases, the cross-stream flow results in a tendency of the fluid to accumulate at the leading surface.

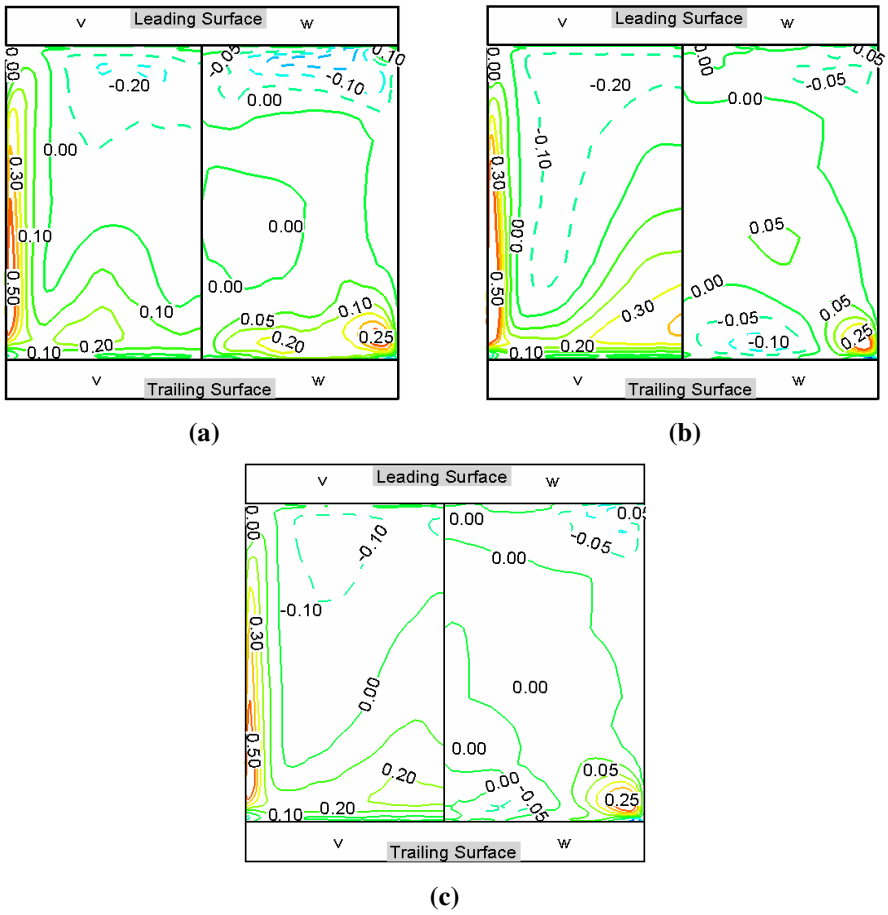

Figure 45: Comparison of the secondary velocities for Ro = 0.35 for varying buoyancies (a) Bo = 0.00 (b) Bo = 0.12 (c) Bo = 0.29

Very small differences are observed in the lateral velocity components in the duct as the buoyancy number is increased. Positive velocities represent flow toward the side wall while negative velocities represent flow towards the core of the duct. A high lateral velocity is observed near the rib – side wall junction at the trailing wall. The magnitude of this high velocity is observed to be almost constant as the buoyancy is increased. This

feature is consistent with the LES predictions by Abdel-Wahab and Tafti (2004) that show a negligible increase in the lateral velocities as the buoyancy is increased from 0.00 to 0.29.

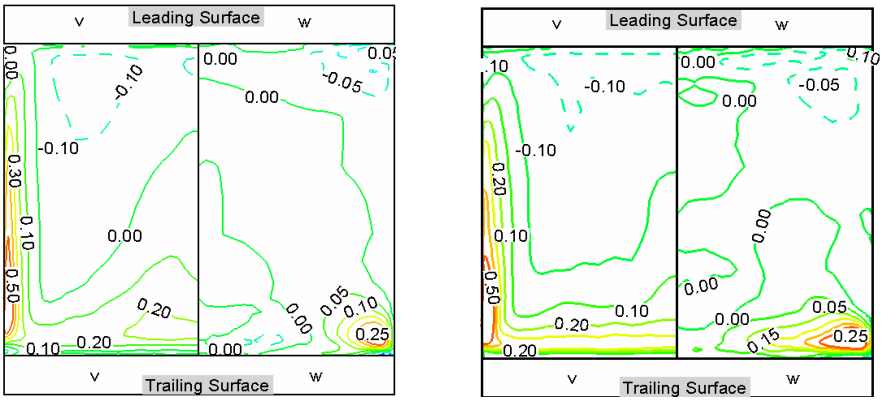

Figure 46: Comparison of the secondary flows as predicted by DES and LES at the center of the rib region for Bo = 0.29 and Ro = 0.35, for (a) DES (b) LES.

A one-to-one comparison of the secondary flow features with flow prediction by LES for Ro = 0.35 and Bo = 0.29 is shown in Figure 46. Comparison at the center of the rib shows that the magnitude and extent of the high vertical velocity region, the downwash at the leading surface and the upwash at the trailing surface, the strong component of lateral flow near the trailing surface, and the component of lateral flow towards the core of the duct are all reproduced well by DES.

5.5.3 Turbulent Flow Features

The turbulent kinetic energy (TKE) at the center of the inter-rib space ($x = D_h$, $z = 0.5D_h$) is reported in Figure 47. Since the flow towards the center of the domain is evaluated in the LES mode, the resolved component of TKE is much larger than the modeled component. Therefore the effective TKE values for DES can be obtained by

considering the TKE resolved by the sub-grid scales. While comparisons have been carried out with LES, the effect of rotation and buoyancy are simultaneously studied.

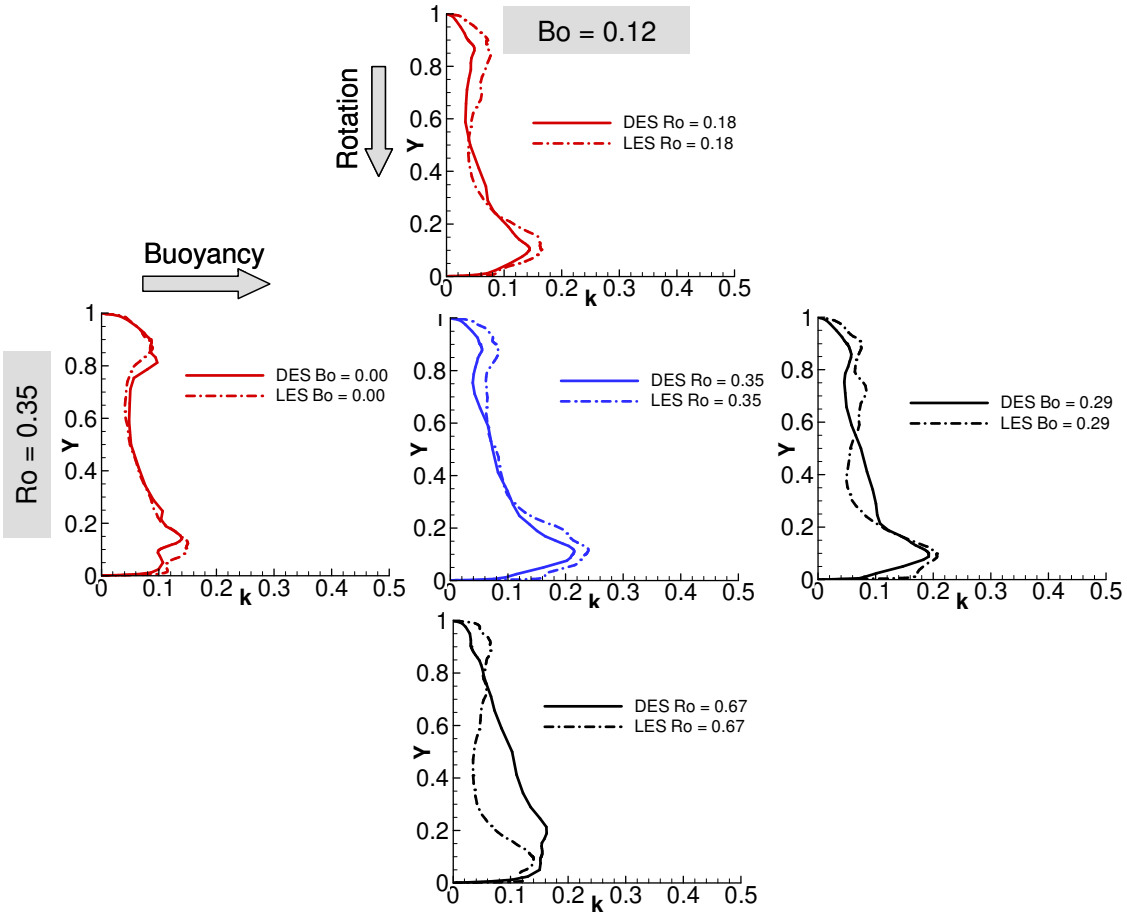

Figure 47: Comparison of the turbulent kinetic energy in between two consecutive ribs at z = 0.5.

With an increase in rotation, the TKE value at the trailing surface is observed to increase as Ro is increased from 0.18 to 0.35. However, as the rotation is increased to a value of 0.67, the peak TKE value at the trailing surface decreases. At the leading surface the peak turbulent kinetic energy is observed to be almost constant. The TKE profiles predicted by DES compare well with the profiles predicted by LES, except for the largest rotation case where the TKE at the core of the duct is observed to be over-predicted as compared to LES. The TKE is underpredicted in the boundary layer as the near wall

region is modeled using URANS and the modeled component of TKE is a significant part of the total TKE.

As the buoyancy is increased from a value of Bo = 0.00 to Bo = 0.12 it is observed that the peak TKE at the trailing surface increases from a value of around 15% to about 22%. A corresponding decrease in the TKE is observed at the leading surface where the TKE value drops from a value of around 9% to a value of 7%. Little difference is observed in the value of the peak TKE values at the leading and trailing surfaces as the buoyancy is increased to Bo = 0.29. The trends and the TKE profiles match well with LES.

5.5.4 Heat Transfer Augmentation

Rotation augments the heat transfer at the trailing surface and decreases the heat transfer at the leading surface. From the comparison of the heat transfer for varying rotation cases (for a zero buoyancy case) it was observed that as the rotation increases, the heat transfer at the trailing surface increases, and the heat transfer at the leading surface decreases correspondingly.

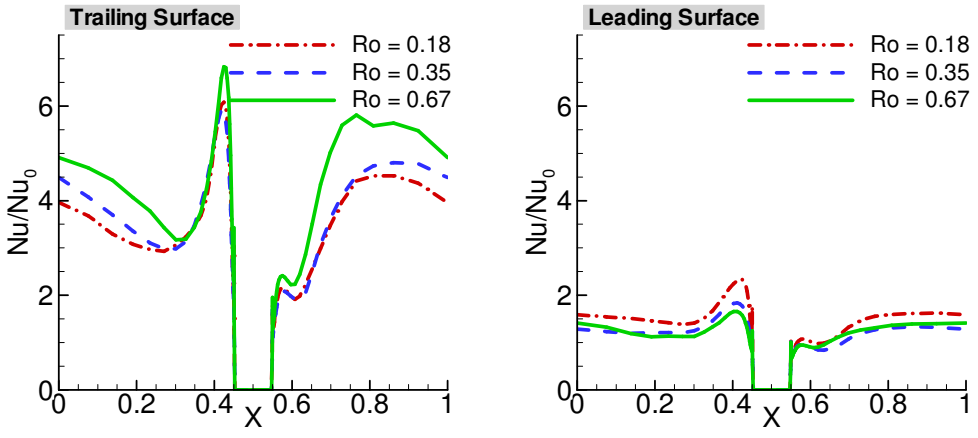

Figure 48: Heat transfer distribution at the center of the duct (z/D_h =0.5) at the leading and trailing surfaces. Buoyancy in all the cases is Bo = 0.12

Heat transfer augmentation profiles plotted for varying rotation cases (for a constant Bo = 0.12) are shown in Figure 48. The trends in heat transfer are observed to be similar to that observed for a zero buoyancy case. The highest heat transfer is observed in the region upstream of the rib where the unsteady vortices enhance the heat transfer. Regions of high heat transfer are also observed in the inter-rib region where the flow reattaches at the ribbed walls. Along the trailing surface the highest heat transfer in the vicinity of the reattachment region increases as rotation is increased from Ro = 0.18 to Ro = 0.67. As rotation increases the destabilization effects of the shear layer combined with the cross-stream effects generated by the Coriolis forces result in an increase in the heat transfer at the trailing surface.

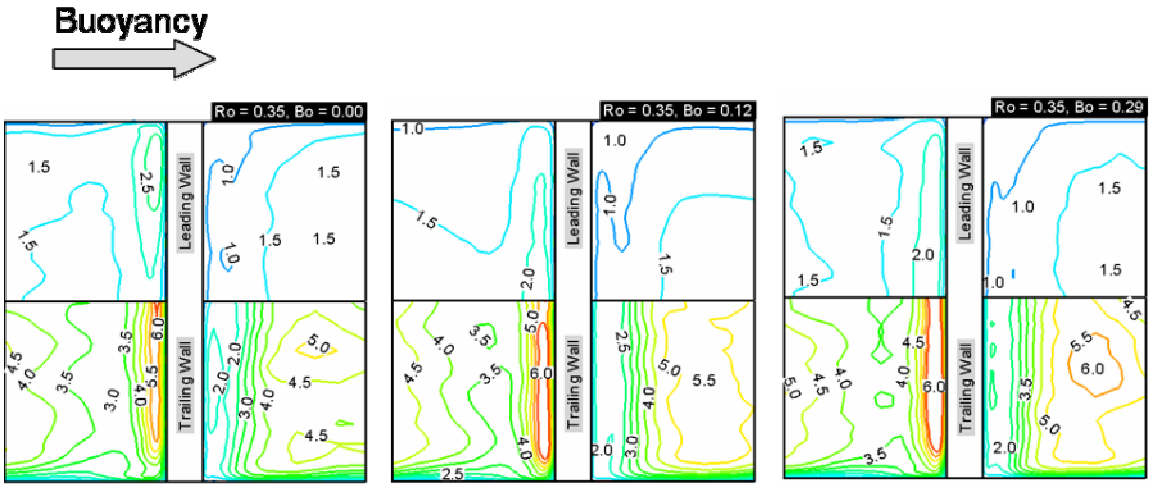

Figure 49: Heat transfer distribution at the ribbed walls for varying buoyancy numbers for a constant Ro = 0.35.

At the leading surface the maximum heat transfer in the inter-rib region is almost a constant value of around 1.5 – 2.0 times the heat transfer in a smooth duct. The longer reattachment length due to the stabilizing effects of rotation decreases the effective heat transfer area (between the reattachment point and the separation point upstream of the

next rib) and thereby hinders the turbulent transport at the leading surface. This feature is consistent with the behavior observed by Wagner *et al.,* (1992).

The effect of buoyancy for a constant rotation of Ro = 0.35 is shown in Figure 49. It is observed that as the buoyancy increases from Bo = 0.00 to Bo = 0.29, the heat transfer augmentation in the vicinity of the reattachment region increases from a value of 4.5 to around 6.0. The reattachment point at the trailing surface does not vary much as the rotation is increased and so the region of high heat transfer is observed to be at a distance of around $3.0D_h$ from the ribs at the trailing surface. The variation in the heat transfer is directly correlated to the variation in the TKE values. Higher TKE (more destabilization) at the trailing surface results in high heat transfer and so as buoyancy increases the heat transfer also increases.

Minimal differences are observed in the heat transfer at the leading surface. The effect of buoyancy is in the direction opposite to the main stream velocity. So as the buoyancy is increased the stabilizing effect at the leading surface increases resulting in lower and relatively constant heat transfer augmentation.

While the heat transfer at the ribbed walls is observed to be affected by both rotation and buoyancy, the heat transfer distribution at the side wall is less sensitive to rotation and buoyancy. This feature predicted by DES is in agreement with the observations of Wagner *et al.,* (1992) who observed small changes in the heat transfer at the outer and inner walls of the first pass of their internal cooling duct. Similar trends were also observed by LES (Abdel-Wahab and Tafti, 2004).

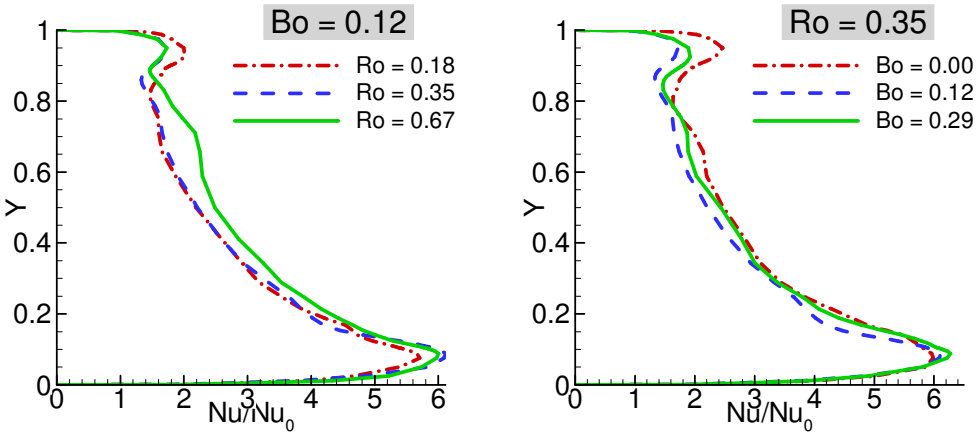

Figure 50: Effect of the variation of rotation and buoyancy on the heat transfer at the side walls, plotted at a distance of 0.5*e* upstream of the ribs.

Figure 50 shows the comparison of the heat transfer profiles at the side wall, slightly upstream of the rib. For a constant buoyancy number of 0.12 it is observed that as the rotation rate increases, the peak heat transfer augmentation at the trailing side increases form a value of around 5.5 for Ro = 0.18 in the vicinity of the ribs to a value of around 6.0 for Ro = 0.67. At the leading side the peak heat transfer decreases from a value of around 2.3 (Ro = 0.18) to a value of around 1.8 (Ro = 0.67) in the vicinity of the ribs.

For a constant rotation rate of 0.35, as the buoyancy is increased it is observed that the peak heat transfer augmentation at the trailing wall almost remains constant at a value of around 6.0. In the vicinity of the leading wall the peak heat transfer decreases from a value of around 2.5 for Bo = 0.00 to a value of around 2.0 for Bo = 0.29. The heat transfer at the center of the side wall is not very different for the three cases studied. Very small differences are observed in the secondary flow features, especially the lateral velocities, as buoyancy is varied and hence there is little difference in the side wall heat transfer at the center of the duct.

Figure 51 shows the comparison of the heat transfer predicted by DES at the ribbed walls and the side walls for a Ro = 0.35 and Bo = 0.29 with LES. Heat transfer profiles at both the leading and trailing walls show good agreement with the LES predictions. The region of high heat transfer upstream of the ribs predicted by DES is observed to be larger at both the ribbed surfaces. The heat transfer at the ribbed walls is influenced by the primary flow features and the turbulence in the vicinity of the ribbed walls. Since DES captures the primary flow features and the turbulence in this region accurately the heat transfer augmentation predicted by DES is consistent with LES.

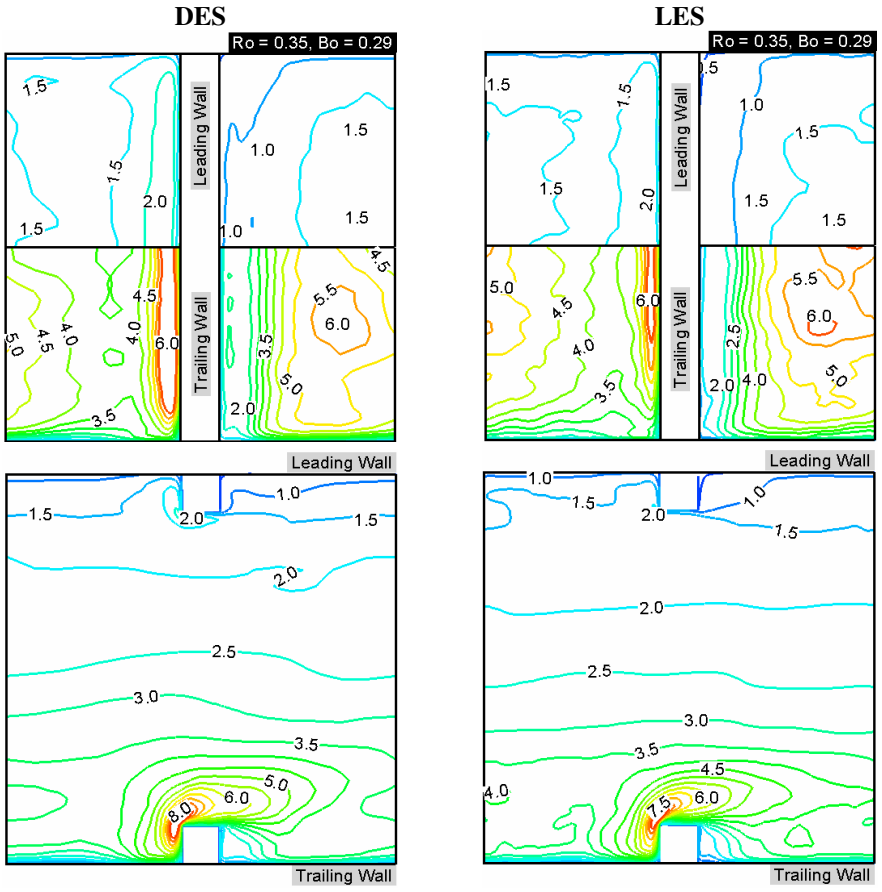

Figure 51: Comparison of the ribbed (Top) and side wall (Bottom) heat transfer predicted by DES and LES for Ro = 0.35 and Bo = 0.29

At the side walls the heat transfer augmentation is observed to decrease from a value of around 8.0 in the vicinity of the rib at the trailing surface to a value of around 1.5 – 2.0 at the rib at the leading surface. The heat transfer contours, which are dictated by the secondary flow, are also predicted accurately by DES.

Figure 52 shows the surface averaged heat transfer at the trailing and leading side walls. The heat transfer augmentation obtained using DES is compared with predictions by LES (Abdel-Wahab and Tafti, 2004) and experimental results by Wagner *et al*., (1992) for the different buoyancy cases. For the lower buoyancy case (Bo = 0.12) it is observed that the heat transfer augmentation predicted at the trailing and leading side wall compares well with the experimental measurements as well as the LES computations. The heat transfer augmentation at the trailing wall is observed to increase from a value of around 3.5 to a value of around 4.1 as the rotation is increased from Ro = 0.18 to Ro = 0.67. At the leading wall the heat transfer augmentation decreases from a value of around 1.6 to a value of 1.1. For the highest buoyancy case (Bo = 0.29) the heat transfer augmentation at the leading and trailing surfaces differ from the values predicted by LES by a factor of 15%. However a comparison with the experimental measurements of Wagner *et al.,* (1992) shows good agreement.

The variation of the overall heat transfer augmentation at the trailing and leading walls with rotation and buoyancy are shown in Table 8. It is observed that the overall heat transfer at the trailing wall is significantly altered due to the effect of rotation. Though buoyancy was observed to increase the peak heat transfer at the trailing wall, the overall heat transfer augmentation is affected only for the lowest rotation case. The overall heat

transfer augmentation at the leading surface decreases with rotation. However, very little difference is observed with the variation of buoyancy.

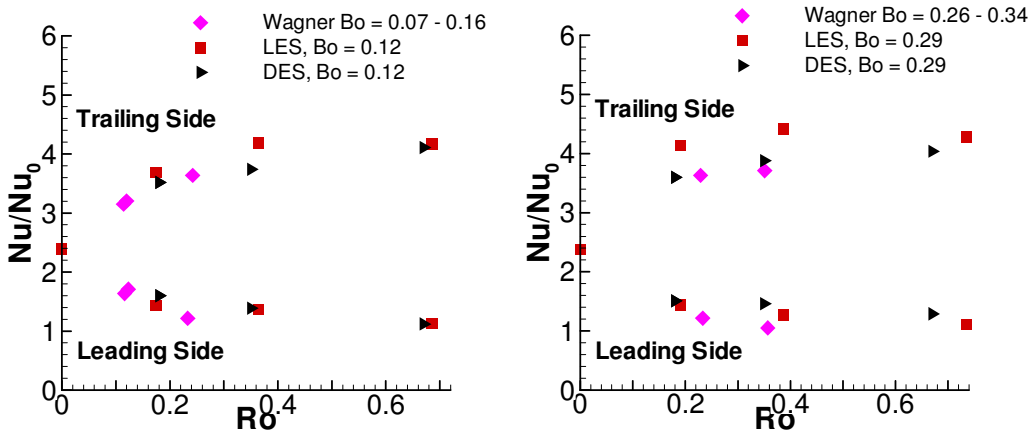

Figure 52: Comparison of the surface averaged ribbed wall heat transfer augmentation

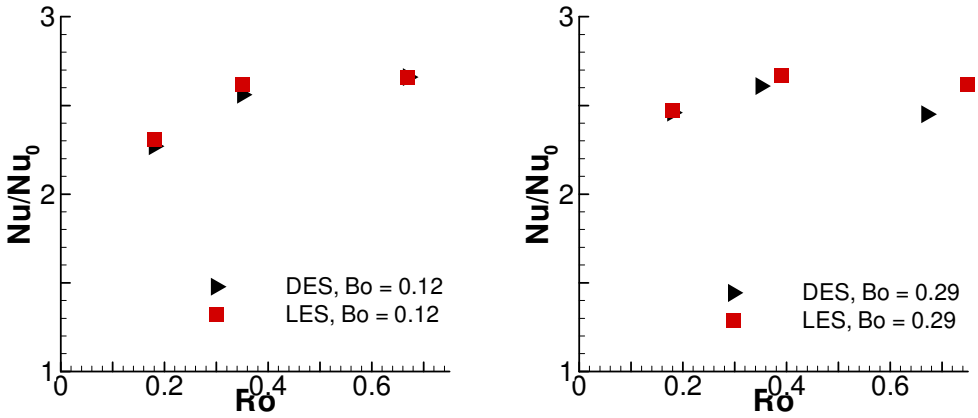

Figure 53: Comparison of the side wall heat transfer augmentations

Figure 53 shows the comparison of the side wall heat transfer as predicted by DES in comparison with the heat transfer reported by LES studies (Abdel-Wahab *et al.,* 2004). The side wall heat transfer augmentation predicted by DES compares well with LES. It is observed that the surface averaged heat transfer augmentation increases as the rotation is increased from 0.18 to 0.35, but remains constant as the rotation is further increased to Ro = 0.67. A slight difference is observed in the side wall heat transfer for the Ro = 0.67

and Bo = 0.29 between DES and LES. However the value predicted by DES, is within 7.5% of the value predicted by LES.

Table 8: Variation of the heat transfer augmentation at the ribbed and side walls for different rotation and buoyancy cases

Ro	0.18			0.35			0.67		
Bo	**0.00**	**0.12**	**0.29**	**0.00**	**0.12**	**0.29**	**0.00**	**0.12**	**0.29**
Re	18990	18040	17950	17080	17340	17660	20040	20520	20360
Trailing	3.05	3.52	3.60	3.79	3.74	3.88	4.05	4.11	4.04
Leading	1.41	1.60	1.51	1.54	1.39	1.46	1.32	1.12	1.29
Side Wall	2.28	2.27	2.46	2.22	2.56	2.61	2.60	2.66	2.45

Table 8 shows the variation of the heat transfer augmentation at the side walls with rotation and buoyancy. It is observed that the variation in the side wall heat transfer is not affected much by buoyancy. Rotation also results in a smaller change in the heat transfer as compared to the trailing wall. This behavior is in agreement with the trends observed by Wagner *et al.,* (1992).

5.5.5 Summary and Conclusions

Earlier studies have shown the deficiencies of the popular RANS models in accurately predicting the effects of buoyancy in ribbed ducts as well as in several other applications like cavity flows, atmospheric flows etc. Addition of *ad hoc* terms have also proposed, but these terms have often failed to work in flows outside the flow regime for which it was proposed. The application of DES based on an eddy-viscosity RANS model improves the prediction capabilities considerably as no additional terms are necessary to

model the effects of buoyancy. The present study validates the capability of DES in predicting the flow and heat transfer in internal cooling passages when subjected to rotation and the effects of buoyancy are significant. Earlier LES studies (Abdel-Wahab and Tafti, 2004) have been used for detailed comparisons of the flow and heat transfer physics, while the surface averaged heat transfer augmentation are validated with the experimental measurements by Wagner *et al.,* (1992).

The comparison of the mean flow features shows that the flow stabilizes at the leading surface as a result of which reattachment length of the flow increases as the buoyancy is increased. Destabilization of the flow at the trailing surface results in a shorted reattachment length. The opposite effect is observed at the leading surface. Buoyancy also results in an increase in the turbulence at the trailing surface and decreases at the leading surface. Heat transfer increases with buoyancy at the trailing surface. At the leading surface the effective heat transfer area is decreased as the recirculation zone occupies a large portion of the inter-rib space. Smaller changes are observed in the heat transfer at the side walls.

A comparison of the detailed flow physics with LES shows that DES predicts the primary and the secondary flow features in the duct accurately. Apart from predicting the flow features, the augmentation and attenuation of turbulence is predicted as accurately as an equivalent LES computation. Heat transfer distributions at the ribbed and side walls, being functions of the mean and turbulent flow features are predicted well by DES. The trends observed in the heat transfer augmentations at the ribbed and side walls are also consistent with the experimental observations by Wagner *et al.,* (1991). The overall heat transfer augmentations predicted by DES compares well with LES and experiments.

In summary, it is observed that DES accurately predicts the physics of the flow dominated by shear and buoyancy. The main contribution is in establishing the capability of DES in predicting the effects of the extra strain generated by buoyancy. It is observed that DES computations can be carried out at reasonable costs, almost an order of magnitude less than the equivalent LES computation.

6 Flow and Heat Transfer in a complete Two Pass Duct connected by a 180º Bend

The previous chapter validates the performance of DES in predicting the flow and heat transfer in the fully-developed regions of the ribbed duct. The following study builds on the studies on fully-developed ducts and focuses on the validation of DES in two-pass ducts. In the process the capabilities of DES in predicting the development of the flow and heat transfer in the first pass of the duct till it attains a fully developed state, the effects of the bend in the two-pass duct and the flow and heat transfer downstream of the bend are studied. The initial part of the study investigates the application of DES in a stationary two-pass duct. This is followed by an investigation of the effects of rotation in the two-pass duct.

The flow and heat transfer in a ribbed internal cooling duct is a function of the flow Reynolds number and the geometric parameters such as the rib height to hydraulic diameter ratio, the rib pitch, the aspect ratio of the duct, the angle of the rib with respect to the flow and the shape of the rib as shown by previous studies (eg. Johnson *et al.,* 1994). Additionally, when rotation is introduced, the Coriolis forces significantly alter the primary and secondary flow features of the flow. The Coriolis forces therefore affect the heat transfer at the ribbed walls in both the first and the second passes of the cooling duct.

Computations are carried out for a ribbed square channel with a rib pitch to rib height (P/e) of 10 and rib height to hydraulic diameter (e/D_h) of 0.1 for a bulk Reynolds number of 20,000. Each rib section (block) consists of two in-line ribs placed at the center of the channel at the top and the bottom walls. The ribs are placed normal to the flow direction

and have a square cross-section. Since DES is less expensive than LES, a complete analysis of a two pass channel with 12 sets of ribs in the first and the second pass has been carried out. The two passes are connected by a 180º bend whose width (W) is half the hydraulic diameter (W/D_h = 0.5). The geometry used for the computation is shown in Figure 54.

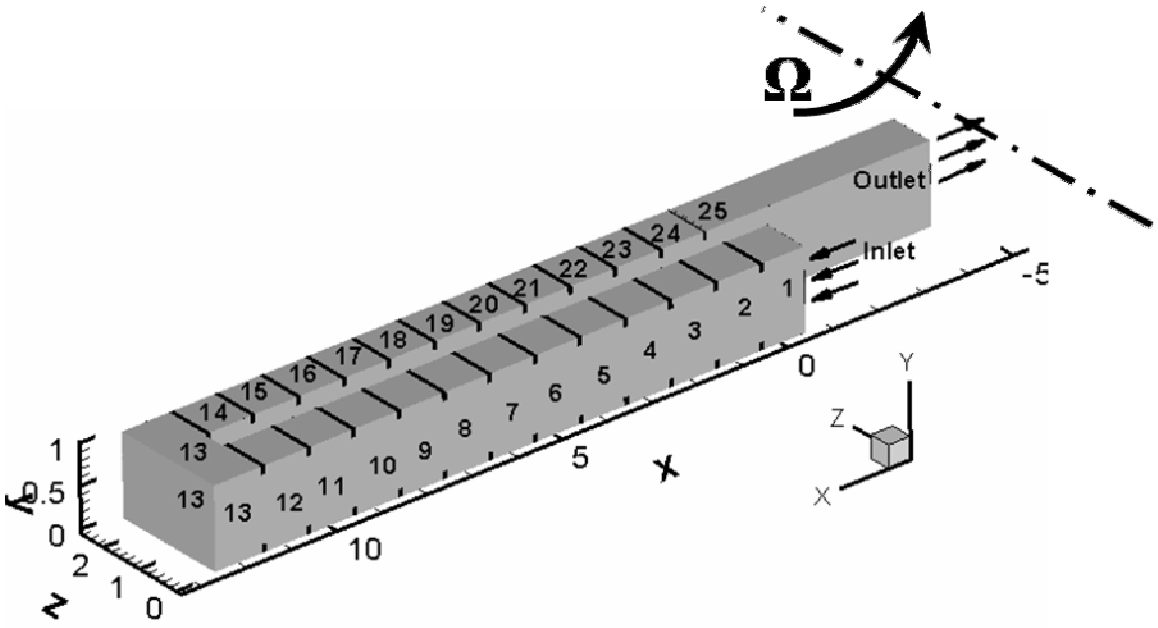

Figure 54: The two-pass internal cooling duct geometry studied

A no-slip boundary condition is imposed on the walls and the ribs. The conditions set at the wall are $\vec{u} = 0$, k = 0, and $\omega \to 6/\mathrm{Re}_\tau\, \beta_1 y^2$ as $y \to 0$, which is derived from a molecular diffusion and dissipation balance on smooth surfaces (Wilcox, 1988). The turbulent Prandtl number is assumed to have a constant value of 0.9. A uniform laminar inlet condition is imposed to approximate the flow exiting a plenum into the inlet section of the duct. At the outflow, a convective condition of the form $\frac{\partial \phi}{\partial t} + c\frac{\partial \phi}{\partial x} = 0$ is applied,

where c is the mean convective velocity and ϕ is the variable being convected out ($\phi = \bar{u}$, θ, k and ω).

The grid in a rib pitch consists of 65 nodes in the streamwise direction and 65 x 65 in the cross-stream direction. The grid used for one pitch has been tested and found to be optimal for DES (fully-developed) computations on stationary and rotating ducts (Chapter 2.3). In total, each unit was discretized into 64 x 64 x 64 cells and was divided into 4 equal blocks in the spanwise direction to facilitate parallel processing. The 180º bend was discretized into 64 x 64 x 32 cells and divided into two blocks. The second leg of the duct had an outlet region which was around 4 hydraulic diameters long. All these sum to 7.7 x 10^6 cells which are distributed in 110 blocks.

A non-dimensional time step (non-dimensionalized based on the bulk velocity and the hydraulic diameter of the duct) of 1 x 10^{-4} was used in all of the cases. Calculations are initiated by assuming a uniform flow velocity in the computational domain and imposing a uniform laminar flow inlet profile, approximating the flow exiting a plenum into the ribbed channel. Time evolution of bulk quantities such as surface-averaged Nusselt numbers and friction factors are monitored as the solution is allowed to reach a statistically steady state for about 30 non-dimensional time units. The mean characteristics of the flow are obtained by averaging the solution for an additional 10 time units.

6.1 Stationary Two-Pass Duct

In the current study, DES and URANS are carried out in a complete two-pass channel with 12 ribs in the first and second passes, connected by a 180 degree bend. The flow in

the first pass of the duct is compared with LES computations by Sewall *et al.* (2006a). The flow in the fully developed region is also compared with experiments by Rau *et al.* (1998). The flow in the 180 degree bend is compared with LES results in the bend by Sewall and Tafti (2006b) and experimental results by Sewall *et al.* (2006a). The LES computations have been validated extensively with experiments in Sewall *et al*. (2006a), and except for some differences at the center of the duct and in the 180 degree bend, all physical phenomena characterized by mean and turbulent rms quantities are reproduced with excellent quantitative accuracy.

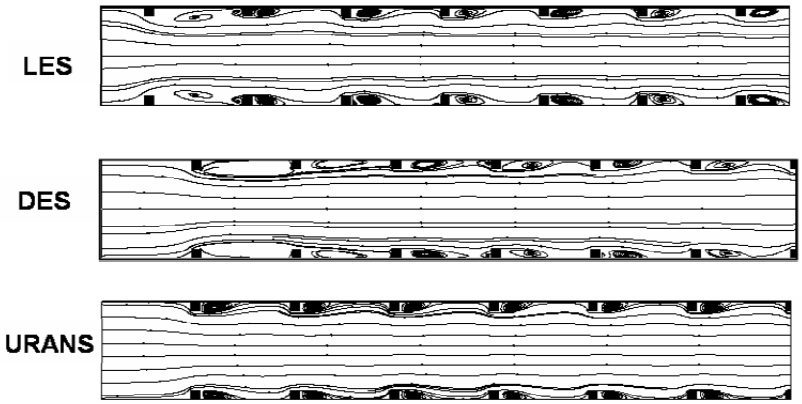

Figure 55: Comparison of streamlines in the developing region through a plane passing through the center z-plane

6.1.1 Mean Flow Field

6.1.1.1 Streamwise Flow Development in First Pass

Figure 55 shows the development of the flow. The LES calculation (Sewall *et al*, 2006a) shows that the separated shear layer at the first set of ribs immediately transitions to turbulence. The separation zone behind the first rib extends the whole pitch and reattaches just upstream of the second set of ribs. However, at the second rib, because of the increased mixing promoted by turbulence, the separated zone extends only half the rib

pitch, after which the flow structure quickly settles down to a near fully-developed state, with small changes occurring in the flow structure and turbulent characteristics. The flow quantities change in magnitude further downstream and a "near-fully-developed" state is established by the third to fourth rib. A comparison of the streamlines injected at the inlet shows that DES predicts that the flow separating after the first rib reattaches in the inter-rib region after passing the second rib. At the first three ribs, the separation zones are much larger than in LES which implies that DES is unable to predict the rapid transition to a turbulent state. In the URANS case the first rib trips the flow and the flow transitions immediately after the first rib. The flow reattaches between the first and the second ribs and immediately settles down to a fully turbulent flow. This can be clearly identified in Figure 55.

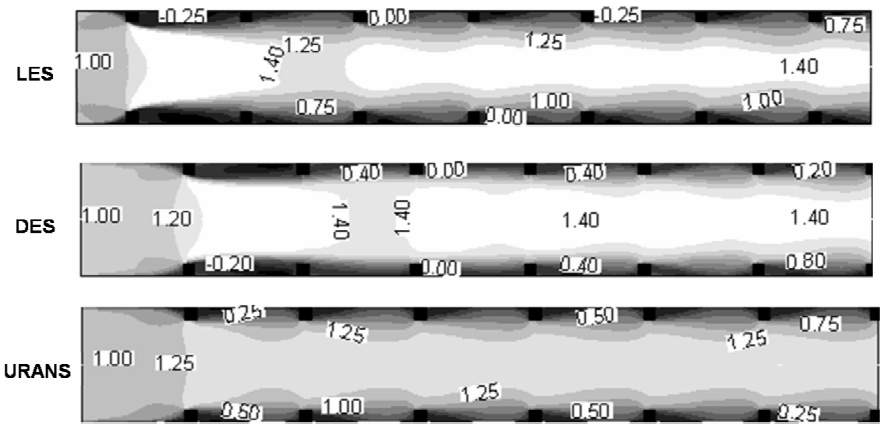

Figure 56: Comparison of u-velocities in the developing region through the center z-plane

A comparison of the streamwise velocity contours (Figure 56) shows that the DES results are slightly different than that predicted by LES for the first three to four rib pairs. The streamwise velocity distribution in the cross-section is less "plug-like", but shows a gradual increasing trend towards the center of the duct. Though differences are observed in the reattachment lengths between the DES and LES predictions, the centerline

velocities predicted by LES and DES reach a constant value of 1.4 times the bulk velocity after the first three ribs. The flow predicted by the URANS shows the immediate transition of the flow as it passes the first rib and attains a flat turbulent profile downstream. The magnitudes of the center line velocities observed in the URANS case is less than the velocity magnitudes observed in LES and DES.

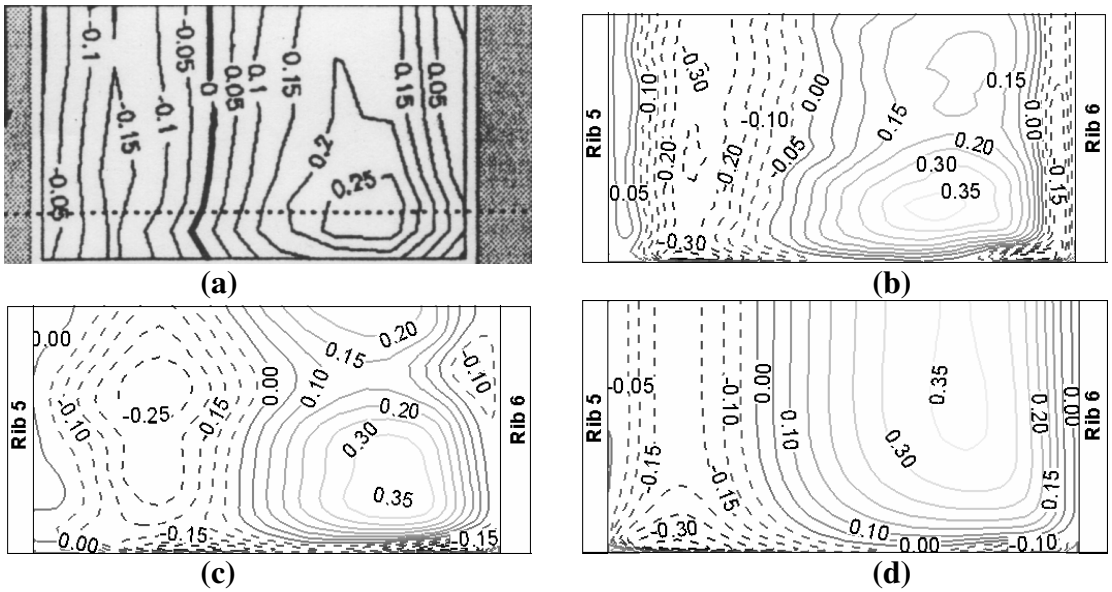

Figure 57: U-velocities at a plane passing through the rib (a) Experiments Rau *et al.,* (1998), P/e = 9 (b) LES – Fully Developed Region (Rib 6) (c) DES – Fully Developed Region (Rib 6) (d) URANS – Fully Developed Region (Rib 6)

Figure 57 compares the flow features in the vicinity of the rib 6 (where the flow is fully developed) predicted by DES and URANS with the flow predicted by LES (Sewall et al., 2006a) and experiments (Rau *et al.,* 1998). For P/e = 9, at a plane passing through y/e = 0.15, Rau *et al.,* (1998) observed the maximum velocity to lie at a distance of around $0.15D_h$ from the wall in the fully developed region. Though some differences in magnitude of the velocities are observed due to the different rib pitch in the experiments, LES and DES predict this feature in the fully developed region of the first pass of the

duct. URANS fails to predict this offset and predicts a uniform high velocity region spanning the channel.

Figure 58 shows the streamwise velocities measured at a plane passing through the center at the *y/e* = 0.1 plane. The separated region behind the rib experiences a reverse flow, which is evident from the negative velocities behind the rib up to the reattachment region. The flow accelerates after reattachment and separates in front of the next rib as shown by the small negative velocities upstream of the rib (x = 5.35). The separation in front of the rib is predicted accurately by DES, and the velocity magnitudes are consistent with the fully developed experimental data. URANS predicts early attachment of the flow and also fails to predict the recirculation regions immediately upstream and downstream of the rib.

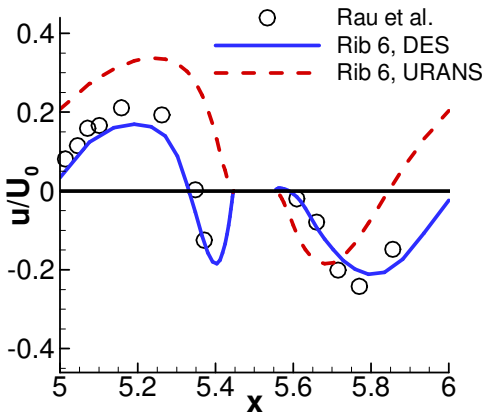

Figure 58: Comparison of the streamwise velocities at *y/e* = 0.1 with experimental data.

6.1.1.2 Development of Secondary Flows

Secondary flows in the duct cross-section have a large effect on heat transfer augmentation on the smooth walls. Unlike skewed or angled ribs, which exhibit strong secondary flow patterns, normal rib induced secondary flows are comparatively weak but

highly localized and strong near the junction of the rib with the side walls. The vortex shedding at the junction induces strong spanwise velocities in the vicinity of the smooth wall. This feature is difficult to predict by standard eddy-viscosity RANS models (Ooi *et al.,* 2002, Chapter 5.3.1).

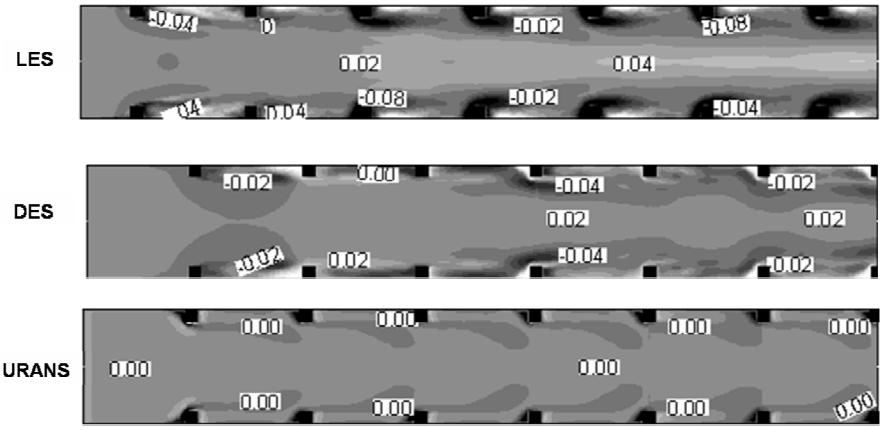

Figure 59: Comparison of w-velocities in the developing region through a plane near the side wall

Figure 59 shows the development of the spanwise velocity contours at a plane near the side wall (z/D_h = 0.05). LES predicts the establishment of this feature by the third rib pair, whereas DES predicts it only after the fourth rib pair, however after it is established, the magnitudes are consistent between the two methods. URANS, as in the earlier computations, fails to predict the secondary flow accurately. The *w*-velocities predicted by URANS are of an order of magnitude less than that predicted by DES and LES.

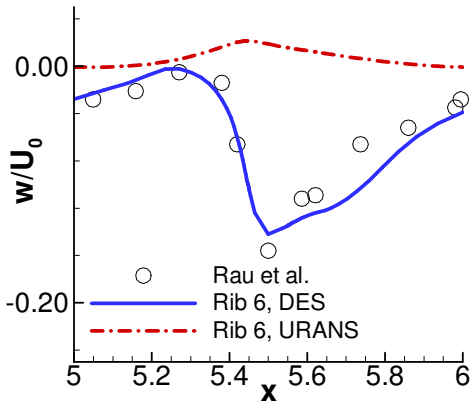

Figure 60: Secondary flow in the duct measured at y/e = 1.5 and z/D_h = 0.45

The lateral w-velocities measured above the rib along a line close to the smooth side wall (y/e = 1.5, z/D_h = 0.45), also shows very good agreement of the secondary flow predicted by DES in the vicinity of rib 6 with the fully developed experimental results. It is observed that there is little spanwise movement of the fluid in the region after reattachment while in the vicinity of the ribs (x = 5.4 – 5.6) a strong secondary velocity is observed. The k-ω model when used in the URANS mode calculates a near zero spanwise velocity at these locations.

6.1.1.3 Heat Transfer in the First Pass

Figure 61 shows the heat transfer at the side and the ribbed walls as predicted by LES (Sewall *et al.*, 2006a). The secondary flows in the duct cross-section play an important role in the side wall heat transfer. In the vicinity of the rib the secondary flow impinging on the side walls results in high heat transfer and the heat transfer increases up to 3.5 times that in a smooth duct. On moving towards the center of the side walls the heat transfer is observed to be close to the values obtained in a smooth channel.

At the ribbed walls the heat transfer augmentation on an average is observed to be close to 2.5 in most of the regions. Heat transfer as high as 3.0-3.5 is observed immediately upstream of the ribs, caused by the unsteady vorticies. Immediately downstream of the rib low heat transfer is observed. The heat transfer is observed to reach a quasi periodic state by the 4th rib. The above observations from the LES computation are used to compare the heat transfer predicted by DES and URANS. The initial development of heat transfer as predicted by DES is slower than the LES computations. However by the 4th rib the heat transfer is observed to be fully developed. The heat transfer predictions are consistent with LES, but slightly higher levels of heat transfer are observed upstream of the ribs and in the shear layer near the smooth side wall. URANS predicts the heat transfer at the ribbed and the smooth wall reasonably well. However the failure to accurately predict the secondary flows results in low levels of heat transfer augmentations in the vicinity of the rib at the side walls.

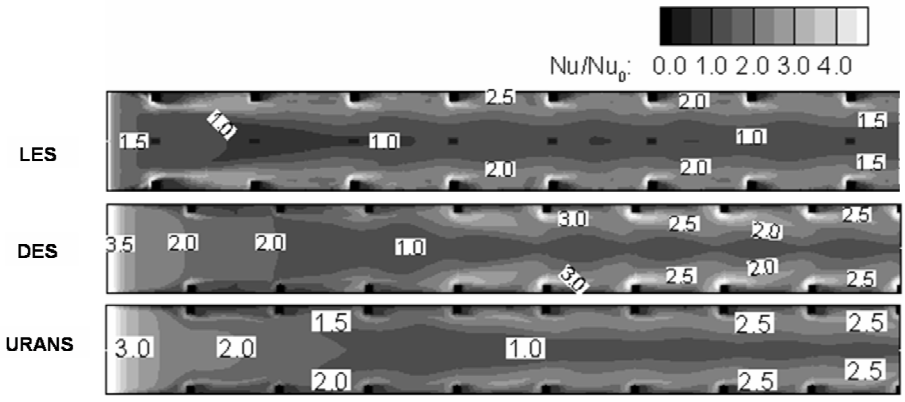

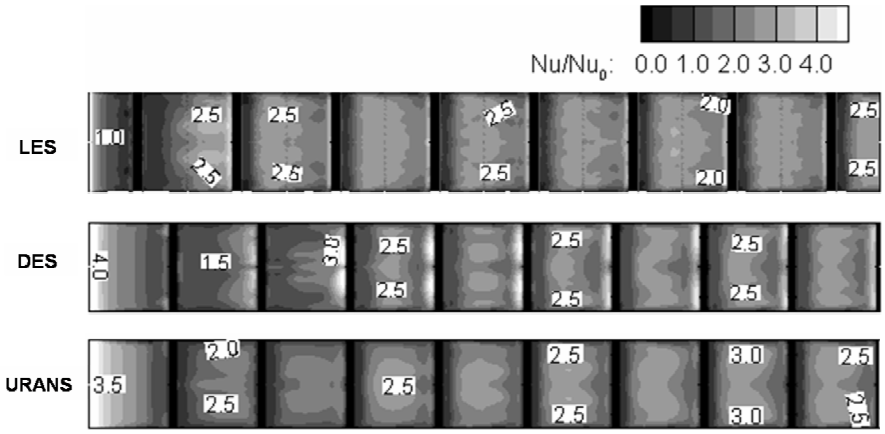

Figure 61: Heat transfer augmentation in the first pass of the two-pass duct at the side wall (Top) and Ribbed Wall (Bottom)

The heat transfer predictions by DES and URANS near the 6th rib, where the flow is fully developed are compared with the heat transfer predicted by LES (Sewall *et al*, 2006a) and observed by experiments (Rau *et al.,* 1998) (Figure 62). The heat transfer contours obtained from the experiments for *P/e* = 9, show that the heat transfer is the maximum in the vicinity of the rib which is due to the impingement of the localized strong secondary flow. Heat transfer decreases on moving away from the ribs. LES predicts similar trends with the heat transfer augmentation reaching a maximum value of 4.5 in the vicinity of the rib. DES slightly over-predicts the heat transfer in the shear layer above the rib. The heat transfer distribution towards the center of the channel is consistent with the earlier observations. URANS also predicts the variation reasonably well. URANS however underpredicts the heat transfer in the shear layer of the rib as compared to LES and DES.

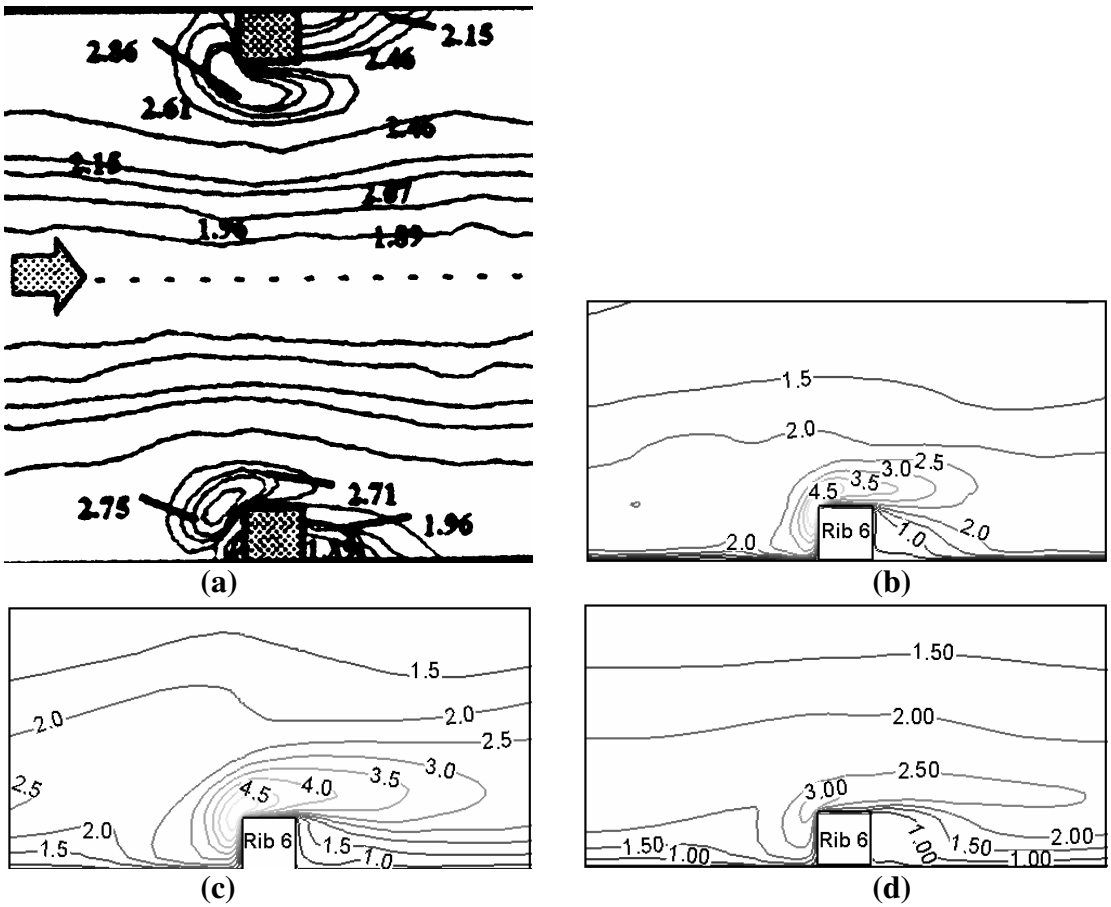

Figure 62: Side wall heat transfer (a) Experiments Rau *et al.,* (1998) *P/e* = 9 (b) LES – Fully Developed Region (Rib 6) (c) DES –Fully Developed Case (Rib 6) (d) URANS – Fully Developed Region (Rib 6). (b), (c) and (d) show the heat transfer from the lower rib to the center of the duct side wall

Figure 63 shows the comparisons of the heat transfer augmentation at the side walls of the first pass immediately upstream ($0.05D_h$ upstream) of the 6th rib with the experiments. The heat transfer is highest in the region of secondary flow impingement and decreases towards the center of the duct. DES predicts the trends in the heat transfer reasonably well. URANS underpredicts the heat transfer in the shear layer as compared to the experiments. On moving towards the center of the channel the heat transfer decreases and both DES and URANS predictions are in good agreement with the experiments.

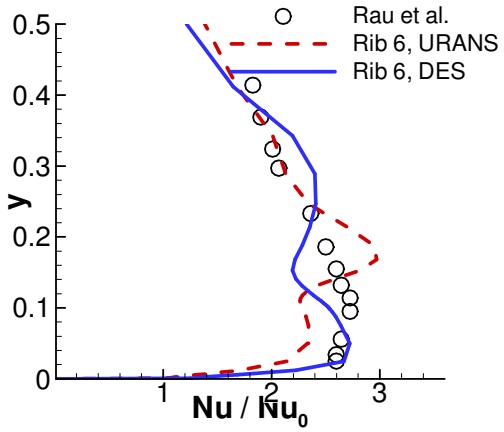

Figure 63: Comparison of side wall heat transfer with the experimental observations.

The heat transfer augmentation at the ribbed wall in the hydrodynamically and thermally fully developed regions as predicted by DES and URANS is shown in Figure 64. These are compared with the heat transfer augmentation contours observed for *P/e* = 12 by Rau *et al.,* (1998) and LES computations (Sewall *et al.*, 2006a). A region of low heat transfer immediately downstream of the rib is predicted, which is caused by the presence of secondary trapped eddies. Further downstream in the primary recirculation region, the heat transfer from the walls is gradually enhanced and reaches a maximum at around 3.5e downstream of the rib. The point of maximum heat transfer is slightly upstream of the reattachment, where the surface shear is a maximum. The general trends indicate that DES is accurate in predicting the heat transfer augmentation in the recirculation region. However, DES tends to predict an exaggerated region of high heat transfer in front of the rib. URANS showed reasonable agreement unlike the fully developed RANS computations (Chapter 5.3.1). Upstream of the rib the heat transfer is under-predicted by URANS.

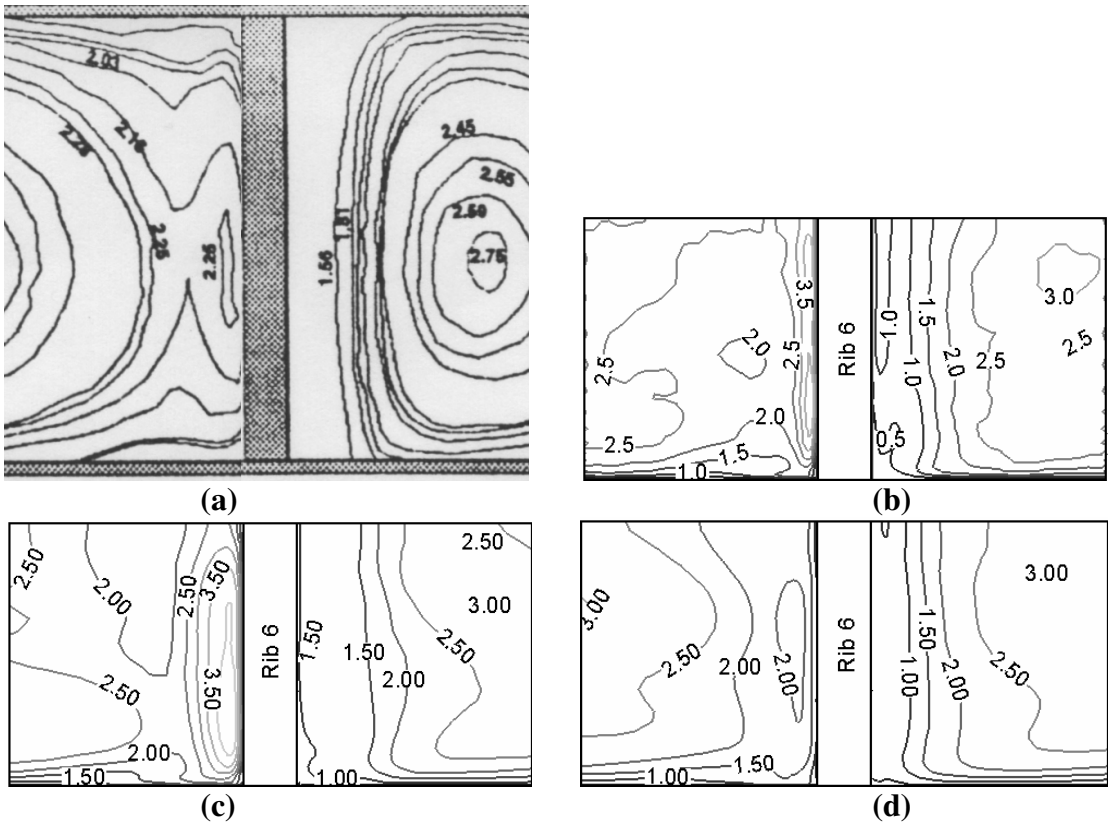

Figure 64: Ribbed wall heat transfer (a) Experiments Rau *et al.,* (1998) P/e = 12 (b) LES – Fully Developed Region (Rib 6) (c) DES –Fully Developed Case (Rib 6) (d) URANS – Fully Developed Region (Rib 6). Only half of the ribbed wall is shown in (b), (c) and (d).

A comparison of the centerline heat transfer at the ribbed wall with the experiments is shown in Figure 65. Both DES and URANS show reasonable agreement with the experimental data. DES underpredicts and URANS overpredicts the heat transfer in the center of the inter-rib region. A closer look at the heat transfer distribution predicted by DES (Figure 61) shows that the higher levels of heat transfer ($Nu/Nu_0 > 2.50$) are offset from the center of the duct. At these locations the heat transfer is comparable to the levels measured by the experiments. Apart from overpredicting the heat transfer downstream of the rib, URANS also fails to capture the high heat transfer in front of the ribs and the

region of local high heat transfer behind the ribs occurring due to the presence of the secondary recirculation.

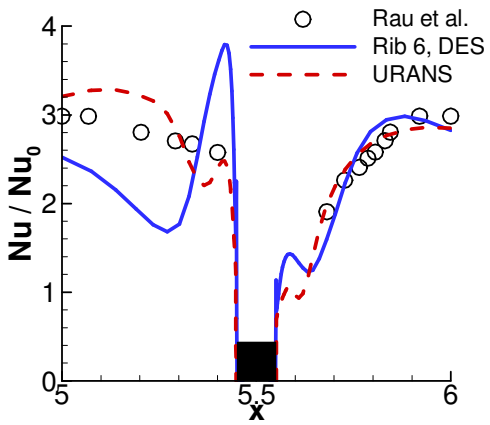

Figure 65: Comparison of ribbed wall heat transfer with the experimental measurements.

6.1.1.4 Flow Features in the180 degree Bend and Second Pass

Figure 66 shows streamlines at three cross-stream locations y = 0.5, 0.3 and 0.15 for the flow entering and exiting the 180 degree bend as predicted by DES and URANS. As the flow approaches the bend, it accelerates at the inside of the bend and separates at the sharp edge of the bend. The separated region occupies the central 25-40% of the duct height and its shape and extent are predicted well by DES. DES predicts a recirculating region which does not quite sustain itself throughout the height of the duct. Further, the flow is characterized by impingement on the back wall and outer downstream wall of the duct which coincide with regions of high heat transfer. LES computations (Sewall and Tafti, 2005) showed similar recirculation regions at the inner wall and the outer corners of the bend. URANS on the other hand does not show any separation downstream of the bend or at the inner wall of the bend. URANS also fails to predict the recirculation at the

outer walls of the bend. However URANS predicts a slight separation downstream of the bend on moving down the height of the duct.

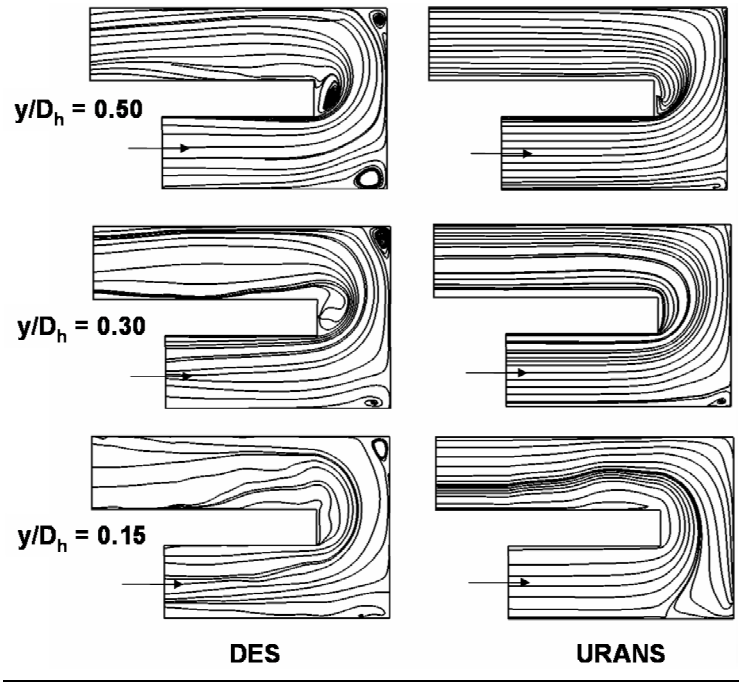

Figure 66: Comparison of the flow predicted by DES and URANS in the 180 degree bend.

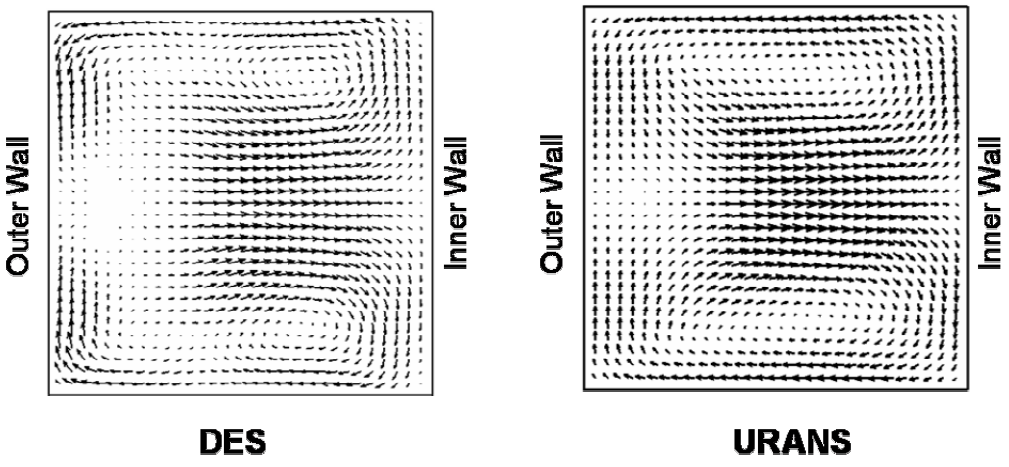

Figure 67: Secondary flow at the center of the 180 degree bend.

Figure 67 shows the secondary flow in the center of the bend as predicted by DES and URANS. DES predicts Dean vortices in the vicinity of the inner and the outer walls.

These vortices are responsible for higher levels of heat transfer at the inner and the outer walls of the bend. URANS also predicts one large secondary full cell in each half of the cross-section. It is observed from the length of the velocity vectors plotted that the secondary velocities predicted by URANS is more than that predicted by DES, especially in the core of the bend.

To verify the accuracy of the flow predicted by URANS and DES, the streamwise velocities computed at the center of the 180 degree bend at different locations are compared with LDV data from Sewall *et al*. (Figure 68). At all *y*-locations, the velocity in the outer part of the bend (x = 12.0 to 12.5) is quite uniform at approximately 1.5 times the bulk velocity. However, at the inside of the bend, the streamwise velocity steadily decreases as y increases with a reversal in the flow direction occurring between y=0.27 and y=0.37. The profile at y = 0.27 shows a velocity of nearly zero, indicating that the recirculation zone occupies about 25% of the height of the duct. It is observed that in all the locations DES predictions match well with experiments. DES comparisons are better than URANS at these locations. URANS fails to predict the recirculating cells in the 180 degree bend, as observed in the profiles at y = 0.37 and 0.44.

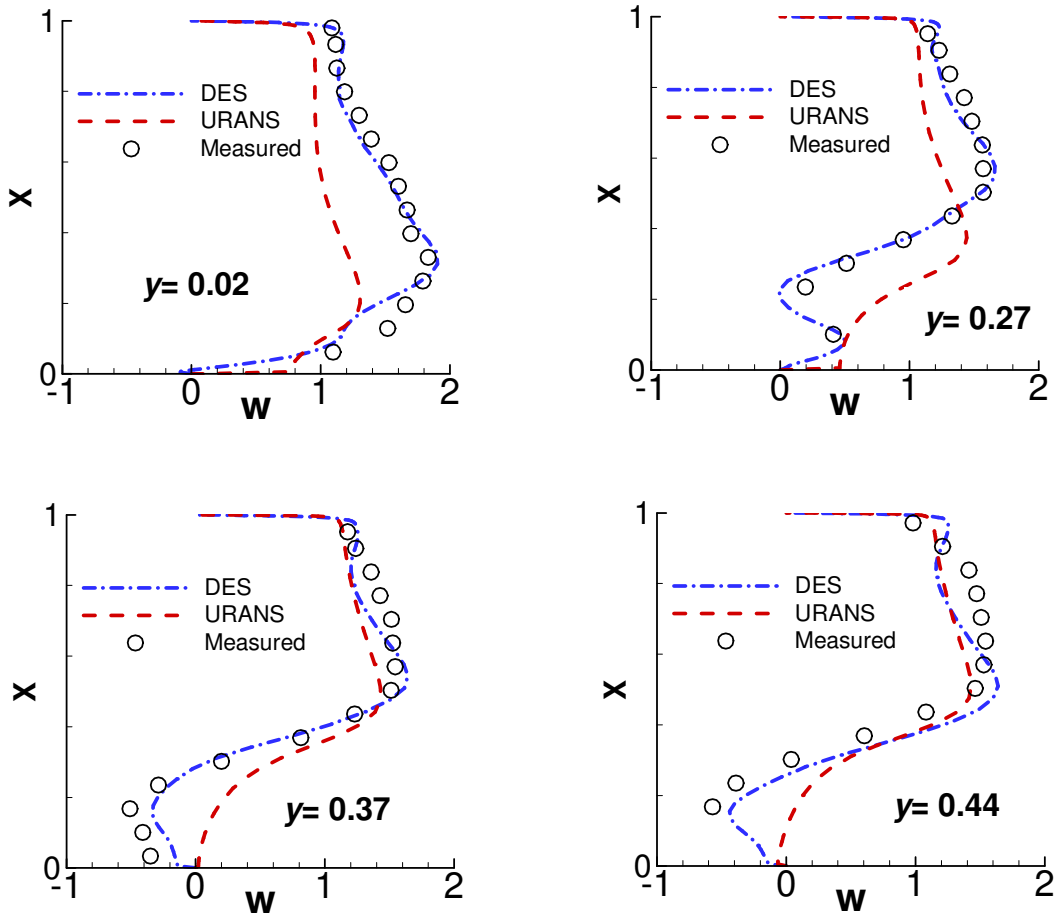

Figure 68: Velocities in the center of the 180° bend in comparison with experiments by Sewall *et al.*, (2006a).

6.1.1.5 Heat Transfer in the 180 degree Bend

Figure 69 shows the comparison of the heat transfer at the side and ribbed walls in the vicinity of the 180 degree bend. The predictions are compared to LES (Sewall and Tafti, 2006b) which was performed in a geometry similar to the one used in this study with slight differences in the flow conditions. The LES computation was initiated by introducing a fully developed time dependent turbulent flow at the inlet which is three hydraulic diameters upstream of the bend, while the DES and the URANS computations have been carried out on a whole two pass channel. Another difference is that the LES

computation assumed a uniform temperature distribution at the walls while the DES and URANS computations assume a uniform heat flux condition.

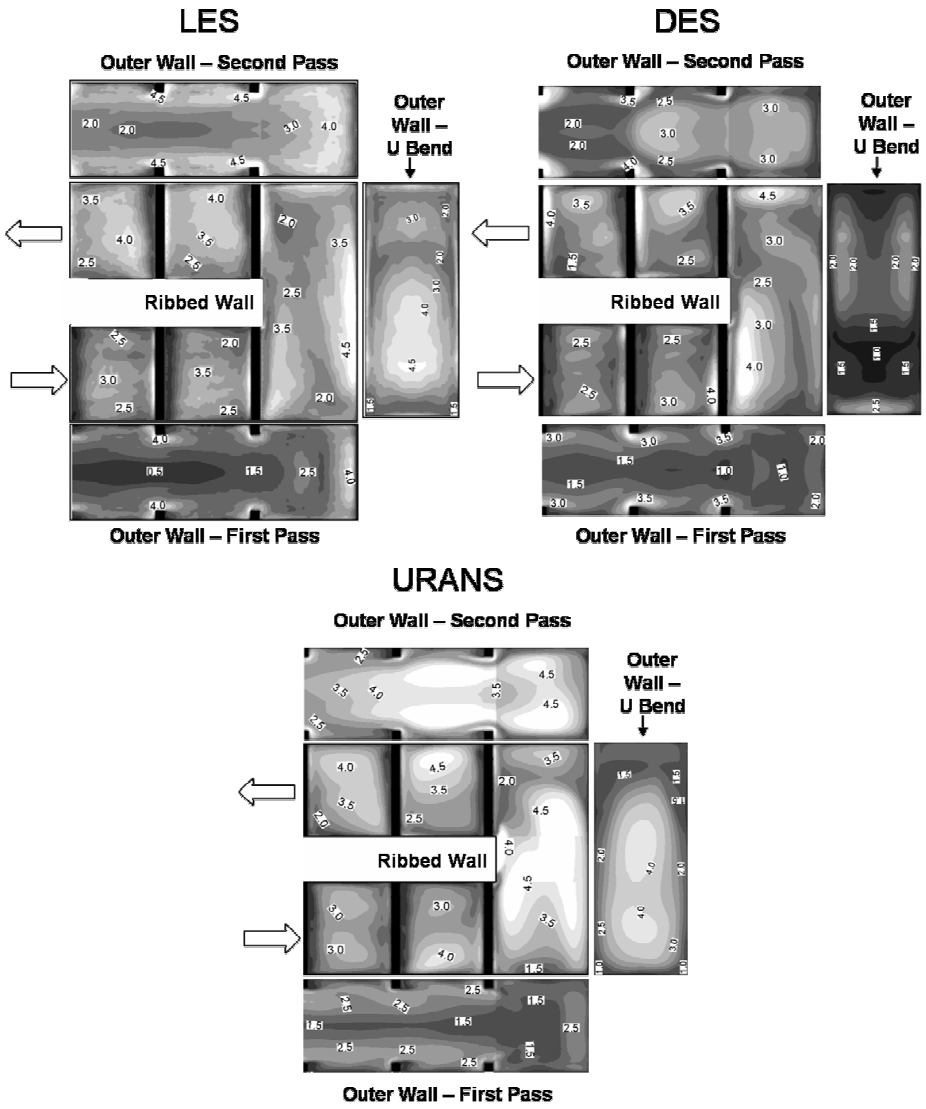

Figure 69: Heat Transfer augmentation at the ribbed wall and outer walls in the vicinity of the 180 degree bend. Flow direction indicated by arrows.

It is observed that while the heat transfer was observed to be near symmetric in the developing region of the first pass, there is a significant asymmetry in the heat transfer values as the flow approaches the bend. The heat transfer at the side walls is maximum in the vicinity of the ribs while it decreases to values close to that of a smooth channel towards the center of the side walls. The flow at the entrance of the bend is similar to the

flow around skewed ribs and so the region of high heat transfer is observed to widen as it enters the bend. In the bend Dean vortices increase the heat transfer both at the the outer wall. The skewness in heat transfer prevails in the second pass of the channel. Impingement of the flow on the outer walls caused high heat transfer as the flow turns into the bend from the first pass and into the second pass from the bend. The general heat transfer downstream of the 180 degree bend is higher than the heat transfer upstream. Similar observations were also made in earlier experimental studies by Ekkad *et al.,* (1997), where the heat transfer profiles at the center of the ribbed wall showed the effect of the bend on the heat transfer in the second pass.

Since the turbulence levels are predicted accurately at the ribbed walls, the heat transfer is predicted accurately by DES. A comparison of the results shows that while the heat transfer predicted by DES at the ribbed walls compares well with LES, the heat transfer is underpredicted at the outer wall in the bend and in the second pass. This underprediction may be attributed to the difference in the inlet conditions. LES computations model the bend separately with a turbulent inlet two ribs upstream of the bend, while DES models a developing flow from an inlet that is located 12 ribs upstream of the bend. So the effect of flow impingement on the heat transfer is lower as predicted by DES as compared to LES. URANS severely overpredicts the heat transfer in the bend and downstream in the second pass, both at the ribbed walls as well as the outer walls.

6.1.1.6 Pitch Averaged Frictional Losses

Figure 70 shows the comparison of the block averaged friction factor values obtained from DES and URANS with the LES computations (Sewall et al., 2006a, Sewall *et al.,* 2006a). The LES data has been collected from two cases: stationary developing flow

(Sewall et al., 2006a) for the first 9 ribs in the first pass, and LES computations in a 180 degree bend (Sewall *et al.,* 2006b), for the 180 degree bend and two ribs upstream and downstream of the bend. In the DES and URANS computations the data is obtained by using the average pressure drop across one pitch ($f = -\Delta p/2\Delta l$) across a rib and the data is fitted to a spline. Slight differences from the LES are expected in the vicinity of the 180 degree bend since the LES computation was carried out assuming a fully developed turbulent flow two ribs upstream of the bend, while a complete channel is studied in this case.

A comparison of the friction factors shows that DES, like LES predicts a negative friction factor due to pressure recovery downstream of the inlet. URANS completely fails to predict this recovery and predicts a large pressure drop across the first rib. Further downstream as the flow reaches a fully developed state the predictions by DES as well as URANS are consistent with the LES predictions. The average friction factor, as predicted by DES and URANS, from the 4th rib to the 10th rib is observed to be around 8.15 times that in a smooth channel which compares well with the LES value of 8.5.

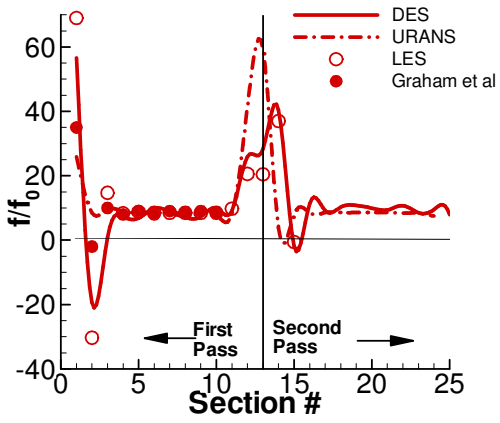

Figure 70: block averaged friction factors in the complete channel

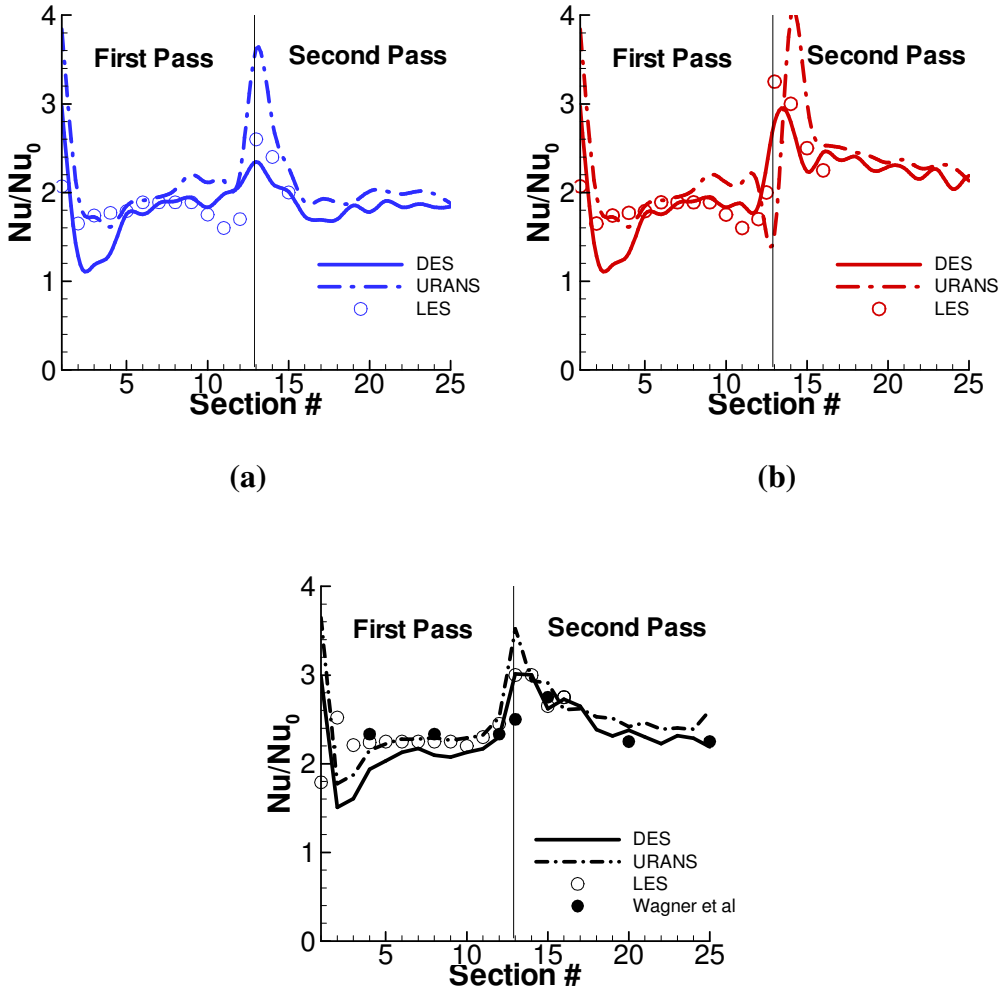

Figure 71: Block averaged heat transfer at (a) inner wall (b) outer wall (c) ribbed wall

The shear induced due to the turning of the flow upstream of the 180 degree bend results in a higher friction factor in the region. Based on the LES predictions the friction factor immediately upstream of the bend is around three times that in a fully developed case. The friction factor in the bend is almost of similar magnitude but as the flow turns the corner (block 14 in Figure 1) it encounters a large drop in pressure. Pressure recovery results in a negative friction factor immediately downstream which is similar to the entry

region where an initial drop in pressure is followed by a pressure recovery. The pressure drop predicted in the vicinity of the 180 degree bend by DES compares well with the LES cases. URANS over-predicts the friction factor in the vicinity of the bend. As the flow settles down in the second pass, the average friction factor in the second pass of the duct is observed to be close to 9.5 as predicted by DES and URANS.

6.1.1.7 Pitch Averaged Heat Transfer Augmentation

Figure 71 shows the comparison of the pitch averaged heat transfer predicted by the DES and URANS with LES computations (Sewall *et al.,* 2006a-b) at the ribbed and the side walls. DES predictions in the first 4 ribs in the developing region of the duct are inconsistent with LES. However after the flow is (hydrodynamically and thermally) developed the predictions by DES are consistent with LES. URANS predictions at the side walls in the first six blocks agree with LES predictions but the heat transfer is over-predicted downstream in the fully developed region.

At the ribbed wall the heat transfer is under-predicted at the ribbed wall of the first 4 blocks by both DES and URANS. Further downstream in the fully developed region of the duct the heat transfer predictions are consistent with LES predictions.

Heat transfer increases in the vicinity of the 180 degree bend at all the walls. The DES predictions in the vicinity of the 180 degree bend are consistent with the LES results, though the values are slightly over-predicted at the inner wall. URANS shows little agreement with the DES and LES in the vicinity of the 180 degree bend.

In the second pass of the duct, the heat transfer at all the walls is higher than the first pass, due to the increase in turbulence and stronger secondary flows. Experiments by

Liou *et al.,* (2001) also showed a similar increase in overall heat transfer in the second pass of the duct. The overall heat transfer at the outer wall of the second pass is observed to be higher than the heat transfer at the inner wall, which is consistent with the trends observed by Wagner *et al.,* (1992) in their experiments on ducts with normal ribs.

6.1.2 Summary and Conclusions

The capability of DES and URANS in predicting the flow and heat transfer in a complete two pass channel has been evaluated. The LES computation in the developing region of the duct used around 8.85 x 10^6 cells (Sewall *et al.,* 2006a) and 8.4 x 10^6 cells were used in the LES computation in a 180 degree bend (Sewall and Tafti, 2006b). The DES and URANS computations of the complete two pass channel were carried out by discretizing the whole domain in to 7.7 x 10^6 cells. The flow and heat transfer in the fully developed region of the duct as predicted by DES compares well with the LES computations by Sewall and Tafti (2004), Sewall *et al*. (2006a) and experiments by Rau *et al.* (1998). URANS manages to capture the primary flow features but fails to capture the subtle secondary flows. The flow and heat transfer predicted by DES in the 180 degree bend are also consistent with the LES results in the bend by Sewall and Tafti (2006b) and experimental results by Sewall *et al*., (2006a).

DES does not predict shear layer transition with accuracy and as a result predicts a greater development length than LES. However, once the flow is fully developed, DES predictions compare very well with LES and experiments. The flow predicted by URANS shows that the first rib trips the flow and the flow immediately transitions to turbulence. The reattachment lengths are almost constant downstream of all the subsequent ribs.

From the computations performed, the following conclusions can be derived:

1. In spite of shortcomings in predicting transition correctly at the entrance to the duct, DES predicts flow and heat transfer with good accuracy in a flow which is dominated by separation and reattachment of shear layers, unsteady vortex induced secondary motions, and strong streamline curvature. It reproduces the correct physics and shows good quantitative comparisons with LES and experiments after the first 4 ribs. URANS predicts the transition as soon as the flow is tripped by the first rib and under-predicts the center line velocities in the developing region.
2. The average flow characteristics in the fully developed regions of the first pass are predicted with good accuracy by the DES computations. Owing to the accurate prediction of the main flow characteristics, the heat transfer on the ribbed wall, which is influenced mostly by the main flow, is also predicted with reasonable accuracy. The secondary flow is also accurately captured by the DES computations, while URANS fails to capture the secondary flow. Since the secondary flow is captured accurately by DES, the heat transfer enhancement predicted on the side wall is accurate in the DES case.
3. DES captures the flow features accurately in the 180 degree bend, while URANS completely fails to predict the recirculating cells in the inner wall and the outer corners of the bend. URANS also overpredicts the friction factor and the heat transfer in the bend. The flow and heat transfer predicted by DES in the bend are superior to URANS and compare well with the experiments and the LES predictions.

Thereby it is shown that by a small switch in the underlying model the accuracy of the model can be improved to be consistent with the underlying physics leading to better prediction capability.

6.2 Rotating Two Pass Duct – Effect of Coriolis Forces

The study of flow and heat transfer in a stationary two pass duct builds on the work in stationary fully developed ducts discussed in chapter 5.3 (stationary fully developed computation). In a similar manner this work builds on previous work (Chapter 5.4) that validates the performance of DES is predicting the effects of Coriolis forces on the flow and heat transfer in the fully developed region of the internal cooling duct.

The objective of this work is to evaluate the capabilities of DES in predicting the effects of rotation on the turbulent flow and heat transfer in a two-pass internal cooling ribbed duct. The present results are compared with LES calculations (Sewall *et al.,* 2005a, 2005b) and experiments (Wagner *et al.,* 1992, Prabhu and Vedula, 2003). Of particular interest is the ability of DES to predict the flow development in the duct, flow in the 180º bend and the reversal of the effects of rotation in the second pass of the duct.

The effects of rotation become prominent immediately after the inlet in the first pass of the duct. Coriolis forces introduce an asymmetry in the flow and heat transfer and hence the development lengths are affected. As the flow turns around the bend the effects of the Coriolis forces at the leading and trailing walls are reversed, as a result of the reversal in the flow direction. Comparisons are made with experiments, LES computations and fully developed DES computations to validate the performance of DES in predicting the effects of rotation.

6.2.1 Developing Flow

Figure 72 shows the comparison of the streamwise velocities at the spanwise center of the first pass (z/D_h = 0.5) of the internal cooling passage for a duct rotated at Ro = 0.30. The effect of rotation is evident from the shift of the maximum streamwise velocity (u/U_0 = 1.40) towards the trailing side of the duct. This shift is also accompanied by the larger regions of negative velocities (separation downstream of the rib) at the leading surface of the duct and shorter recirculation regions at the trailing surface. The figure shows the flow development in the first 10 ribs (out of 12 in the first pass). It is observed that while the flow fully develops by the 3rd – 4th rib in the stationary case, the rotating duct shows complete development of the flow only by the 8th rib.

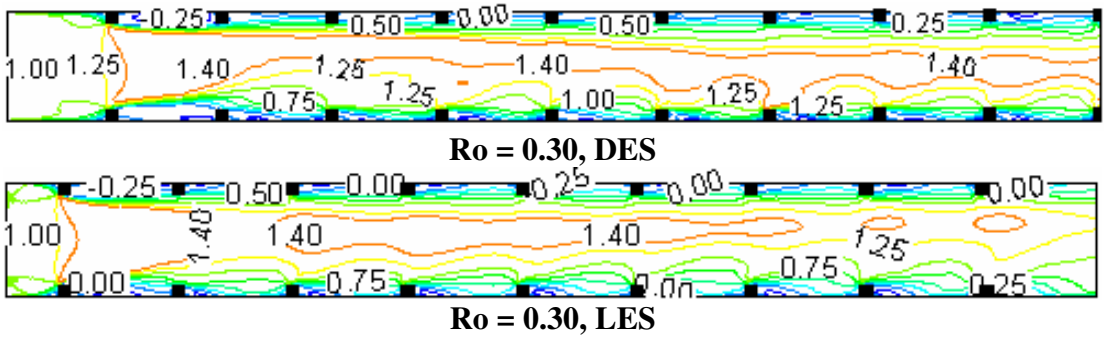

Figure 72: Contours of streamwise velocity at the center of the duct (z/D_h = 0.5).

A comparison of the streamwise velocities predicted by DES (64 x 64 x 64 grid per rib pitch) with analogous LES computations (96 x 96 x 96 grid per rib pitch) shows some differences. LES and DES show similar levels of velocities in the duct. While it is observed that while LES predicts the maximum velocity in the fully developed region of the duct to move towards the leading wall, DES predicts the maximum velocity to move towards the trailing wall. However the DES predictions concur with the observations

reported by Liou *et al.,* (2001). LDV measurements conducted by Liou on two pass ducts at a Reynolds number of 10,000 and rotation rates ranging from 0.0 to 0.2, showed a maximum velocity of around 1.40 – 1.50 times the bulk velocity skewed towards the trailing wall, as rotation is introduced in the duct.

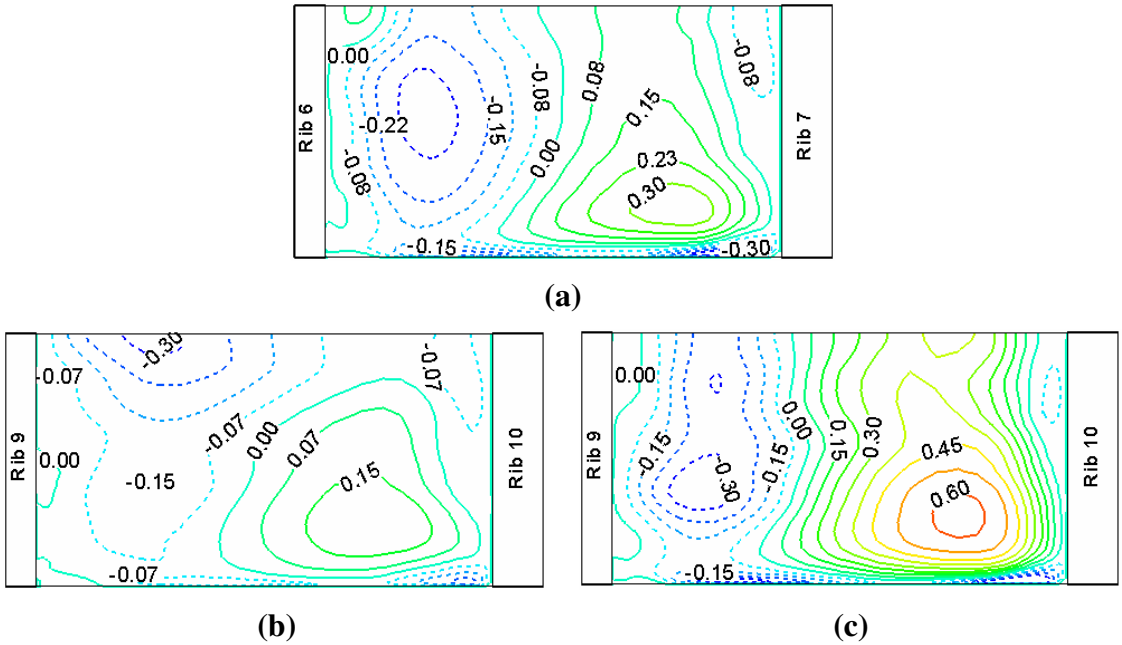

Figure 73: Comparison of the streamwise velocities at *y/e* = 0.15 in the fully developed regions of the flow for (a) Stationary Case (b) Ro = 0.30, Near Leading Wall (c) Ro = 0.30, Near Trailing Wall

Rau *et al.,* (1998) studied the flow features at a plane passing through the rib located at a distance of $0.15D_h$ from the ribbed wall, and observed the maximum velocity in this plane upstream of the rib at a distance of around $0.35D_h$ from the centerline. DES captures this feature in the fully-developed region accurately for the stationary, two pass cooling duct as shown in Figure 73(a). Rotation preserves this trend as can be observed in Figure 73(b)-(c), but the magnitudes are significantly different. The larger recirculation region at the leading wall results in lower velocities near this wall, while the smaller

recirculation region at the trailing wall followed by the acceleration of the flow after reattachment results in higher velocities near the trailing wall.

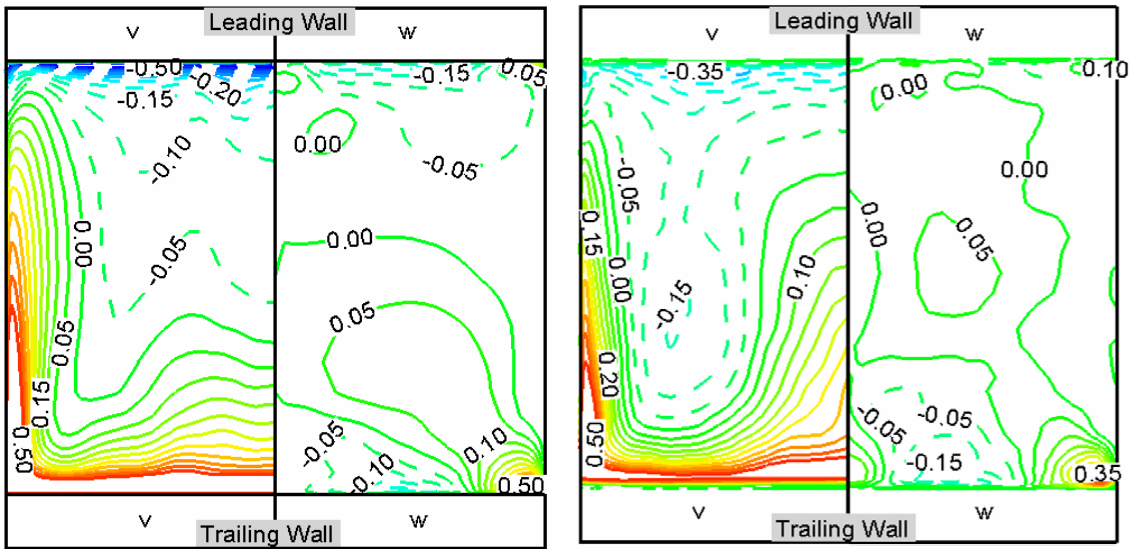

(a) **(b)**

Figure 74: Comparison of the secondary flow contours on top of rib 9 (a) DES (b) LES

The effect of Coriolis forces is also felt by the secondary flows. Figure 74 shows the comparison of the secondary flow contours in the fully developed region of the duct as predicted by DES and LES. The presence of ribs results in convergence of the flow as it passes over the ribs and hence positive *v*-velocities are observed above the rib on the trailing surface and negative velocities below the rib on the leading surface. In the vicinity of the side wall, DES predicts an increase in the *v*-velocities at the trailing surface and a decrease at the leading surface. This feature is consistent with LES predictions. The spanwise velocities observed on top of the ribs are negligible except near the side walls where the flow impinges on the side walls. A comparison of the secondary velocities with LES predictions shows good agreement near the side walls. Slight differences are observed in the *v*-velocities at the center of the duct, with the LES

predicting a strong secondary flow from the trailing wall to the center of the duct while DES predicts a weaker flow.

6.2.2 Heat Transfer Augmentation in the First Pass

Figure 75 and Figure 76 show the heat transfer augmentation at the leading and the trailing walls of the rotating duct as predicted by DES and LES. The heat transfer predicted by DES is compared with the LES computations. As rotation is introduced the heat transfer at the leading wall is observed to be lower than the heat transfer for a stationary duct. A comparison of the heat transfer predicted by DES with LES shows that DES underpredicts the heat transfer in the developing region of the duct. This feature is similar to the heat transfer predictions in the stationary duct. However as the flow develops the heat transfer levels are observed to be consistent with the LES computations in the fully-developed regions of the duct.

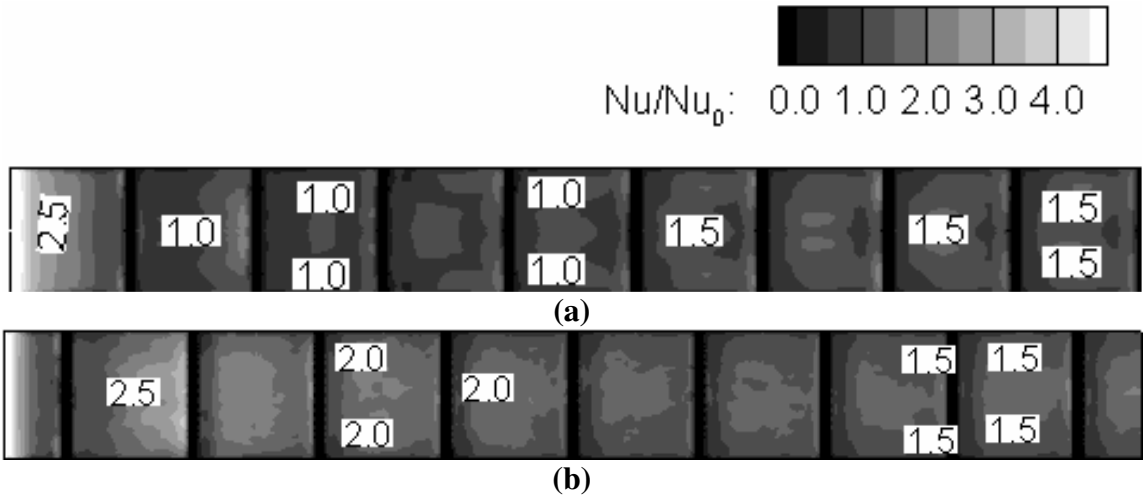

Figure 75: Heat transfer augmentation for the first pass of the rotating duct at the leading wall (a) DES (b) LES

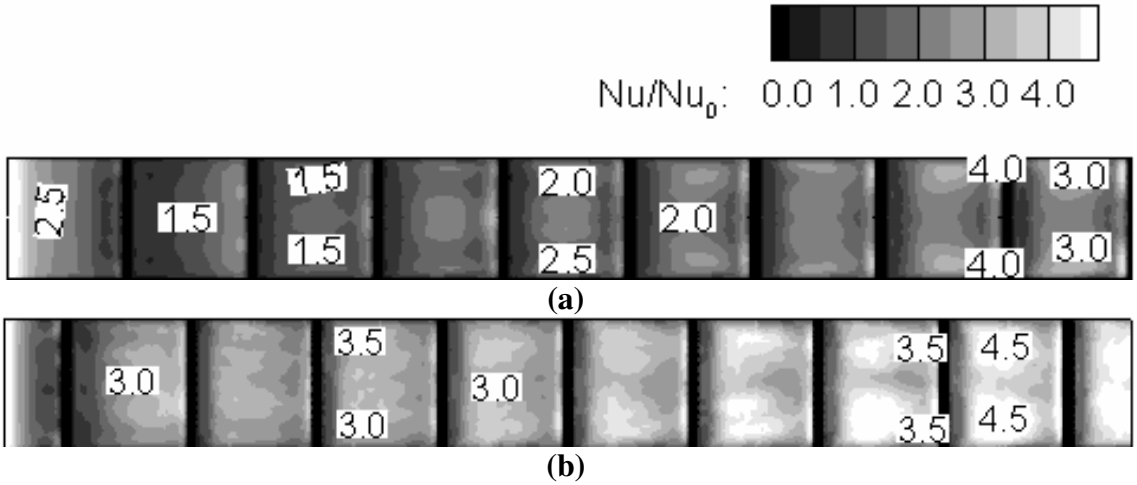

Figure 76: Heat transfer augmentation for the first pass of the rotating duct at the trailing wall (a) DES (b) LES

A comparison of the heat transfer predictions at the trailing surface further highlights the deficiency. Coriolis forces augment the turbulence in the vicinity of the trailing wall. This results in a steady increase in the heat transfer as the flow proceeds in the duct. LES captures this effect. Although DES captures a steady increase in the heat transfer, the levels of heat transfer are much smaller than LES. This is attributed to the inability of DES to predict transition to turbulence accurately. Since DES predicts a delayed transition and hence low turbulence levels the effects of Coriolis forces are weaker. So the heat transfer augmentation predicted is much lower.

Figure 77(a)-(b) shows the heat transfer on the side walls, predicted by LES and DES. Along the side walls, region of high heat transfer are observed in the vicinity of the rib due to secondary flow impingement. The heat transfer steadily decreases to lower values on moving from the trailing wall towards the leading wall. Since DES captures the secondary flows with reasonable accuracy, the heat transfer predictions at the side wall are consistent with the LES predictions.

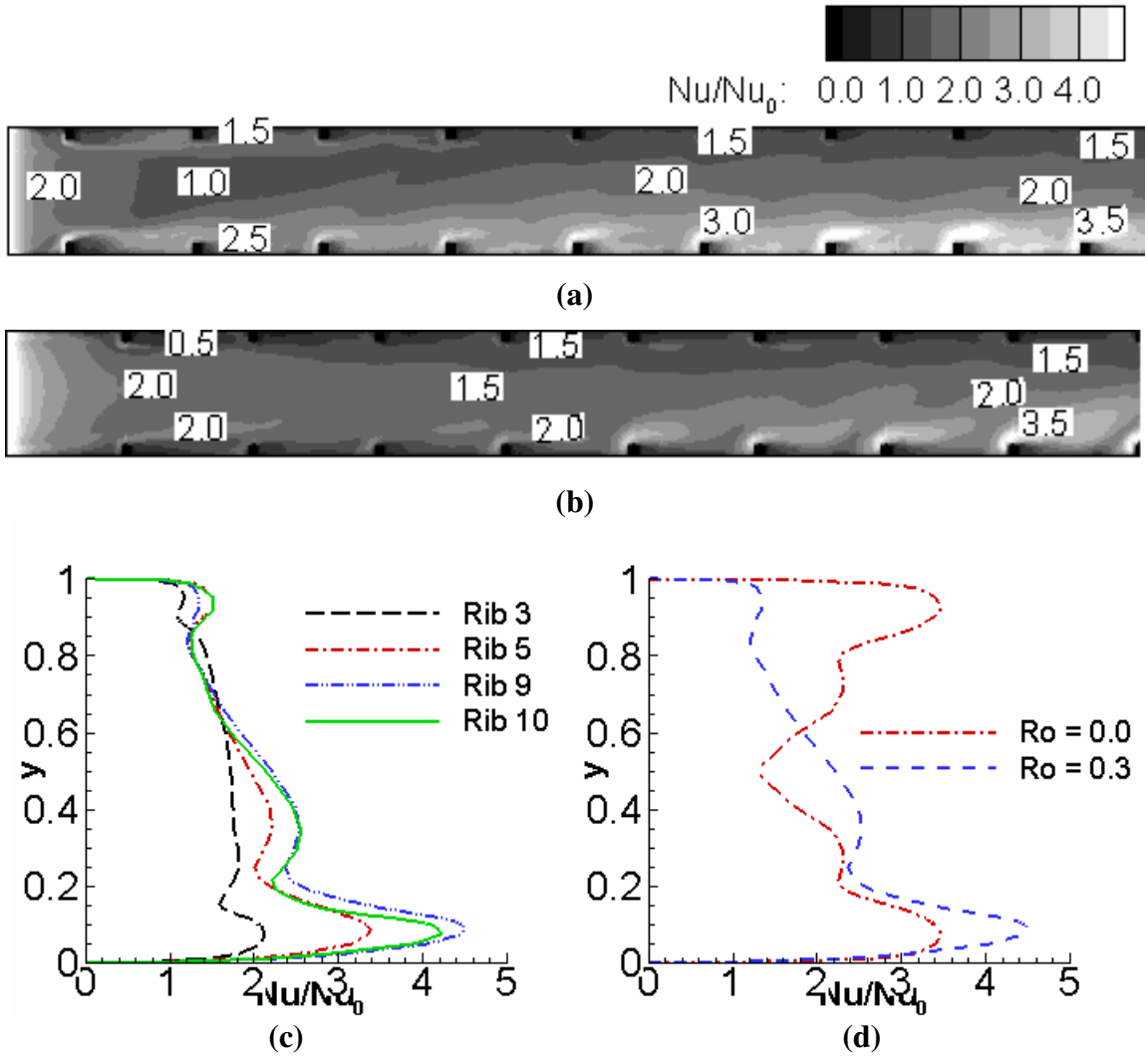

Figure 77: (a) Heat transfer augmentation for the first pass of the rotating duct at the side wall predicted by (a) LES (b) DES (c) Development of the heat transfer at the outer side wall (0.05D_h upstream of the ribs) of the internal cooling duct (d) Comparison of the fully developed heat transfer augmentations for the stationary and the rotating cases. y = 0 represents the trailing wall and y = 1 represents the leading wall

Figure 77(c) shows the development of the heat transfer at the side wall as the flow moves from the 3rd rib to the 10th rib. The flow is observed to be thermally fully-developed by the 9th rib, as can be observed from the similar heat transfer distributions in the vicinity of the 9th and 10th rib. This is comparatively slower than the heat transfer

development in the stationary duct, where the flow is observed to be thermally fully-developed by the 6th rib.

Figure 77(d) shows the comparison of the heat transfer augmentation in the fully developed regions of the stationary and the rotating ducts. While the heat transfer distribution is observed to be symmetric about the vertical center in the stationary duct, the rotating duct shows the difference in the heat transfer at the leading and the trailing walls. The heat transfer as pointed out earlier is higher in the vicinity of the trailing wall than near the leading wall. This is a direct effect of the secondary flows which are observed to be stronger near the trailing wall than near the leading wall.

6.2.3 Flow in the 180º Bend

Figure 78 shows the streamlines of the flow in the 180º bend region at three vertical locations along the duct. The plane y = 0.25 corresponds to a plane that is near the trailing wall while the plane y = 0.75 correspond to a plane that is near the leading wall. It is observed that from the streamlines plotted on the three planes that the presence of the bend introduces asymmetry in the flow features almost $2.5D_h$ upstream of the bend. As the flow turns around the bend, it results in a region of separation in the bend as the radius of curvature of the bend is more than the radius of curvature of the flow. It is observed that in the rotating duct, a region of separation is observed slightly downstream of the center of the bend, near the trailing surface. On moving towards the leading surface the size of this recirculation region increases and the recirculation region occupies almost the whole bend region near the leading surface. Flow impingement is observed at the

inner wall near the trailing surface and on both the inner and outer walls near the vertical center plane and in the proximity of the leading wall.

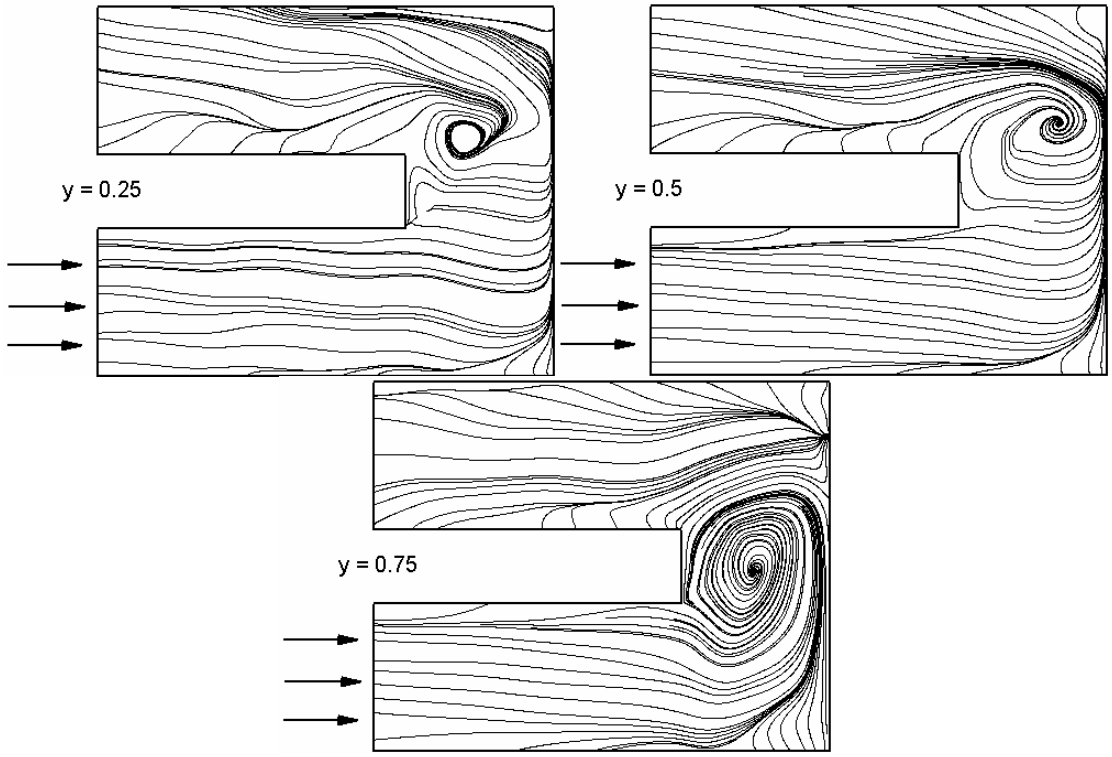

Figure 78: Flow in the U-bend connecting the first and the second passes of the duct at three different vertical locations

Figure 79 shows the secondary flow at the center of the 180º bend for the rotating duct. While the Dean vortices were observed to be of the same size in a stationary duct (Figure 67) it is observed that the cell at the leading side grows in size as rotation is introduced and almost completely occupies the cross-section of the bend. This characteristic of the secondary flow concurs with the observations of Liou *et al.,* (2001).

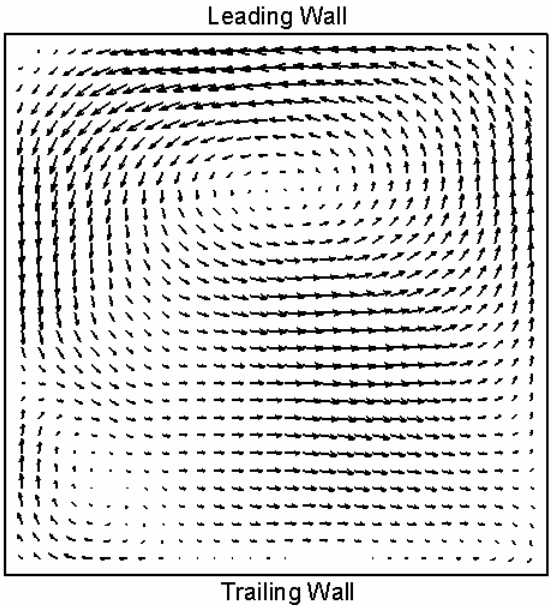

Figure 79: Secondary flow at the center of the 180º bend for the rotating duct

6.2.4 Heat Transfer in the 180º Bend

Figure 80 compares the heat transfer augmentation in the bend predicted by LES and DES. At the leading wall it is observed that the heat transfer is low in the first pass going into the bend. The heat transfer augmentation values of 1.4 – 2.6 predicted in this region by DES compares well with the heat transfer predicted by LES. This value is less than the heat transfer observed in the stationary duct. The Coriolis forces attenuate the turbulence in the leading surface resulting in lower levels of heat transfer at this surface. As the flow turns around the bend, higher levels of heat transfer are observed in the bend region due to the high shear associated with the turning of the flow. DES slightly over-predicts the heat transfer in the bend. Downstream of the bend, owing to the change in direction of the flow, the effect of Coriolis forces are reversed resulting in augmentation of turbulence at the leading surface. This results in high levels of heat transfer at the leading surface in the

second pass of the duct. The heat transfer augmentation contours predicted by DES concur with LES.

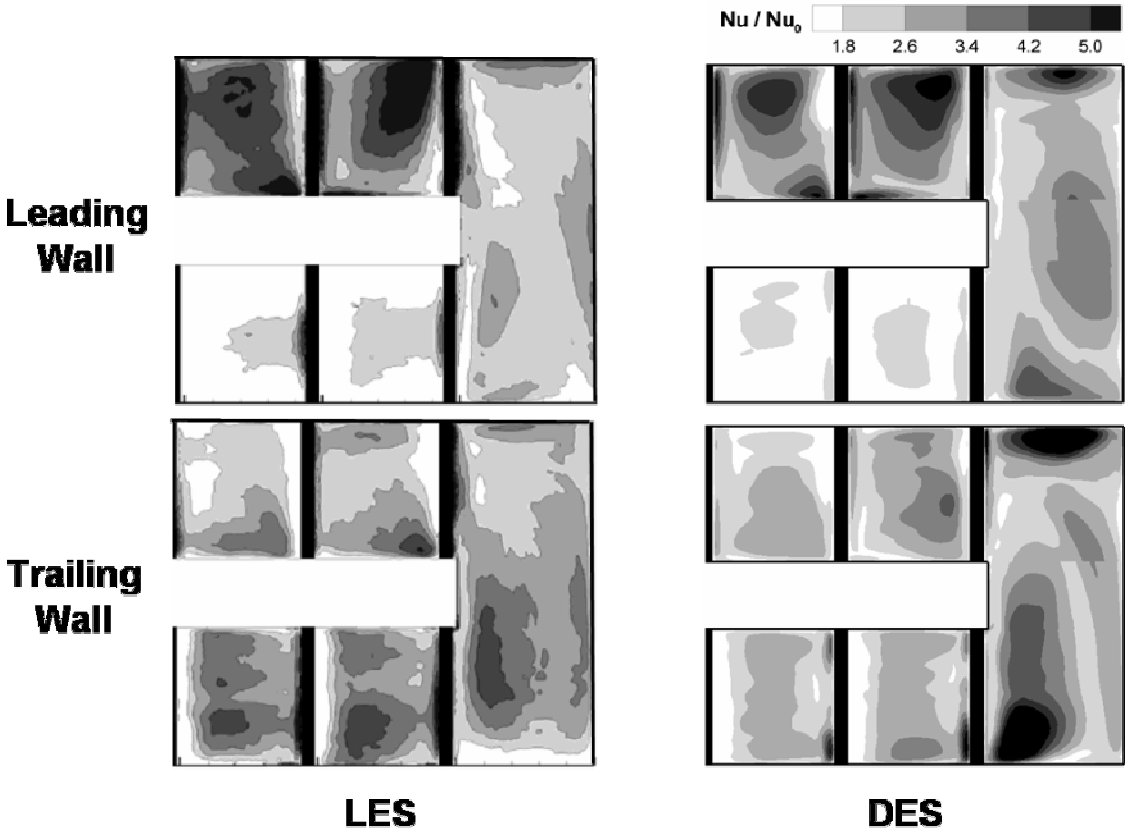

Figure 80: Heat transfer augmentation in the vicinity of the U bend

At the trailing wall, DES underpredicts the heat transfer in the first pass of the duct, where the flow development is observed to be slower that what was predicted by LES. This trend is also observed in the first pass of the duct upstream of the bend. However as the flow turns around the bend, high heat transfer is observed downstream of the last rib in the first pass and in the vicinity of the outer wall as the flow enters and leaves the bend. The heat transfer in the bend is slightly overpredicted by DES. The attenuation of turbulence in the vicinity of the trailing surface in the second pass results in low levels of

heat transfer. The heat transfer augmentation predicted by DES agrees reasonably well with LES in the second pass.

6.2.5 Pitch Averaged Friction Factor

The pitch-averaged friction factor reported in this study is obtained by using the average pressure drop across the ribs ($f = -\Delta p/2\Delta l$). The data obtained is compared to the fully developed DES computations and LES. The LES data is collected from two sources: LES in a rotating developing flow in a duct (Sewall and Tafti, 2005a) for the first 9 ribs and LES in a 180º bend for the bend and two ribs upstream and downstream of the bend. The comparison of the pitch averaged friction factors is shown in Figure 81.

As the flow enters through the inlet, the drastic pressure drop results in a high friction factor at the inlet. This is immediately followed by a pressure recovery resulting in a high value of negative friction factor between the first and the second ribs. As the flow proceeds further into the duct the friction factor settles around a value of 8.8 which compares well with the friction factor of 8.5, obtained from a fully developed DES case (Chapter 5.3) and LES (Sewall *et al.*, 2006a).

As the flow turns around the 180º bend higher friction factors are observed due to the shear induced by the turning of the flow. The friction factor immediately downstream of the bend reaches a value almost equal to the value of friction factor at the inlet. At the entrance to the second pass the pitch averaged friction factor behaves in a manner very similar to that at the inlet of the first pass. Another region of pressure recovery is observed resulting in a small negative friction following the 180º bend. A comparison of this trend matches well with the predictions by LES (Sewall and Tafti, 2005a). The

pressure drop across each rib in the second pass is also observed to settle down to a value of around 8.5 which is the value obtained in the first pass of the internal cooling passage.

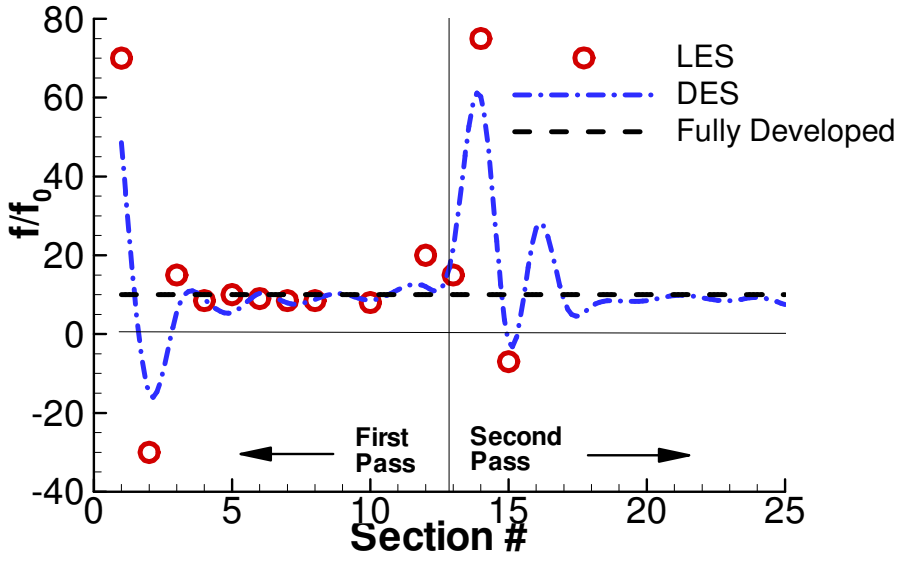

Figure 81: Comparison of the friction factor as predicted by the present computations with LES and fully developed flow predicted by DES

Prabhu and Vedula (2003) reported the pressure drop in a two pass channel by placing taps at the leading wall and the outer wall of ducts with 90º ribs. The geometry used is similar to the geometry currently studied. The study defined the local pressure drop and non-dimensionalized it by the dynamic pressure. So the pressure drop was defined as $K=(P_Y - P_{in})/(\frac{1}{2}\rho V^2)$, where P_{in} is the pressure at the inlet and P_Y is the local pressure measured. Pressure taps are placed on the leading wall and the outer wall of the duct, at locations shown in Figure 82. Results are compared with experiments at Re = 10,000, Ro = 0.38 and the width of the bend being $0.37D_h$, which compares with Re = 20,000, Ro = 0.30 and the width of the bend of $0.5D_h$ used in the current case.

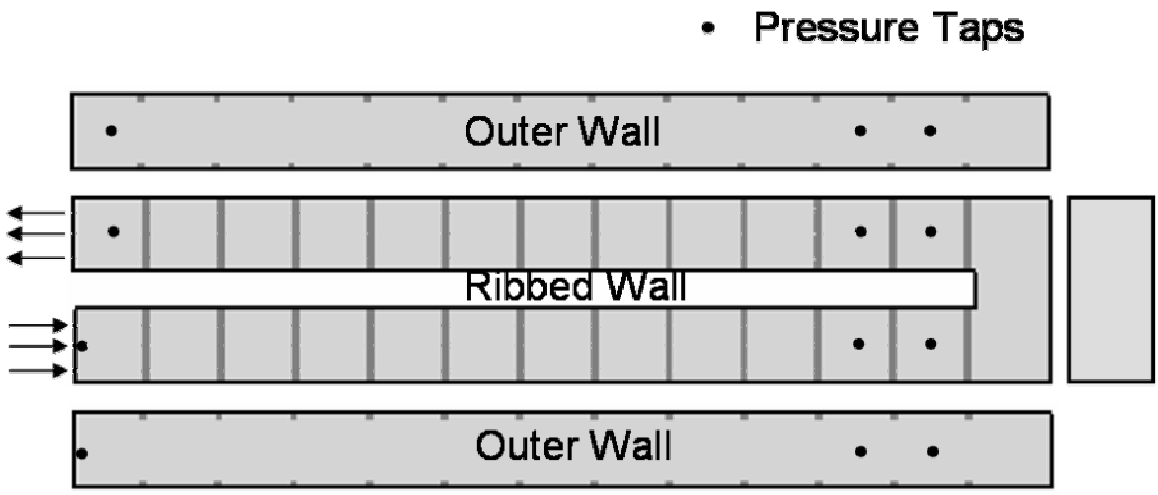

Figure 82: Locations of pressure taps in the two-pass duct used for comparison with experimental data by Prabhu and Vedula (Comparison in Table 9).

Table 9: Comparison of the surface pressure drop as predicted by the current computation in comparison with the experimental measurements by Prabhu and Vedula (2003) for the rotating duct.

	Across the first 10 Ribs	Across the 180º Bend	Across the last 10 ribs
Leading Wall – Prabhu and Vedula	-2.00	-2.00	-1.50
Leading Wall - Current Study	-2.35	-1.98	-1.47
Outer Wall – Prabhu and Vedula	-2.50	-1.25	-1.50
Outer Wall - Current Study	-2.40	-1.66	-1.40

A comparison of the pressure drop (ΔK) measured in the first pass, the 180º bend and the second pass is shown in Table 9. It is observed that the pressure drop predicted compare well with the experimentally measured values. Differences are observed in the value of ΔK measured across the first 10 ribs at the leading wall which may be a result of the slight difference in the rotation rates. The pressure drop across the bend measured from the taps placed at the outer wall may be attributed to the difference in the bend

width which affects the impingement at the outer walls, thereby affecting the local pressure at the location.

6.2.6 Rib Averaged Heat Transfer Augmentation

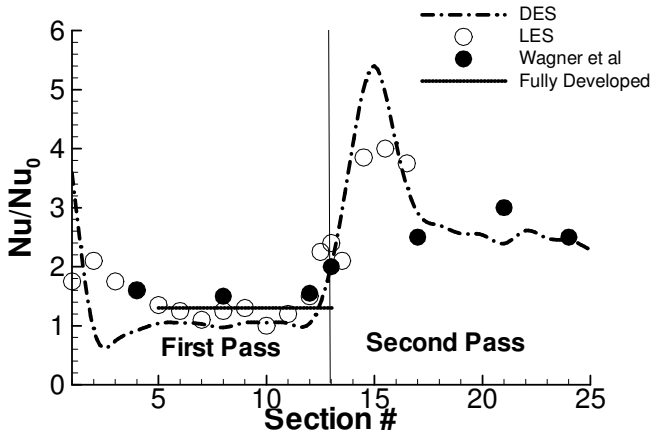

Figure 83: Ribbed averaged heat transfer at the leading wall

The rib averaged heat transfer at the leading wall is shown in Figure 83. The values obtained from the DES computation are compared with LES (Sewall and Tafti, 2005a), the fully developed DES computations (Chapter 5.4) and experimental measurements by Wagner *et al.*, (1992). As observed in the stationary case, DES underpredicts the heat transfer in the developing region of the duct. By the 7^{th} rib, the rib-averaged heat transfer settles down to a value of around 1.2 which agrees with the values predicted by LES. This value is however slightly lower than the values predicted by the fully developed computations and the experimental measurements. As the flow approaches the bend the heat transfer increases due to the high shear associated with the turning of the flow. This results in higher heat transfer in the bend. The average heat transfer at the leading wall in the bend agrees well with LES and the experimental measurements. Downstream of the

bend, the Coriolis forces aid in increasing the heat transfer. This causes higher heat transfer at the leading surface. The rib averaged heat transfer in the second pass of the duct agrees reasonably well with the experimental measurements.

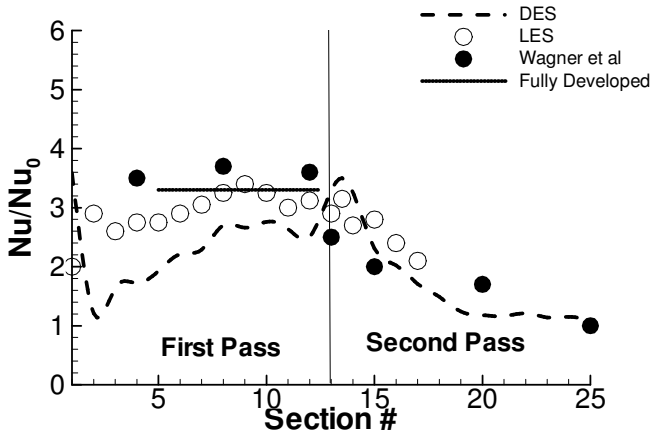

Figure 84: Ribbed averaged heat transfer at the trailing wall

The rib-averaged heat transfer at the trailing wall is shown in Figure 84. As explained in the earlier section the underprediction of heat transfer is attributed to the inability of DES to predict transition to turbulence. Though the heat transfer augmentation increases, the delay in development of turbulence results in an underprediction of the heat transfer by approximately 30%. Downstream of the bend, the heat transfer at the trailing surface decreases due to the reversal in the effects of the Coriolis forces. The trend is predicted well by DES showing good quantative agreement with LES and experiments.

6.2.7 Summary and Conclusions

In this part of the study the predictive capability of DES in the developing flow of a rotating ribbed duct is investigated. The internal cooling duct is subjected to rotation about the spanwise axis, with a constant rotation rate of Ro = 0.30. The results obtained

from a 7.7 x 10^6 grid used for DES are compared to the experimental measurements, two LES computations carried out a development region of the passage (8.85 x 10^6 cells) and in the 180º bend (8.4 x 10^6 cells) and some fully developed DES computations.

DES predicts a delayed transition and low turbulence in the developing region of the duct. Low turbulence levels due to delay in transition are also observed in the stationary duct, but this effect is intensified as rotation is introduced. The cumulative effect of the delay in transition and rotation results in an underprediction of the heat transfer. However as the flow passes through the 180 degree bend it picks up enough turbulence resulting in a reasonable prediction of the heat transfer augmentation in the bend. As the flow changes direction after passing through the bend the effects of Coriolis forces are reversed. The heat transfer augmentation increases at the leading surface and decreases at the trailing surface. The levels of heat transfer predicted in the duct downstream of the bend in the second pass show good agreement with LES and the measurements.

While DES is observed to combine the merits of high fidelity LES (accuracy) and (U)RANS (low computational cost), some deficiencies still exist. One deficiency that has been highlighted from these studies is the inability of DES to capture the transition to turbulence accurately, which still persists as with the RANS model on which it is based. Once the flow passes this hurdle, the flow features and heat transfer downstream in the fully turbulent regions of the flow are predicted accurately. The transition region is significant at the Reynolds number considered in the current computations. However, if the Reynolds number is increased the transition region decreases in size and so the prediction capabilities of DES are expected to be more beneficial at higher Reynolds numbers.

7 Summary and Conclusions

This study investigates the performance of Detached Eddy Simulation (DES) in predicting the non-canonical flow and heat transfer in ribbed ducts with direct applications to the internal cooling of turbine blades. In a series of calculations it is shown that DES successfully predicts the physics of rotation induced Coriolis forces and centrifugal buoyancy introduced due to thermal gradients in this industry specific internal flow configuration. The capabilities of DES in predicting the complex turbulent physics is highlighted by studies in flow in sudden expansion ducts subjected to rotation, the flow in a cavity with a heated wall and flow and heat transfer in stationary and rotating internal cooling ribbed ducts. From these studies the following conclusions are reached:

1. DES performs much better than an equivalent URANS in predicting the dynamics of separation and reattachment and in capturing the secondary flows which affect the heat transfer
2. DES maintains a LES like accuracy at around one-tenth the computational cost.
3. The main contribution of this work is showing that DES can be successfully applied to flows which are dominated by rotation induced Coriolis forces and centrifugal buoyancy. While linear eddy-viscosity models exhibit severe inadequacies in predicting such flows when used in URANS mode, DES by allowing LES like resolution of the large scales allows itself to be receptive to secondary strain which the base RANS model fails to capture.

7.1 Recommendations

DES is a simple, non-zonal approach for solving complex flows and has had qualitative success over a wide range of flows. DES is also observed to provide sufficient

unsteady information in the resolved range. The performance of DES is superior to URANS in several flows and demands computational power much less than LES.

In spite of these advantages, successful application of DES to a wide range of flows poses several challenges. Some potential areas of improvement for DES are discussed.

1. DES is a strategy that depends on the grid not only for accurately resolving the turbulence in the regions of interest, but also in determining the switch between RANS and LES. Though guidelines have been prescribed for Spalart – Allmaras (SA) based DES (Spalart, 2001) for external flows; grid generation is not trivial and requires some *a-priori* knowledge of the flow. One probable alternative is the Scale Adaptive Simulation (SAS) approach suggested by Menter (2003, 2005) that compares a von Karman length scale to the turbulent length scales to determine the switch from RANS to LES. This approach is still in its incipient stage of development and the prediction capability of this model for a wider range of flows in the context of two equation models remains to be established.
2. Though it is hypothesized that DES reduces to a well resolved LES solution as the grid is refined, this reduction is not smooth. Refining the grid in the vicinity of the wall results in the activation of the LES mode. If the grid in this region is not sufficiently resolved to capture the dominant frequencies, the quality of the solution deteriorates. However, local grid adaptation results in treating the regions of interest using LES and maintaining the RANS characteristics near the wall. The effects of local grid adaptation in resolving the unsteadiness has been shown in earlier studies (Forsythe *et al.,* 2002). The adaptation strategies however are empirical and are dependent on the user's grid generation skills.

3. While applying RANS characteristic in the boundary layer is advantageous in terms of the grid requirements, DES still depends on the base RANS model to predict the separation point. Studies on flows around circular and square cross-section cylinders (Squires *et al.,* 2002) have shown the capabilities of SA-DES in accurately predicting separation in such flows. However the same feature is yet to be established using the other DES models, especially for smooth geometries.
4. Another bottleneck for DES, as pointed out by this study its inability in predicting transition in the separated shear layers in the rib. Accurate prediction of transition requires a good turbulence model that can also capture transition. While incorporation of transition models has been studied for RANS models, applying these models in DES remains a potential area for development.
5. The transition from URANS to LES still remains a 'grey area' in DES (Spalart, 2001). The physics behind the switch from a completely modeled solution in the RANS regions to a well resolved LES still remains to be understood.

References

Chapter 1: Introduction

Constantinescu, G., Squires, K. D., 2000, LES and DES investigations of turbulent flow over a sphere. AIAA-2000-0540, 2000.

Constantinescu, G.S., Pacheco, R., Squires, K.D., 2002, Detached-eddy simulation of flow over a sphere, AIAA Paper 2002-0425, 2002.

Forsythe, J.R., Squires, K.D., Wurtzler, K.E., Spalart, P.R., 2002, Detached-Eddy Simulation of fighter aircraft at high alpha, AIAA Paper 2002-0591, 2002.

Kapadia, S., Roy, S., Vallero, M., Wurtzler, K.E., Forsythe, J.R., 2003, Detached Eddy Simulation Over a Reference Ahmed Car Model, AIAA 2003-0857, 2003.

Kotapati-Apparao, R.B., Squires, K.D., Forsythe, J.R., 2003, Prediction of a prolate spheroid undergoing a pitchup maneuver, AIAA Paper 2003-0269, 2003.

Morton, S.A., Steenman, M.B., Cummings, R.M., Forsythe, J.R., 2003, DES grid resolution issues for vertical flows on a delta wing and an F-18C, AIAA Paper 2003-1103, 2003.

Nikitin, N.V., Nicoud, F., Wasistho, B., Squires, K.D., Spalart, P.R., 2000, An approach to wall modeling in Large-Eddy Simulation, Physics of Fluids, **12**(7), pp. 1629-1632, 2000.

Pope, S.B., 2001, Turbulent Flows, Cambridge University Press

Shur, M., Spalart, P.R., Strelets, P.R., Travin, A., 1999, Detached-eddy Simulation of an airfoil at high angle of attack. 4th Int. Symposium on Eng. Turb. Modelling and Experiments, May 24-26 1999, Corsica. W. Rodi and D. Laurence Eds., Elsevier

Spalart, P.R., Jou, W.H., Streletes. M., Allmaras. S.R., 1997, Comments on the feasibility of LES for wings and a hybrid RANS/LES approach, First AFSOR Int. Conf. on DNS/LES, Aug 4-8, 1997, In Advances in DNS/LES, C.Liu and Z.Liu Eds, Greyden Press, Columbus, OH.

Squires, K.D., Forsythe, J.R., Morton, S.A., Blake, D.C., Serrano, M., Wurtzler, K.E., Strang, W.E. , Tomaro, R.F., Spalart, P.R., 2002, Analysis of full aircraft with massive separation using Detached-Eddy Simulation, Proceedings of the High Performance Computing Modernization Program 2002 Users Group Conference, Austin, Texas, 2002.

Strelets, M., 2001, Detached Eddy Simulation of Massively Separated Flows, AIAA 2001-0879.

Travin, A., Shur, M. L., Strelets, M., and Spalart, P.R., 2000, Detached Eddy Simulation Past a Circular Cylinder, Flows, Turbulence, and Combustion, Vol. 63, pp. 193-313, 2000.

Viswanathan, A.K., Squires, K.D., Klismith, K., Forsythe, J.R., 2003, Detached-Eddy Simulation around a forebody at high angle of attack, AIAA Paper 2003-0263, 2003

Chapter 2: Literature Review

Abdel-Wahab, S., Tafti, D. K., 2004b. Large Eddy Simulations of Flow and Heat Transfer in a 90º Ribbed Duct with Rotation - Effect of Coriolis and Centrifugal Buoyancy Forces, J. Turbomachinery, 126(4), pp. 627-636, 2004.GT2004-53799, ASME Turbo Expo: 2004, Vienna, Austria.

Amano, R.S., Goel, P., 1995. Computation of turbulent flow beyond backward steps using Reynolds Stress closure, AIAA J, 1995 23, pp 1356.

Baldwin, B. S. and Lomax, H. (1978), Thin Layer Approximation and Algebraic Model for Separated Turbulent Flows, AIAA Paper 78-257

Bo, T., Iacovides, H., Launder, B.E., 1995, Developing Buoyancy-Modified Turbulent Flow in Ducts Rotating in Orthogonal Mode, Transactions of ASME 177, pp.474-484.

Bradshaw, P., 1969, The Analogy Between Streamline Curvature and Buoyancy in Turbulent Shear Flow, J. Fluid Mech, 36, Part 1, pp 177-191.

Bradshaw, P., 1988, Effects of Extra Strain – Review, Near Wall Turbulence, Zoran Zaric Memorial Conference Ed. S J Kline, N.H. Afghan, Hemisphere Publishing Corporation, pp 106 - 122.

Chima, R.V., 1996, A k-ω turbulence model for quasi-three dimensional turbo machinery flows, AIAA 96-0258.

Driver, D., Seegmiller, H.L., 1985. Features of reattaching turbulent shear layer in divergent channel flow, AIAA J., 23, 162-171.

Hanjalic, K., Launder, B.E., 1980, Sensitizing the Dissipation Equation to Irrotational Strains, ASME J. Fluids Eng., 102: 34.

Hanjalic, K., Kenjeres, S., Durst, F., 1996, Natural convection in partitioned two-dimensional enclosures at higher Rayleigh numbers, Int. J. Heat and Mass Transfer, 39(7), pp 1407-1427.

Hanjalic, K., Kenjeres, S., 2001, T-RANS simulation of Deterministic eddy structure driven thermal buoyancy and Lorentz force, Flow, Turbulence and Combustion, 66, pp 427-451.

Hellsten, A., 1998, Some improvements in Menter's k-ω SST turbulence model, AIAA 98-2554.

Howard, J.H.G., Patankar, S.V., Bordynuik, R.M., 1980, Flow prediction in rotating ducts using Coriolis-modified turbulence models, ASME Journal of Fluids Engg, 102, pp 456-461.

Humphrey, J.A.C., To, W.M., 1986, Numerical simulation of buoyant turbulent flow II – Free and mixed convection in a heated cavity, Int. J. Heat and Mass Transfer, 29(4), pp 593-610.

Iacovides, H., Launder, B.E., 1991, Parametric and Numerical Study of Fully Developed Flow and Heat Transfer in Rotating Rectangular Ducts, J. Turbomachinery 133, pp.331-338.

Iacovides, H., Raisee, M., 1999. Recent Progress in the Computation of Flow and Heat Transfer in Internal Cooling Passages of Turbine Blades Int. J. Heat Fluid Flow, 20. pp. 320-328, 1999.

Ishigaki, H., 1996, Analogy between turbulence flows in curved pipes and orthogonally rotating pipes, Journal of Fluid Mechanics, 307, pp 1 – 10.

Jia, R., Saidi, A., Sunden, B., 2002. Heat Transfer Enhancements in Square Ducts with V-Shaped Ribs of Various Angles, Proc ASME Turbo Expo, GT 2002-30209.

Kantha, L.H., 2004, The length scale equation in turbulence models, Nonlinear processes in Geophysics, 11, pp 83-97.

Launder, B.E., Priddin, C.H., Sharma, B.I., 1977, The calculation of turbulent boundary layers on spinning and curved surfaces, ASME Journal of Fluids Engg, pp 231-239, March.

Lin, Y.L., Shih, T,I-P, Stephens, M.A., Chyu, M.K., 2001, A numerical study of flow and heat transfer in a smooth and a ribbed U-duct with and without rotation, ASME Journal of Heat Transfer, 123, pp 219-232.

Mellor, G. L., Yamada, T., 1982, Development of a turbulence closure model for geophysical fluid problems, Rev. Geophys. and Space Phys., 20(4), 851-875, 1982.

Menter, F.R., 1993, Zonal Two Equation k-ω Turbulence Models for Aerodynamic Flows, AIAA Paper 93-2906.

Murata, A., Mochizuki, S., 2001, Large Eddy simulation with a dynamic subgrid-scale model of turbulent heat transfer in an orthogonally rotating rectangular duct with transverse rib turbulators, Int. J. Heat Mass Transfer 43, pp. 1243-1259.

Ooi, A., Iaccarino, G., Durbin, P.A., Behnia, 2002. M., Reynolds Averaged Simulation of Flow and Heat Transfer in Ribbed Ducts, Int. J. Heat and Fluid Flow, 23, pp 750-757.

Peng, S-H., Davidson, L., 1999, Computation of turbulent buoyant flows in enclosures with low-Reynolds number k-ω models, Int. J Heat and Fluid Flow, 20, pp 172-184.

Plett, E.G., Soultogiannis, A.A., Jouini, D.B., 1995, Numerical Simulation of ventilation air movement in partitioned offices, Indoor Air, 3, pp 26-33.

Prakash, C., Zerkle, R., 1995. Prediction of Turbulent Flow and Heat Transfer in a Ribbed Rectangular Duct With and Without Rotation, ASME J. of Turbomachinery, Vol 117, pp 255-264.

Rigby, D.L., 1998, Prediction of Heat and Mass Transfer in a Rotating Ribbed Coolant Passage with a 180 Degree Turn, 98-GT-329, International Gas Turbine and Aeroengine Congress and Exhibition, Stockholm, Sweden, June 2-5.

Rodi., 1980, Turbulence models and their applications in hydraulics, a state of art review, Int Association of Hydraulic Research, Delft, p30.

Rodi, W., Scheuerer, G., 1983, Calculation of curved shear layers with two-equation turbulence models, Physics of Fluids, 26(6).

Saidi, A., Sunden, B., 2001. On Prediction of Thermal-Hydraulic Characteristics of Square-Sectioned Ribbed Cooling Ducts, ASME J. of Turbomachinery, Vol 123.

Sewall, E.A., Tafti, D.K., 2005, Large Eddy Simulation of Flow and Heat Transfer in the Developing Flow Region of a Rotating Gas Turbine Blade Internal Cooling Duct with Coriolis and Buoyancy Forces, GT 2005-68519, ASME Turbo Expo 2005, June 6-9, 2005, Reno-Tahoe, Nevada, USA.

Shankar, V., Davidson, L., Olsson, E., 1995, Numerical investigation of turbulent plumes in both ambient and stratified surroundings, Indoor Air, 5, pp 136-146.

Sharif, M.A.R., Liu, W., 2003, Numerical study of turbulent natural convection in a side-heated square cavity at various angles of inclination, Numerical Heat Transfer, Part A, 43: 693-716.

Stips, A., Burchars, H., Bolding, K., 2002, Modeling of convective turbulence with a two-equation k-ε turbulence closure scheme, Ocean Dynamics, 52, 153-168.

Strelets, M., 2001, Detached Eddy Simulation of Massively Separated Flows, AIAA 2001-0879.

Tafti, D.K., 2005, Evaluating the Role of Subgrid Stress Modelling in a Ribbed Duct for the Internal Cooling of Turbine Blades, Int. J Heat and Fluid Flow 26(1), pp. 92-104.

To, W.M., Humphrey, J.A.C., 1986, Numerical simulation of buoyant turbulent flow I – Free convection along a heated, vertical flat plate, Int. J. Heat and Mass Transfer, 29(4), pp 573-592.

Umlauf, L., Burchard, H., Hutter, K., 2003, Extending the k-ω turbulence model towards oceanic applications, Ocean Modelling, 5, pp 195-218

Watanabe, K., Takahashi, T., 2002, LES Simulation and Experimental Measurement of Fully Developed Ribbed Channel Flow and Heat Transfer, Proc. ASME Turbo Expo: 2002-GT-30203.

Wilcox, D.C., Chambers, T.L., 1977, Streamline curvature effects on turbulent boundary layers, AIAA Journal, Vol 15, No.4.

Wilcox, D.C., 1988. Reassessment of the Scale-Determining Equation for Advanced Turbulence Models, AIAA Journal, Vol 26 (11), pp 1299-1310. Nov 1988.

Yeoh, G.H., Yuen, R.K.K., Chen, D.H., Kwok, W.K., 2002, Combustion and heat transfer in compartment fires, Numerical Heat Transfer, Part A, 42, pp 153 – 172.

Yokosawa, H., Fujita, H., Iwata, S., 1989, Measurement of Turbulent Flow in a Square Duct with Roughened Walls on Two Opposite Sides, Int. J. of Heat and Fluid Flow, Vol 10(2), pp 125-135, 1989.

Zhao, C.Y., So, R.M.C., Gatski, T.B., 2001, Turbulence modeling effects on the prediction of equilibrium states of buoyant shear flows, Theoretical and Computational Fluid Dynamics, 14, pp 399-422.

Chapter 3: Computational Model and Governing Equations

Abdel-Wahab, S, Tafti, D.K., 2004a. Large Eddy Simulation of Flow and Heat Transfer in a Staggered 45° Ribbed Duct, ASME Turbo Expo: 2004, Vienna, Austria, GT2004-53800.

Abdel-Wahab, S., Tafti, D. K., 2004b. Large Eddy Simulations of Flow and Heat Transfer in a 90º Ribbed Duct with Rotation - Effect of Coriolis and Centrifugal Buoyancy Forces, J. Turbomachinery, 126(4), pp. 627-636, 2004.GT2004-53799, ASME Turbo Expo: 2004, Vienna, Austria.

Incropera, F.P. and Dewitt, 2002. D.P., Fundamentals of Heat and Mass Transfer, fifth edition, John Wiley and Sons, New York.

Menter, F.R., 1992, Improved Two-Equation k-ω Turbulence Models for Aerodynamic Flows, NASA Technical Memorandum 103975.

Menter, F.R., 1993, Zonal Two Equation k-ω Turbulence Models for Aerodynamic Flows, AIAA Paper 93-2906.

Sewall, E.A., Tafti, D.K., Graham, A., Thole, K.A., 2005c. Experimental Validation of Large Eddy Simulation of flow and heat transfer in a Stationary Ribbed Duct. Submitted Int. J. Heat and Fluid Flow, 2005.

Spalart, P.R., Jou, W.H., Streletes. M., Allmaras. S.R., 1997, Comments on the feasibility of LES for wings and a hybrid RANS/LES approach, First AFSOR Int. Conf. on DNS/LES, Aug 4-8, 1997, In Advances in DNS/LES, C.Liu and Z.Liu Eds, Greyden Press, Columbus, OH.

Strelets, M., 2001, Detached Eddy Simulation of Massively Separated Flows, AIAA 2001-0879.

Tafti, D.K., 2001, GenIDLEST – A Scalable Parallel Computational Tool for Simulating Complex Turbulent Flows, Proc. ASME Fluids Engineering Division, FED – Vol. 256, ASME-IMECE, New York.
Tafti, D.K., 2005, Evaluating the Role of Subgrid Stress Modelling in a Ribbed Duct for the Internal

Wilcox, D.C., 1988. Reassessment of the Scale-Determining Equation for Advanced Turbulence Models, AIAA Journal, Vol 26 (11), pp 1299-1310. Nov 1988.

Chapter 4: Validation Cases

Bradshaw, P., 1969, The Analogy Between Streamline Curvature and Buoyancy in Turbulent Shear Flow, J. Fluid Mech, 36, Part 1, pp 177-191.

Bradshaw, P., 1988, Effects of Extra Strain – Review, Near Wall Turbulence, Zoran Zaric Memorial Conference Ed. S J Kline, N.H. Afghan, Hemisphere Publishing Corporation, pp 106 - 122.

Chong, M.S., Perry, A.E., Cantwell, B.J., 1990, A General Classification of Three-Dimensional Flow Fields, Physics of Fluids A, Vol 2 (5), pp 765-777.

Chow, W.K., Gao, P.Z., 2004, Large Eddy Simulation of Turbulent Convective Cavity Flow, *Int. J. Computational Fluid Dynamics*, 18(8), pp 641 – 650.

Ghosal, S., Lund, T.S., Moin, P., Akselvoll, K., 1995, A Dynamic Localization Model for Large Eddy Simulation of Turbulent Flows, *Journal of Fluid Mechanics,* Vol 286, pp 229-255.

Grand, D., 1975, Contribution a l'etude des courant de recirculation, PhD. Thesis, *L'Universite Scientifique et Medicale et Institut Nationale, Polytechnique*, Grenoble.

Hanjalic, K., Kenjeres, S., Durst, F.,1996 Natural convection in partitioned two-dimensional enclosures at higher Rayleigh numbers, *Int. J. Heat and Mass Transfer*, 39(7), pp 1407-1427.

Hassid, S., 2002, Effects of buoyancy on the turbulence model equations., Ocean Dynamics, 52, pp 169-178.

Hellsten, A., 1998, Some improvements in Menter's k-ω SST turbulence model, AIAA 98-2554.

Iaccarino, G., Ooi, A., Pettersson Rief, B.A., Durbin, P., 1999, RANS Simulations of Rotating Flows, Center of Turbulence Research, Annual Research Briefs, pp 257 – 266.

Ideriah, F.J.K., 1980, Prediction of Turbulent Cavity Flow Driven By Buoyancy and Shear, *Journal of Mechanical Engineering Science*, 22(6), pp 287 – 295

Johnston, J.P.; Halleen, R.M.; Lezius, D.K., 1972, Effects of spanwise rotation on the structure of two-dimensional fully developed turbulent channel flow, J. Fluid Mech. 56, pp 533 – 557.

Koutsourakis, N., Vlachogiannis, D., Sfetsos, A., Bartzis, J.G., 2003, CFD in atmospheric dispersion problems – State of the art, QNET-CFD Network Newsletter, Vol 2, No 1.

Launder, B.E., Priddin, C.H., Sharma, B.I., 1977, The calculation of turbulent boundary layers on spinning and curved surfaces, ASME Journal of Fluids Engg, pp 231-239.

Moore, J.A., 1973, Wake and an Eddy in a Rotating, Radial-Flow Passage. Part 1: Experimental Observations, ASME Journal of Engg. For Power, pp 205 – 212.

Murakami, S., Ohira, N., Kato, S., 1999, CFD analysis of a thermal plume and the indoor air flow using k-ε models with buoyancy effects, Flow, Turbulence and Combustion, 63, pp 113-134.

Nilsen, P.J., Andersson, H.I., 1990, Rotational Effects on Sudden-Expansion Flows, Engineering Turbulence Modelling and Experiments, Elsevier Science Publications Co., Inc Rodi and Ganić, pp 65-72.

Peng, S-H., Davidson, L., 1999, Computation of turbulent buoyant flows in enclosures with low-Reynolds number k-ω models, *Int. J Heat and Fluid Flow*, 20, pp 172-184.

Plett, E.G., Soultogiannis, A.A., Jouini, D.B., 1995, Numerical Simulation of ventilation air movement in partitioned offices, Indoor Air, 3, pp 26-33.

Rodi, W., Scheuerer, G., 1983, Calculation of curved shear layers with two-equation turbulence models, *Physics of Fluids*, 26(6).

Rothe, P. H.., 1975, The effects of System Rotation on Separation, Reattachment and Performance in Two-dimensional Diffusers. Stanford University Dissertation, Dept. Mechanical Engineering

Rothe, P. H., Johnston, J. P., 1976, Effects of System Rotation on the Performance of Two-Dimensional Diffusers, ASME J. Fluids Eng., 9, pp. 422–430.

Rothe, P.H., Johnston, J.P., 1979, Free Shear Layer Behavior in Rotating Systems, ASME J. Fluids Eng., 101, pp 117-120.

Stips, A., Burchars, H., Bolding, K., 2003, Modeling of convective turbulence with a two-equation k-ε turbulence closure scheme, *Ocean Dynamics*, 52, 153-168.

Wilcox, D.C., 1988. Reassessment of the Scale-Determining Equation for Advanced Turbulence Models, AIAA Journal, Vol 26 (11), pp 1299-1310.

Wilcox, D.C., Chambers, T.L., 1977, Streamline curvature effects on turbulent boundary layers, *AIAA Journal*, Vol 15, No.4.

Yeoh, G.H., Yuen, R.K.K., Chen, D.H., Kwok, W.K., 2002, Combustion and heat transfer in compartment fires, Numerical Heat Transfer, Part A, 42, pp 153 – 172.

Chapter 5: Fully Developed Cases

Abdel-Wahab, S., Tafti, D. K., 2004, Large Eddy Simulations of Flow and Heat Transfer in a 90º Ribbed Duct with Rotation - Effect of Coriolis and Centrifugal Buoyancy Forces, *J. Turbomachinery* 126(4), pp. 627-636.

Chong, M.S., Perry, A.E., Cantwell, B.J., 1990, A general classification of three-dimensional flow fields, *Phy. Fluids A.,* 2(5), pp 765 – 777.

Forsythe. J.R, Squires. K.D, Wurtzler. K.E., Spalart. P.R, 2002, Detached-Eddy Simulation of Fighter Aircraft at High Alpha, AIAA Paper 2002-0591.

Halleen, R.M., and Johnston, J.P., 1967, The Influence of Rotation of Flow in a Long Rectangular Channel – An Experimental Study, Report MD-18, Thermosciences Division, Dept. of Mech. Eng., Stanford University.

Lezius, D.K., and Johnston, J.P., 1976, Roll-Cell Instabilities in Rotating Laminar and Turbulent Channel Flows, *J. Fluid Mech.* Vol. 77, Part 1, pp. 153-175.

Lin, Y.L., Shih, T,I-P, Stephens, M.A., Chyu, M.K., 2001, A numerical study of flow and heat transfer in a smooth and a ribbed U-duct with and without rotation, ASME *Journal of Heat Transfer*, 123, pp 219-232.

Liou, T.M., Wu, Y.Y., Chang, Y., 1993, LDV Measurements of Periodic Fully Developed Main and Secondary Flows in a Channel with Rib-disturbed Walls, *ASME Journal of Fluids Engineering,* Vol 115, pp 109-114.

Liou, T.M., Chen, M.Y., Tsai, M.H., 2001, Fluid Flow and Heat Transfer in a Rotating Two-Pass Square Duct with In-Line 90° Ribs, ASME Turbo Expo: 2001-GT-0185.

Murata, A., Mochizuki, S., 1999, Effect of cross-sectional aspect ratio on turbulent heat transfer in an orthogonally rotating rectangular smooth duct, *Int. J. Heat Mass Transfer* 42, pp. 3803-3814.

Murata, A., Mochizuki, S., 2000, Large Eddy simulation with a dynamic subgrid-scale model of turbulent heat transfer in an orthogonally rotating rectangular duct with transverse rib turbulators, *Int. J. Heat Mass Transfer* 43, pp. 1243-1259.

Murata, A., Mochizuki, S., 2001, Comparison between Laminar and Turbulent Heat Transfer in Stationary Square Ducts with Transverse or Angled Rib Turbulators, 2001, *Int. J. Heat Mass Transfer,* 44, pp 1127-1141.

Ooi, A., Iaccarino, G., Durbin, P.A., Behnia, M., 2002, Reynolds Averaged Simulation of Flow and Heat Transfer in Ribbed Ducts, 2002, *Int. J. Heat and Fluid Flow,* 23, pp 750-757..

Parsons, J.A., Han, J.C., Zang, Y.M., 1994, Wall Heating Effect on Local Heat Transfer in a Rotating Two-Pass Square Channel with 90º Rib Turbulators, *Int. J. Heat Mass Transfer* 37, 1411-1420.

Prakash, C., Zerkle, R., 1995, Prediction of Turbulent Flow and Heat Transfer in a Ribbed Rectangular Duct with and without Rotation, *J. Turbomachinery*, 117, pp.255-264.

Rau, G., Cakan, M., Moeller, D., Arts, T., 1988, The Effect of Periodic Ribs on Local Aerodynamic and Heat Transfer Performance of a Straight Cooling Channel, *ASME J. Turbomachinery,* 120, pp 368-375.

Tafti, D.K., 2005, Evaluating the Role of Subgrid Stress Modelling in a Ribbed Duct for the Internal Cooling of Turbine Blades, *Int. J Heat and Fluid Flow 26(1),* pp. 92-104.

Wagner, J.H., Johnson, B. V., Graziani, R.A., Yeh, F.C., 1992, Heat Transfer in Rotating Serpentine Passages with Trips Normal to the Flow, *J. Turbomachinery* 114, pp. 847-857.

Chapter 6: Flow and Heat Transfer in a Two pass duct

Ekkad., S.V., Han, J.C., 1997, Detailed Heat Transfer Distributions in Tow-pass Square Channels with Rib Turbulators, *Int. J Heat Mass Transfer*, Vol 40 (11), pp 2525-2537.

Johnson, B.V., Wagner, J.H., Steuber, G.D., 1994, Effect of Rotation on Coolant Passage Heat Transfer: Vol II – Coolant Passages with Trips Normal and Skew to Flow, *NASA Contractor's Report 4396*.

Liou, T.M., Chen, M.Y., Tsai, M.H., 2001, Fluid Flow and Heat Transfer in a Rotating Two-Pass Square Duct with In-Line 90° Ribs, *ASME Turbo Expo: 2001-GT-0185*.

Prabhu, S.V., Vedula, R.P., 2003, Pressure Drop Characteristics in a Rib Roughened Square Duct with a Sharp 180º Bend, *Journal of Enhanced Heat Transfer*, Vol 10, pp 363-377.

Ooi, A., Iaccarino, G., Durbin, P.A., Behnia, M., 2002, Reynolds Averaged Simulation of Flow and Heat Transfer in Ribbed Ducts, 2002, *Int. J. Heat and Fluid Flow,* 23, pp 750-757..

Rau, G., Cakan, M., Moeller, D., Arts, T., 1988, The Effect of Periodic Ribs on Local Aerodynamic and Heat Transfer Performance of a Straight Cooling Channel, *ASME J. Turbomachinery,* 120, pp 368-375.

Sewall, E.A., Tafti, D.K., 2004, Large Eddy Simulation of the Developing Region of a Stationary Ribbed Internal Turbine Blade Cooling Channel, *Paper No. GT2004-53832*, ASME Turbo Expo: 2004, June 14-17, 2004, Vienna, Austria.

Sewall, E.A., Tafti, D.K., 2005a, Large Eddy Simulation of Flow and Heat Transfer in the Developing Flow Region of a Rotating Gas Turbine Blade Internal Cooling Duct with Coriolis and Buoyancy Forces, GT 2005-68519, ASME Turbo Expo 2005, June 6-9, 2005, Reno-Tahoe, Nevada, USA. Submitted *J. Turbomachinery.*

Sewall, E., 2005b, Large Eddy Simulation of Flow and Heat Transfer in the Developing Region and 180 Bend Regions of Ribbed Gas Turbine Internal Cooling Ducts with Rotation – Effect of Coriolis and Centrifugal Buoyancy Forces, *Ph.D Dissertation*, Virginia Polytechnic Institute and State University.

Sewall, E.A., Tafti, D.K., Graham, A., Thole, K.A., 2006a, Experimental Validation of Large Eddy Simulation of flow and heat transfer in a Stationary Ribbed Duct. *Int. J. Heat and Fluid Flow*, Vol 27(2), pp 243 - 258.

Sewall, E.A., Tafti, D.K., 2006b, Large Eddy Simulation of Flow and Heat Transfer in the 180° bend Region of a Stationary Ribbed Gas Turbine internal Cooling Duct, *J. Turbomachinery*, 128.

Wagner, J.H., Johnson, B. V., Graziani, R.A., Yeh, F.C., 1992, Heat Transfer in Rotating Serpentine Passages with Trips Normal to the Flow, *J. Turbomachinery* 114, pp. 847-857.

Chapter 7: Summary and Conclusions

Forsythe, J.R., Squires, K.D., Wurtzler, K.E., Spalart, P.R., 2002, Detached-Eddy Simulation of fighter aircraft at high alpha, AIAA Paper 2002-0591, 2002.

Menter, F., Kuntz., M., Bender, R., 2003, A Scalable Adaptive Simulation Model for Turbulent Flow Predictions, AIAA paper 2003-0767.

Menter, F., Egorov, V., 2005, A Scale Adaptive Simulation Model using Two-Equation Models, AIAA 2005-1095.

Spalart, P.R., 2001, Young-Person's Guide to Detached Eddy Simulations, NASA/CR-2001-211032.

Squires, K.D., Forsythe, J.R., Morton, S.A., Strang, W.Z., Wurtzler, K.E., Tomaro, R.F., Grismer, M.J., Spalart, P.R., 2002, AIAA Paper 2002-1021.

Appendix A: Additional Buoyancy Production Term in the *k*-equation

The *k*-equation (TKE equation) can be systematically derived from the momentum equations. To account for the effects of buoyancy an extra strain term ($Ar\overline{\theta}$) is added to the momentum equations. The corresponding buoyancy production term for the *k*-equation can be derived in a similar fashion as the derivation of the TKE equations. The same procedure has been applied to derive the extra strain term to incorporate the effects of buoyancy. The derivation is as shown below.

[Total Momentum Equation – Mean Momentum Equation]

$$Ar\theta - Ar\overline{\theta} = Ar\theta'$$

Multiplying this by v' gives $Ar\theta'v'$ and averaging this gives $Ar\overline{\theta'v'}$. Applying Bousinessq approximation this term reduces to

$$Ar\frac{\nu_t}{\mathrm{Pr}_t}\left(\frac{\partial\theta}{\partial y}\right) = Ar\frac{1}{\mathrm{Re}_t\,\mathrm{Pr}_t}\left(\frac{\partial\theta}{\partial y}\right)$$

So the new *k*-equation (with the additional buoyancy production term) is

$$\boxed{\frac{\partial k}{\partial t}+\frac{\partial(uk)}{\partial x}+\frac{\partial(vk)}{\partial y}=\tau_{xy}\left[\frac{\partial u}{\partial y}+\frac{\partial v}{\partial x}\right]-\frac{k^{3/2}}{\delta}+\left(\frac{1}{\mathrm{Re}}+\frac{\sigma^*}{\mathrm{Re}_t}\right)\left[\frac{\partial k}{\partial x}+\frac{\partial k}{\partial y}\right]+\frac{Ar}{\mathrm{Re}_t\,\mathrm{Pr}_t}\left(\frac{\partial\theta}{\partial y}\right)}$$

This is the term that has been used to incorporate the effects of buoyancy in the RANS and DES formulations of the *k*-ω model for the validations in Chapter 4.2.3. From

this study it was observed that the term had considerable influence on the RANS predictions, while hardly affecting the DES predictions. Since no differences in the DES prediction capabilities were noted, this modification had not been incorporated in the later DES studies (Chapter 5.5).

Appendix B: Dimensionless Parameters

The dimensionless parameters that are used in the current study are listed below.

Skin Friction Coefficient (*f*, C_f) – The skin friction coefficient characterizes the relationship between the velocity and the pressure drop across a set of points. Since the pressure drop can be related to the shear stress at the surface for an internal flow the skin friction coefficient can be defined as the ratio of the shear stress to the dynamic pressure ($C_f = \tau_w/0.5\rho V^2$)

Archimedes Number (*Ar*) – The Archimedes number is defined as the ratio of the buoyancy forces due to thermal gradients to the viscous forces in a fluid. ($Ar = g\beta\Delta TL/U_0^2$)

Buoyancy Number (Bo) – The buoyancy parameter is defined as ratio of the buoyancy forces to the inertial forces. ($\mathrm{Bo} = \frac{\Delta\rho}{\rho} \cdot \frac{r}{D_h} . Ro^2$)

Nusselt Number (Nu) – The Nusselt number measures the heat transfer occurring at a surface due to convection in relation to a surface where conduction is the dominant form of heat transfer. ($\mathrm{Nu} = hL/k$)

Prandtl Number (Pr) – The Prandtl number is defined as the ratio of the momentum diffusivity to thermal diffusivity. ($\mathrm{Pr} = \mu C_p/k$)

Reynolds Number (Re) – The Reynolds number is defined as the ratio of the inertial forces to the viscous forces. The Reynolds number determines if the flow is laminar or turbulent. ($Re = VD/\nu$)

Rotation Number (Ro) – The rotation number is the ratio of the Coriolis forces in a fluid to the inertial forces. The rotation number is the reciprocal of the more popular Rossby number which is used to compare the effects of Coriolis forces. ($Ro = \Omega L/U$)

Richardson Number (Ri) – The Richardson number is the relative importance of the thermal stratification to the inertial effects of the fluid. The higher the Richardson number, the more the flow is driven by buoyancy.

Appendix C: Abstracts of relevant publications

Viswanathan, A.K., Tafti, D.K., "Detached Eddy Simulation of Turbulent Flow and Heat Transfer in a Ribbed Duct", *ASME Journal of Fluids Engineering,* **127(5), pp 888-896***,* September 2005**.**

Detached Eddy Simulation (DES) of a hydrodynamic and thermally developed turbulent flow is presented for a stationary duct with square ribs aligned normal to the main flow direction. The rib height to channel hydraulic diameter (e/D_h) is 0.1, the rib pitch to rib height (P/e) is 10 and the calculations have been carried out for a bulk Reynolds number of 20,000. DES calculations are carried out on a 96^3 grid, a 64^3 grid and a 48^3 grid to study the effect of grid resolution. Based on the agreement with earlier LES computations, the 64^3 grid is observed to be suitable for the DES computation. DES and RANS calculations carried out on the 64^3 grid are compared to LES calculations on $96^3/128^3$ grids and experimental measurements. The flow and heat transfer characteristics for the DES cases compare well with the LES results and the experiments. The average friction and the augmentation ratios are consistent with experimental results, predicting values within 10% of the measured quantities, at a cost lower than the LES calculations. RANS fails to capture some key features of the flow.

Viswanathan, A.K., Tafti, D.K., "Detached Eddy Simulation of Turbulent Flow and Heat Transfer in a Two-pass Internal Cooling Duct", *International Journal of Heat and Fluid Flow,* **27(1), pp 1-20***, February 2006.*

Numerical predictions of a hydrodynamic and thermally developed turbulent flow are presented for a stationary duct with square ribs aligned normal to the main flow direction. The rib height to channel hydraulic diameter (e/D_h) is 0.1, the rib pitch to rib height (P/e) is 10 and the calculations have been carried out for a bulk Reynolds number of 20,000. The capability of the Detached Eddy Simulation (DES) version of the 1988 k-ω model has been validated in predicting the turbulent flow field and the heat transfer in a complete two pass channel. Results of mean flow quantities, secondary flows, friction and heat transfer are compared to experiments and Large-Eddy Simulations (LES). It is concluded that in spite of shortcomings in predicting transition correctly at the entrance to the duct, DES surpasses the base capability of the underlying RANS model and predicts flow and heat transfer with good accuracy in a flow which is dominated by separation and reattachment of shear layers, unsteady vortex induced secondary motions, and strong streamline curvature. In all aspects it reproduces the correct physics and shows good quantitative comparisons with LES and experiments while reducing the computational complexity by nearly an order of magnitude.

Viswanathan, A.K., Tafti, D.K., "Detached Eddy Simulation of Flow and Heat Transfer in Fully Developed Rotating Internal Cooling Channel with Normal Ribs", *International Journal of Heat and Fluid Flow,* **27(3), pp 351-370***, June 2006.*

Numerical predictions of a hydrodynamic and thermally developed turbulent flow are presented for a rotating duct with square ribs aligned normal to the main flow direction. Three rotation numbers Ro=0.18, 0.35 and 0.67 are investigated. The rib height to channel hydraulic diameter (e/D_h) is 0.1, the rib pitch to rib height (P/e) is 10 and the calculations have been carried out for a bulk Reynolds number of 20,000. The capability of the Detached Eddy Simulation (DES) in predicting the turbulent flow field and the heat transfer under the effects of rotation has been evaluated against Unsteady Reynolds-Averaged Navier Stokes (URANS), Large-Eddy Simulations (LES), and experimental data. It is shown that DES by capturing a large portion of the turbulent energy in the resolved scales is much more capable than URANS in transcending the underlying shortcomings of the RANS model. DES shows much better fidelity in calculating critical components of the turbulent flow field and heat transfer than URANS does.

Viswanathan, A.K., Tafti, D.K., "A Comparative Study of DES and URANS for Flow Prediction in a Two-pass Internal Cooling Duct", ***In press*** *ASME Journal of Fluids Engineering*

The capabilities of the Detached Eddy Simulation (DES) and the Unsteady Reynolds Averaged Navier-Stokes (URANS) versions of the 1988 k-ω model in predicting the turbulent flow field in a two-pass internal cooling duct with normal ribs is presented. The flow is dominated by the separation and reattachment of shear layers; unsteady vorticity induced secondary flows and strong streamline curvature. The techniques are evaluated in predicting the developing flow at the entrance to the duct and downstream of the 180^o bend, fully-developed regime in the first pass, and in the 180^o bend. Results of mean flow quantities, secondary flows and the average friction factor are compared to experiments and Large-Eddy Simulations (LES). DES predicts a slower flow development than LES, while URANS predicts it much earlier than LES computations and experiments. However it is observed that as fully developed conditions are established, the capability of the base model in predicting the flow is enhanced by the DES formulation. DES accurately predicts the flow both in the fully-developed region as well as the 180^o bend of the duct. URANS fails to predict the secondary flows in the fully-developed region of the duct and is clearly inferior to DES in the 180^o bend.